MODE-LOCKING AND OTHER NONLINEAR EFFECTS IN CdS PHONON MASERS

by

MELVIN DOUGLAS SMEATON

B.Sc. (Hon.), University of Alberta, 1971

M.Sc., Simon Fraser University, 1973

A THESIS SUBMITTED IN PARTIAL FULFILLMENT OF

THE REQUIREMENTS FOR THE DEGREE OF

DOCTOR OF PHILOSOPHY

in

THE DEPARTMENT OF PHYSICS

We accept this thesis as conforming

to the required standard

THE UNIVERSITY OF BRITISH COLUMBIA

November, 1976

© Melvin Douglas Smeaton, 1976

In presenting this thesis in partial fulfilment of the requirements for an advanced degree at the University of British Columbia, I agree that the Library shall make it freely available for reference and study. I further agree that permission for extensive copying of this thesis for scholarly purposes may be granted by the Head of my Department or by his representatives. It is understood that copying or publication of this thesis for financial gain shall not be allowed without my written permission.

Department of PHYSICS

The University of British Columbia
2075 Wesbrook Place
Vancouver, Canada
V6T 1W5

Date NOV. 2, 1976

ABSTRACT

The nonlinear theory of acoustic amplification in piezoelectric semiconductors has been applied to the CdS phonon maser, to demonstrate that mode-locking in such a device can be predicted as a consequence of its structure and nonlinear properties of the acousto-electric amplifying mechanism. The first direct evidence of mode-locking in the phonon maser has been provided by applying optical processing techniques to signals obtained from laser diffraction. A new and powerful technique for the analysis of optical signals, involving a combination of spatial and temporal filtering, has been developed.

Further application of optical processing has allowed the first direct observation of acoustically induced space charge gratings in CdS. Proper exploitation of the methods outlined should give insight into the underlying physical processes.

In addition to the optical experiments, data has been presented that demonstrates the existence of two new photovoltaic effects in CdS. The resulting photovoltages are several orders of magnitude larger than those produced by known photovoltaic effects. As yet, the physical processes involved are not properly understood.

TABLE OF CONTENTS

LIST OF TABLES

LIST OF FIGURES

LIST OF SYMBOLS

A	nonlinear parameter in acoustic gain theory
$A(x,z,t)$	optical amplitude
A_{DF}	total dark field amplitude
$A_f(x',t)$	focal plane optical amplitude
A_n	optical amplitude in n^{th} diffraction spot
$A_o(x,t)$	near field (object plane) optical amplitude
$a_o(x,z,t)$	near field optical amplitude in absence of acoustic waves
α, $\alpha_{\pm}$	nonlinear acoustic gain; + parallel and - antiparallel to applied electric field
B_{ij}, B_i	components of the relative dielectric impermeability tensor and matrix, respectively
ΔB_i	change in the parameters B_i
β_n	parameter indicating the degree of spatial synchronization of Fourier components ψ_n
c	elastic stiffness constant
D, D_i	electric displacement
d	thickness of acoustic cavity
D_n	electron diffusion constant
δ_n	relative phases of mode-locked acoustic waves
E, E_i	electric field
e	piezoelectric stress constant
E_s	synchronous electric field = v_s/μ
E_t	total electric field
ϵ	permittivity constant

F	acoustic trapping fraction
Γ	lattice loss coefficient
γ	acoustic wave velocity parameter = $1 - v_D/v_s$, or normalized angle of incident light (section 1.3.2)
$\gamma_{\pm}$	acoustic wave velocity parameter: + parallel and - antiparallel to applied electric field
I	total current density
I_{DF}	total dark field intensity distribution
$I_{n,n+1,n+2}$	optical intensity distribution produced by combining diffraction orders n, n+1, n+2
$I^{\Omega}_{n,n+1,n+2}$	image plane signal obtained with spatial orders n, n+1, n+2 and temporal filter at Ω
$I^{\omega_m}_{1,0}$	image plane signal at frequency ω_m produced by imaging diffraction spots 0,1
I_s	synchronous current = $n_o q v_s$
J	conduction current density
J_n	Bessel function of order n
K	acoustic wave number
ΔK	acoustic phase shift produced by piezoelectric coupling
k	optical wave number
k'	= $k\sin\theta$, where θ is angle of diffraction
κ_i	principal dielectric constants
L	width of the acoustic cavity
Λ	acoustic wavelength
λ	optical wavelength
M	amplitude modulation index

μ	electron mobility
n	conduction band electron density, or index of refraction
Δn	change in electron density or index of refraction
n_i	principal refractive indices
n_I, n_{II}	semiaxes of index ellipse for isotropic material in the presence of strain
Δn_I, Δn_{II}	strain induced changes in index ellipse semiaxes
n_o	equilibrium electron density, or unperturbed refractive index
n_o, n_e	ordinary and extraordinary indices of refraction
n_o', n_e'	acoustically modified ordinary and extraordinary indices of refraction
Δn_o, Δn_e	$n_o' - n_o$, $n_e' - n_e$
Ω	acoustic frequency
ω	optical frequency
ω_c	conductivity relaxation frequency = σ/ε
ω_c'	conductivity relaxation frequency as modified by nonlinear theory
ω_D	diffusion frequency = v_s^2/D_n
ω_m	modulation frequency
p_{ij}	components of the optoelastic matrix
$\Phi(x,t)$	phase function describing mode-locked acoustic waveform
ϕ	phase angle, or angle of incidence
ϕ_A	acoustic phase function
ϕ_s	phase function describing static space charge grating
$\psi(x,z,t)$	envelope function describing acoustic modification of optical amplitude

$\psi_n(z)$	Fourier components of $\psi(x,z,t)$
Q	parameter characterizing diffraction
q	electron charge
r	reflectivity of acoustic cavity walls
ρ	mass density
S, S_i	strain amplitude
σ	electrical conductivity
T	acoustic stress
$T^{\Omega}_{n,n+1,n+2}$	component of $I_{n,n+1,n+2}$ at frequency Ω
$\tau^{\Omega}_{n,n+1,n+2}$	Fourier transform of $T^{\Omega}_{n,n+1,n+2}$
θ	phase angle = $Kx - \Omega t$, or angle of diffraction
Θ_n	linear combination of acoustic phases = $\delta_n - \delta_{n+1} + \delta_{n+2}$
u	mass displacement
V	= $2v\cos\Omega t$
V'	= $(2v\cos\Omega t + v_o)(1 + M\cos\omega_m t)$
V_n	= $2v_n\cos(nKd - n\Omega t + \delta_n)$
v, v_n	Raman - Nath parameter
v_D	electron drift velocity
v_o	amplitude of optical phase variation produced by static space charge grating
v_s	velocity of sound
z_{ij}	components of the electro-optic matrix
ζ	phase parameter = $(n_o kL - \omega t)$

ACKNOWLEDGEMENTS

I wish to thank my research supervisor, Dr. R.R. Haering, for a great many productive discussions, and for being a source of encouragement and motivation throughout the course of my research. Thanks are due also to Dr. J. Vrba, who participated in the initial stages of the development of a theoretical model for the mode-locked phonon maser. I am also grateful to Lore Hoffmann for her capable assistance in the preparation of publications. The financial support of the National Research Council, the International Nickle Company, and the University of British Columbia is gratefully acknowledged. Finally, I thank my wife Marg for her continuing support and for her assistance in typing this thesis.

FOREWORD

Chapters 1 and 2 document the results of optical diffraction and signal processing experiments, and contain the most important contributions of the thesis. Chapter 3 deals with new photovoltaic effects that are not yet understood. This chapter is included as a permanent record of the experimental results, and to provide a base for future work.

CHAPTER 1

MODE-LOCKING IN CdS PHONON MASERS

1.1 Introduction

Phonon masers are solid state acoustic oscillators produced by polishing the faces of piezoelectric single crystals accurately flat and parallel, to form high Q resonant structures which are strongly analogous to lasers. The most successful phonon masers have been fabricated from CdS. The application of a D.C. electric field of sufficient magnitude creates a situation in which net round-trip acoustic gain can be achieved by virtue of the piezoelectric coupling between drifting conduction electrons and local acoustic fields. Acoustic oscillation is then spontaneously built up from the thermal background. The linear theory of acoustic amplification in piezoelectric semiconductors (White 1962) has been well established, and reviews may be found in the literature (Gurevich 1969, McFee 1966).

Operation of the phonon maser is generally observed by monitoring the current passing through the device. There is a D.C. component to this current, due to the applied D.C. electric field, but there is also an A.C. component present when the phonon maser is operating. This acousto-electric current is produced by the tendency of electrons to group in piezoelectric potential wells produced by the acoustic wave. Maines and Paige (1970) reported that phonon masers operated under certain experimental conditions exhibited sharp spiking in the time display of

the A.C. current. The frequency display of the current signal consisted of a harmonic series having amplitudes constant in time, and a frequency spacing equal to the reciprocal of the round trip transit time of the crystal cavity. From these observations Maines and Paige (1970) concluded that the phonon maser was operating in a mode-locked regime, and, by analogy with mode-locked optical lasers, predicted that the acoustic output should consist of narrow, high strain pulses.

The validity of this prediction is, however, far from obvious, since the mode-locked regime is strongly nonlinear, and there is no one-to-one correspondence between the frequency spectrum of the acoustoelectric current and that of the acoustic fields. When the piezoelectric potential associated with these fields is much larger than the thermal energy, a purely Sinusoidal acoustic wave can result in an electron distribution with rich harmonic content (Gulayev 1970, Gurevich 1969). The nonlinear nature of the mode-locked regime is clearly established by the presence of strong current saturation, indicating that the conduction electrons are trapped in the potential wells associated with the acoustic wave, and are constrained to move with the velocity of sound. These considerations clearly indicate that the prediction of Maines and Paige (1970) should be verified by direct observation of the acoustic fields.

This chapter deals with a unique set of optical experiments that have provided verification of mode-locked operation, by allowing direct observation of the resulting acoustic strain pulses. The general

method relies on a powerful combination of spatial and temporal filtering applied to optical signals obtained from laser diffraction. Before considering the optical measurements, it is worthwhile to consider what mode-locking means and why the phonon maser may be mode-locked. This information may be provided by making a very fruitful analogy between a phonon maser and a general class of devices known as Repetitive Pulse Generators.

1.2 The Phonon Maser as a Repetitive Pulse Generator

It is well known that a feedback loop containing the basic elements of an amplifier, filter, delay line, and a nonlinear element called a saturable absorber, behaves as a Repetitive Pulse Generator (RPG) (Cutler 1955). The mode-locked optical laser is a well known example of such a device (Demaria et al 1969). The basic block diagram for a RPG is shown in FIG. 1(a). The output consists of a train of identical pulses recurring at a rate determined by the loop delay, with shape determined principally by the characteristics of the filter and saturable absorber, and width controlled primarily by the bandwidth of the filter.

The saturable absorber has a crucial role. It has the effect of emphasizing the highest amplitude parts in the pulse circulating in the feedback loop, while reducing the lower amplitudes. An element having the transmission characteristics shown in FIG 1 (a) will serve the purpose. As indicated, intensities $\geq I_o$ are passed almost unattenuated while lower intensities are reduced. A highly qualitative illustration of saturable absorber operation is shown in FIG 1 (b). As a circulating pulse makes

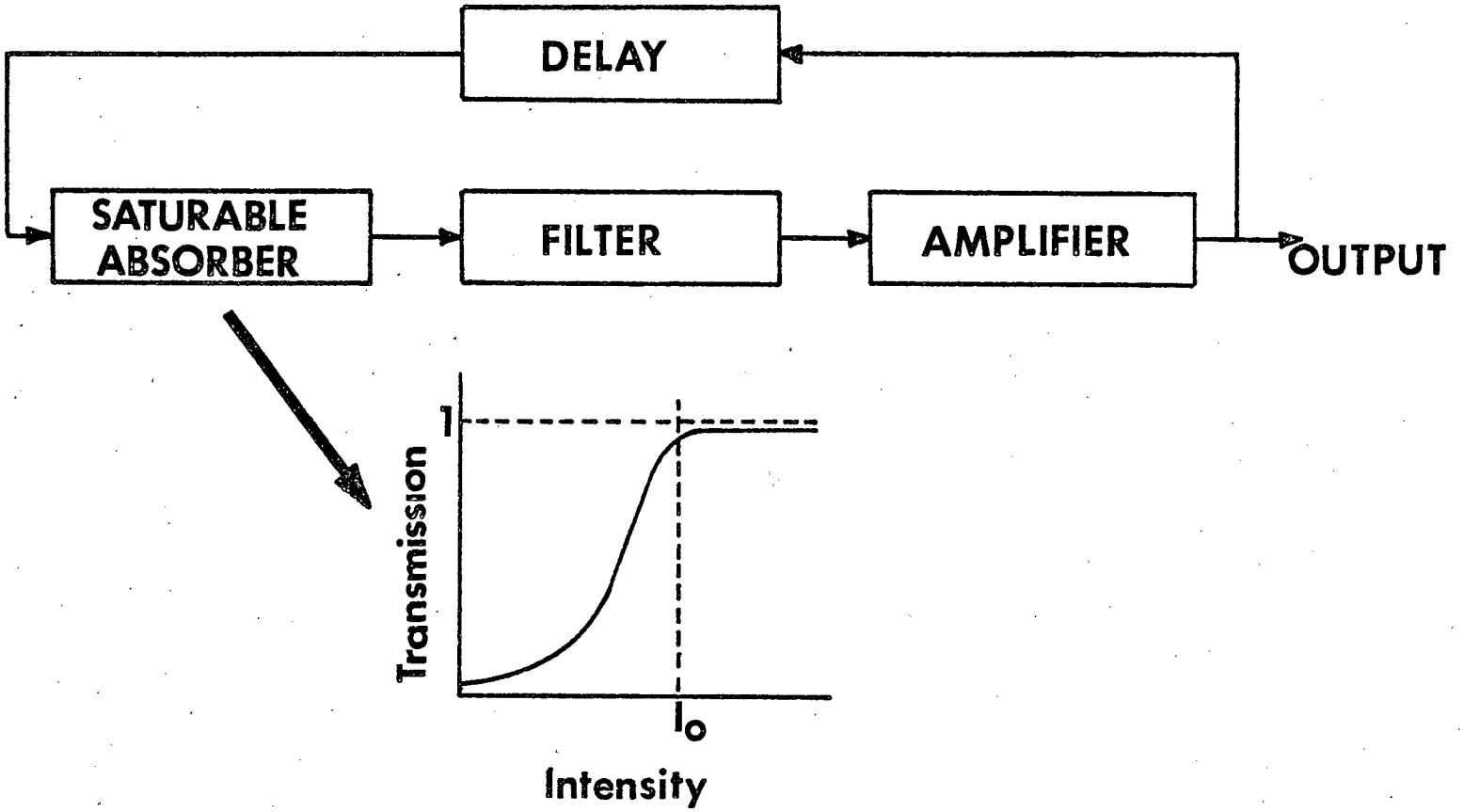

FIG 1(a). Block diagram for the Repetitive Pulse Generator (RPG).

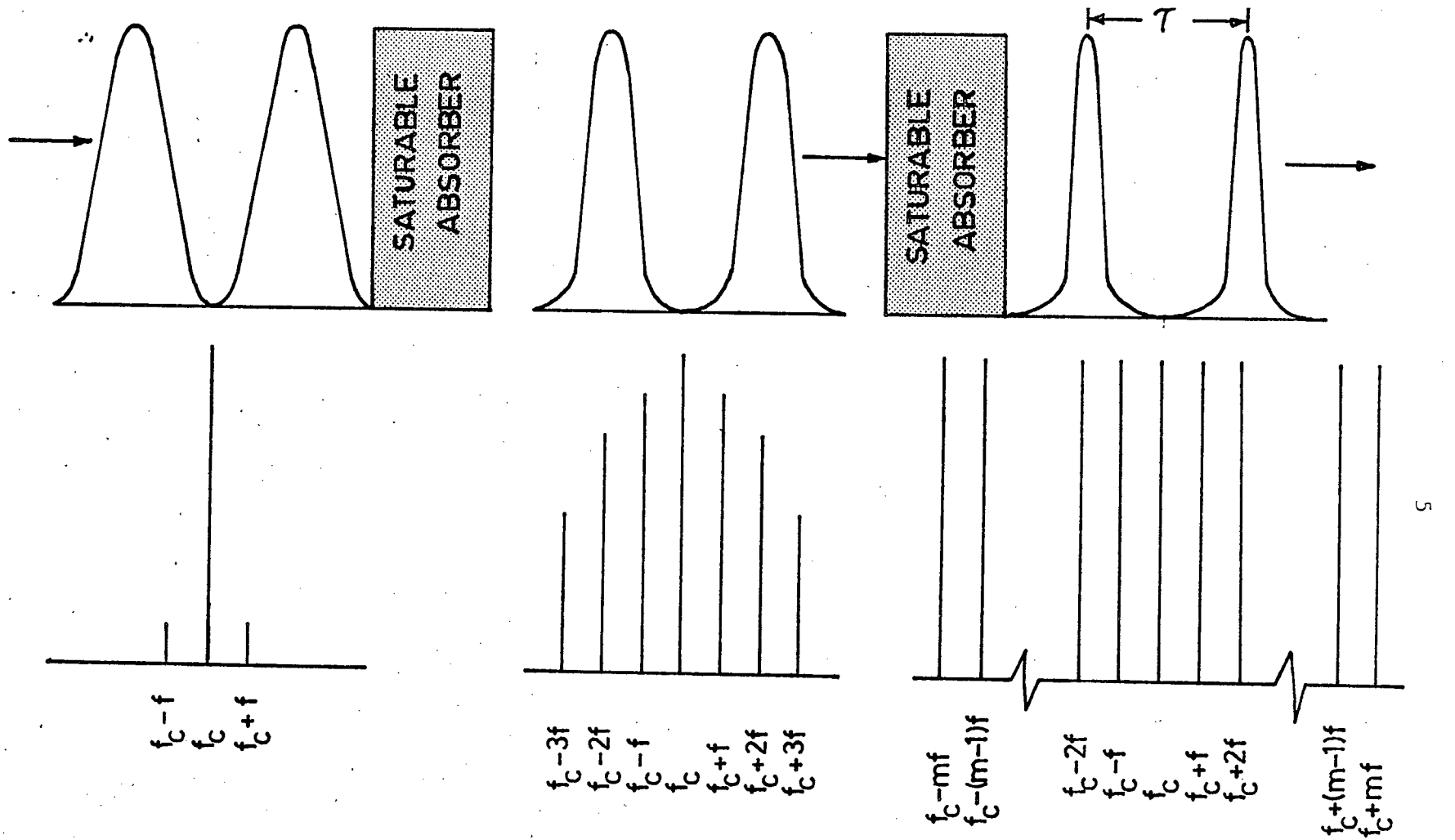

FIG 1(b). A qualitative illustration of the operation of a saturable absorber in both the time (upper) and frequency (lower) domains. Only the envelope of the pulses is shown in the time display. f_c is the center frequency or frequency of maximum gain, and f is the reciprocal of the round trip transit time τ of the delay loop.

repetitive passes through the saturable absorber, it becomes more and more compressed. Correspondingly, its frequency spectrum becomes broader and broader until it is finally limited by the bandwidth of the filter. The steady state pulse width is approximately equal to the reciprocal of the system bandwidth.

In the phonon maser, most of the required elements may be readily identified. The piezoelectric coupling of the acoustic field to drifting electrons provides an amplifying mechanism, a combination of the cavity Fabry - Perot resonances and the gain profile of the phonon maser constitute the filter, and the round trip transit time of the resonant cavity serves as the loop delay. It remains to find something which will provide the necessary saturable absorber effect.

In the case of an ordinary optical laser, which also contains the above 3 basic elements, the saturable absorber must be physically added to the system for RPG operation. One thing that is done, for example, is to place a cell of bleachable dye solution in the laser cavity. Such a dye becomes transparent at very high light intensities, thus providing the necessary characteristic indicated in FIG 1 (a). For some lasers, the gain profile encompasses hundreds of cavity modes. In general all these modes will be running but in a very incoherent manner, so that any pulses existing in the system will be broad and ill-defined. The pulse compression produced by addition of the saturable absorber forces the operating cavity modes into a fixed phase relationship. Hence the origin of the term mode-locking.In this manner picosecond

optical pulses have been achieved.

For the phonon maser it is not possible to isolate a physical element which functions as a saturable absorber. We shall present a qualitative discussion which demonstrates that certain nonlinear properties of the acousto-electric amplifying mechanism provide the necessary behavior.

1.2.1 Nonlinear Gain Theory - The Saturable Absorber

To establish that a mechanism which serves as the counterpart of the saturable absorber exists in the phonon maser, it is necessary to formulate an expression for large amplitude gain. Since mode-locking is a strongly nonlinear process, closely related to such phenomena as D.C. current saturation (Smith 1963) and high electric field domain formation and propagation (Maines 1966, Haydl and Quate 1966), any attempt to extend the linear theory of acoustic amplification (White 1962) will not produce results valid for this situation. The nonlinear theory of acoustic wave propagation in piezoelectric semiconductors has been discussed by many authors: Butcher (1971), Butcher and Ogg (1968, 1969, 1970), Gay and Hartnagel (1969, 1970), Gulayev (1970), Gurevich (1969), Tien (1968), Wanneberger (1970), as well as others.

While the above treatments produce results that are largely similar, the unique approach used by Butcher and Ogg (1968, 1969, 1970) will be adopted since it is quite straight forward and provides results in a transparent and useful form. Since only qualitative expressions are required for our purposes, the finite thickness of the phonon maser

and the ensuing electrical boundary conditions will be ignored. For a discussion of these boundary conditions see Sharma and Wilson (1970). The quasi static approximation (ie. the curl of the electric field = 0) will be employed. This has the effect of decoupling purely electromagnetic waves (propagating at the velocity of light) from acousto-electric waves (propagating at the velocity of sound). Since this corresponds to ignoring terms in the acoustic dispersion which are a factor of $\sim 10^{-10}$ (the square of the ratio of the acoustic velocity to the velocity of light) smaller than other contributions (Hudson and White 1962), it is an excellent approximation. We shall consider the case of uniform plane acoustic waves, propagating along the x axis.† This reduces the problem to a one-dimensional situation. With these considerations the system of equations to be solved becomes (MKS units are employed) :

Elastic wave equation:

$$\frac{\partial T}{\partial x} = \rho \frac{\partial^2 u}{\partial t^2} \tag{1.1}$$

†This is not as unrealistic as it may appear. The physical situation of particular interest corresponds to pure shear waves whose wave vectors lie along the crystallographic b-axis. Results of our optical experiments indicate that a one dimensional analysis is quite reasonable in this case.

Poisson's equation:

$$\frac{\partial D}{\partial x} = q(n - n_o) \tag{1.2}$$

Piezoelectric equations of state:

$$T = cS + eE \tag{1.3}$$

$$D = -eS + \varepsilon E \tag{1.4}$$

Continuity equation:

$$\frac{\partial J}{\partial x} = -q \frac{\partial (n - n_o)}{\partial t} \tag{1.5}$$

Equation of current density:

$$J = qn\mu E - q D_n \frac{\partial n}{\partial x} \tag{1.6}$$

Where T and S are the acoustic stress and strain, u is the mass displacement, ρ is the mass density, E and D are the electric field and electric displacement, q, μ, D_n are the magnitude of the electron charge, the electron mobility and the electron diffusion coefficient, J is the conduction current, c, e, ε, are the appropriate elastic stiffness, piezoelectric and permittivity constants, n is the conduction band electron density and n_o is the equilibrium electron density.

The sign convention of Butcher and Ogg (1968) is employed in

equations (1.1) - (1.6) : E, J and D are measured positive in the negative x direction. This implies that a positive D.C. electric field (ie. pointing in the negative x direction) will produce electron drift, and ultimately acoustic amplification, in the positive x direction. In equations (1.2), (1.5) and (1.6) the effect of holes has been ignored. This is a very good approximation for CdS which is n-type and has a hole mobility and hole lifetime which are approximately 10^{-1} and 10^{-3} times smaller, respectively, than the corresponding electron parameters.

The presence of the acoustic wave produces a variation $\Delta n = (n-n_o)$ in the equilibrium electron density. It is implicitly assumed in the preceeding equations that the space charge $q\Delta n$ is mobile. While this approximation is satisfactory for our purposes, it should be realized that $q\Delta n$ will include a contribution due to modulation of the electron density in localized traps. Thus, in general, only a fraction of the space charge produced by the acoustic wave will be mobile (see McFee 1966).

Combining equations (1.2) and (1.5) to eliminate the term in electron charge, we obtain:

$$\frac{\partial}{\partial x}\left(J + \frac{\partial D}{\partial t} \right) = 0 \qquad (1.7)$$

Expression (1.7) has general validity. For our one-dimensional system it implies that the total current I, consisting of the conduction current J and the displacement current $\partial D/\partial t$ is spatially invariant. This allows us to modify equation (1.6) in the form

$$I = qn\mu E + \frac{\partial D}{\partial t} - q\,Dn\,\frac{\partial n}{\partial x} \tag{1.8}$$

where, according to equation (1.7), I can at most be a function of time. In fact, as will be indicated shortly, I may be assumed to have a constant value in the calculations to be performed.

S, T, E, n and D are assumed to have plane wave dependence of the form

$$D = D_o + D_1 e^{i\theta} + c.c. \tag{1.9}$$

as illustrated for the electric displacement. Here $\theta = Kx - \Omega t$, where K, Ω are the real wavenumber and angular frequency of the wave. D_o is time independent, and D_1 is assumed to be a slowly varying function of x and t compared with the exponential. The D.C. component E_o corresponds to the applied drift field required to operate the phonon maser.

The nonlinearity in the previous equations is contained solely in the term $nq\mu E$ in the expression for current density (equations (1.6) and (1.8)). Thus this term must be explicitly retained to extend the theory into the large amplitude regime. Following Butcher and Ogg (1968), we begin by solving equation (1.8) for E and making use of equation (1.2) to obtain

$$E = \frac{I - \frac{\partial D}{\partial t} + D_n \frac{\partial^2 D}{\partial x^2}}{\sigma\left(1 + \frac{1}{qn_o}\frac{\partial D}{\partial x}\right)} \tag{1.10}$$

where $\sigma = n_o q \mu$

The nonlinear behavior is now expressed by the denominator in equation (1.10), as may be seen by expanding this term in powers of $(qn_o)^{-1}\ \partial D/\partial x$. With the use of equation (1.9) and the substitution

$$A = \frac{2iKD_1}{qn_o} \tag{1.11}$$

equation (1.10) may be written:

$$E = \frac{I + \frac{qn_o}{2}\left((v_s + iKD_n)\, Ae^{i\theta} + c.c. \right)}{\sigma\left(1 + \left(\frac{A}{2} e^{i\theta} + c.c. \right) \right)} \tag{1.12}$$

where $v_s = \frac{\Omega}{K}$ = velocity of sound. In obtaining equation (1.12) the derivatives of D_1 have been neglected in comparison with the derivatives of the exponential term. From the previous discussion it is apparent that all nonlinear behavior is now embodied in the parameter A. A has a simple physical interpretation. Solving equation (1.2) for n and using equations (1.9) and (1.11) we obtain (again neglecting derivatives of D_1):

$$n = n_o \left(1 + \frac{A}{2} e^{i\theta} + \frac{A^*}{2} e^{-i\theta} \right) \tag{1.13}$$

or, writing A in polar form $|A|e^{i\phi}$:

$$n = n_o \left[1 + |A| \cos(\theta+\phi) \right] \tag{1.14}$$

Thus A specifies the amplitude and phase of the electron density wave. Since n in equation (1.14) cannot be negative, the present analysis imposes the following constraint:

$$0 \leq |A| \leq 1 \tag{1.15}$$

In a broader sense, A provides an extremely convenient parameter for determining amplitude dependent expressions for the variables involved, as for E in equation (1.12). The linear theory of White (1962) may be recovered in the limit $|A| \to 0$.

The D.C. and A.C. components of E may be extracted from equation (1.12) by performing the following phase averages:

$$E_o = \frac{1}{2\pi} \int_0^{2\pi} E d\theta \tag{1.16}$$

$$E_1 = \frac{1}{2\pi} \int_0^{2\pi} E e^{i\theta} d\theta \tag{1.17}$$

In the slowly varying envelope approximation already outlined, D_1 may be treated as a constant in carrying out the integrations. Also, since D, E and n have the form shown in equation (1.9), the RHS of equation (1.8) may be treated as solely a function of θ for the integrations in (1.16) and (1.17). Thus I, which has been shown to be at most a function of time, may be treated as a constant in equations (1.16) and (1.17).

Using equation (1.12) and the standard substitution $z = e^{i\theta}$, the integrals in (1.16) and (1.17) may be converted to contour integrals around the unit circle in the complex plane. One then obtains:

$$E_o = E_s \left[1 - \frac{(1 - \frac{I}{I_s})}{(1 - |A|^2)^{\frac{1}{2}}} \right] \tag{1.18}$$

$$E_1 = \frac{E_s A}{1 + (1 - |A|^2)^{\frac{1}{2}}} \left[\frac{(1 - \frac{I}{I_s})}{(1 - |A|^2)^{\frac{1}{2}}} + \frac{i\Omega}{\omega_D} \right] \tag{1.19}$$

The notation used is the same as Butcher and Ogg (1968):

$E_s = \frac{v_s}{\mu}$ is the synchronous electric field, i.e. the field required to produce an electron drift velocity equal to the velocity of sound.

$I_s = n_o q v_s$ is the synchronous current.

$\omega_D = \frac{v_s^2}{D_n}$ is the diffusion frequency.

Equation (1.18) may be rearranged to yield:

$$\frac{(1 - \frac{I}{I_s})}{(1 - |A|^2)^{\frac{1}{2}}} = \gamma \qquad (1.20)$$

where $\gamma = 1 - \frac{E_o}{E_s} = 1 - \frac{v_D}{v_s}$; v_D = electron drift velocity (1.21)

Substituting equation (1.20) into equation (1.19) yields a relationship between E_1 and D_1:

$$E_1 = \frac{i\Omega D_1}{\varepsilon \omega_c'} \left(\gamma + \frac{i\Omega}{\omega_D} \right) \qquad (1.22)$$

where

$$\omega_c' = \tfrac{1}{2}\, \omega_c \left[1 + (1 - |A|^2)^{\frac{1}{2}} \right] \qquad (1.23)$$

$\omega_c = \frac{\sigma}{\varepsilon}$ is the conductivity relaxation frequency.

To find the expression for acoustic gain, we obtain a wave equation by substituting equation (1.3) into (1.1) to yield (using $v_s^2 = \frac{c}{\rho}$):

$$\frac{\partial^2 u}{\partial t^2} - v_s^2 \frac{\partial S}{\partial x} = \frac{e}{\rho} \frac{\partial E}{\partial x} \qquad (1.24)$$

Taking the derivative with respect to x on both sides of (1.24) and using the relation $S = \frac{\partial u}{\partial x}$:

$$\frac{\partial^2 S}{\partial t^2} - v_s^2 \frac{\partial^2 S}{\partial x^2} = \frac{e}{\rho} \frac{\partial^2 E}{\partial x^2} \tag{1.25}$$

The plane wave forms of S and E [see equation (1.9)] may now be substituted into equation (1.25). In keeping with the slowly varying envelope approximation, only the dominant terms on both sides of the equation will be retained. On the LHS there are no terms in S_1 and the first derivatives of S_1 are therefore retained. We obtain:

$$\frac{\partial S_1}{\partial t} e^{i\theta} - \frac{\partial S_1^*}{\partial t} e^{-i\theta} + v_s \frac{\partial S_1}{\partial x} e^{i\theta} - v_s \frac{\partial S_1^*}{\partial x} e^{-i\theta}$$

$$= \frac{K}{2iv_s} \frac{e}{\rho} \left(E_1 e^{i\theta} + E_1^* e^{-i\theta} \right) \tag{1.26}$$

Equating the coefficients of $e^{i\theta}$ on both sides of (1.26):

$$\frac{\partial S_1}{\partial t} + v_s \frac{\partial S_1}{\partial x} = \frac{K}{2iv_s} \frac{e}{\rho} E_1 \tag{1.27}$$

With the aid of equation (1.22) and using equation (1.4) in the form $D_1 = -eS_1 + \varepsilon E_1$, E_1 may be related to S_1 and one finally obtains:

$$\frac{\partial S_1}{\partial t} + v_s \frac{\partial S_1}{\partial x} = \alpha_c v_s S_1 \tag{1.28}$$

where

$$\alpha_c = \frac{\chi\Omega}{2v_s} \frac{\left(\gamma + \frac{i\Omega}{\omega_D} \right)}{\left(i\gamma - \frac{\Omega}{\omega_D} - \frac{\omega_c'}{\Omega} \right)} \tag{1.29}$$

The real and imaginary parts of α_c are given by:

$$\alpha \equiv \text{Re } \alpha_c = -\frac{\chi}{2v_s} \left(\frac{\gamma\omega_c'}{\gamma^2 + \left(\frac{\Omega}{\omega_D} + \frac{\omega_c'}{\Omega} \right)^2} \right) \tag{1.30}$$

$$\Delta K \equiv \text{Im } \alpha_c = -\frac{\chi\Omega}{2v_s} \left(\frac{\gamma^2 + \frac{\Omega}{\omega_D} \left(\frac{\Omega}{\omega_D} + \frac{\omega_c'}{\Omega} \right)}{\gamma^2 + \left(\frac{\Omega}{\omega_D} + \frac{\omega_c'}{\Omega} \right)^2} \right) \tag{1.31}$$

$\chi = \frac{e^2}{\varepsilon\rho v_s^2}$ is the piezoelectric coupling coefficient.

From the form of the general solution for equation (1.28), it may be readily inferred that α in equation (1.30) is the nonlinear acoustic gain coefficient, while ΔK in equation (1.31) specifies the phase shift of the acoustic wave produced by piezoelectric coupling.

Equations (1.30) and (1.31) only differ from the corresponding expressions in linear theory by the substitution of ω_c' for ω_c [see equation (1.23)]. In the limit $|A| \to 0$, $\omega_c' \to \omega_c$ and linear theory is recovered. The frequency of maximum gain is given by $(\omega_c'\omega_D)^{\frac{1}{2}}$ [White 1962]. From equation (1.23) it is apparent that the frequency of maximum gain is reduced by about 30% as $|A|$ increases from 0 to 1.

To use equation (1.30) in the expression for total round trip gain in the phonon maser, it is necessary to account for acoustic waves travelling both parallel and antiparallel to the applied D.C. electric field E_o. This is achieved by setting γ in equation (1.30) equal to:

$$\gamma_- = 1 - \frac{v_D}{v_s} \tag{1.32a}$$

for acoustic waves travelling antiparallel to E_o, and

$$\gamma_+ = 1 + \frac{v_D}{v_s} \tag{1.32b}$$

for acoustic waves travelling parallel to E_o.

The total round trip gain G in the phonon maser may be written (Gurevich 1969):

$$G = \alpha_+ + \alpha_- + 2\Gamma - \frac{2\ln r}{d} \tag{1.33}$$

where α_+ (α_-) is given by substituting γ_+ (γ_-) into equation (1.30). Γ is the lattice loss coefficient, r is the acoustic reflectivity of

the phonon maser cavity wall, and d is the cavity thickness. For the lattice loss Γ we use the empirical relation (Maines and Paige 1969):

$$\Gamma = \delta\Omega^{\beta} \text{ (cm)}^{-1} \tag{1.34}$$

where $\delta = 1.11 \times 10^{-14}$; $\beta = 1.51$

In FIG 2(a) and (b) the value of G corresponding to the frequency of maximum gain is plotted as a function of $|A|$, under different conditions of conductivity and applied D.C. electic field. The parameters used in the calculation were $\omega_D = 4.38 \times 10^9$Hz, $\mu = 280$ cm^2/volt-sec., $\chi = 0.0378$ and $v_s = 1.759 \times 10^5$ cm/sec. (the value for μ was calculated from the threshold electric field for $b_\perp$ crystal 24.01.02.04). A value of 1.5 was used for the end loss term $-2\ln r/d$. As is indicated in FIG 2, conditions can be realized such that G increases with increasing $|A|$, and hence with increasing acoustic amplitude.

It is this nonlinear property that provides the counterpart of the saturable absorber, and completes the analogy between the phonon maser and the repetitive pulse generator. The phenomenon of mode-locking can thus be predicted as a natural consequence of the physical properties and structure of the phonon maser. The theoretical behavior of the phonon maser as a function of conductivity and applied electric field is summarized in FIG 3. The region of oscillation is indicated by cross-hatching. The regime of the "saturable absorber" corresponds to the shaded area near the top of the region of oscillation.

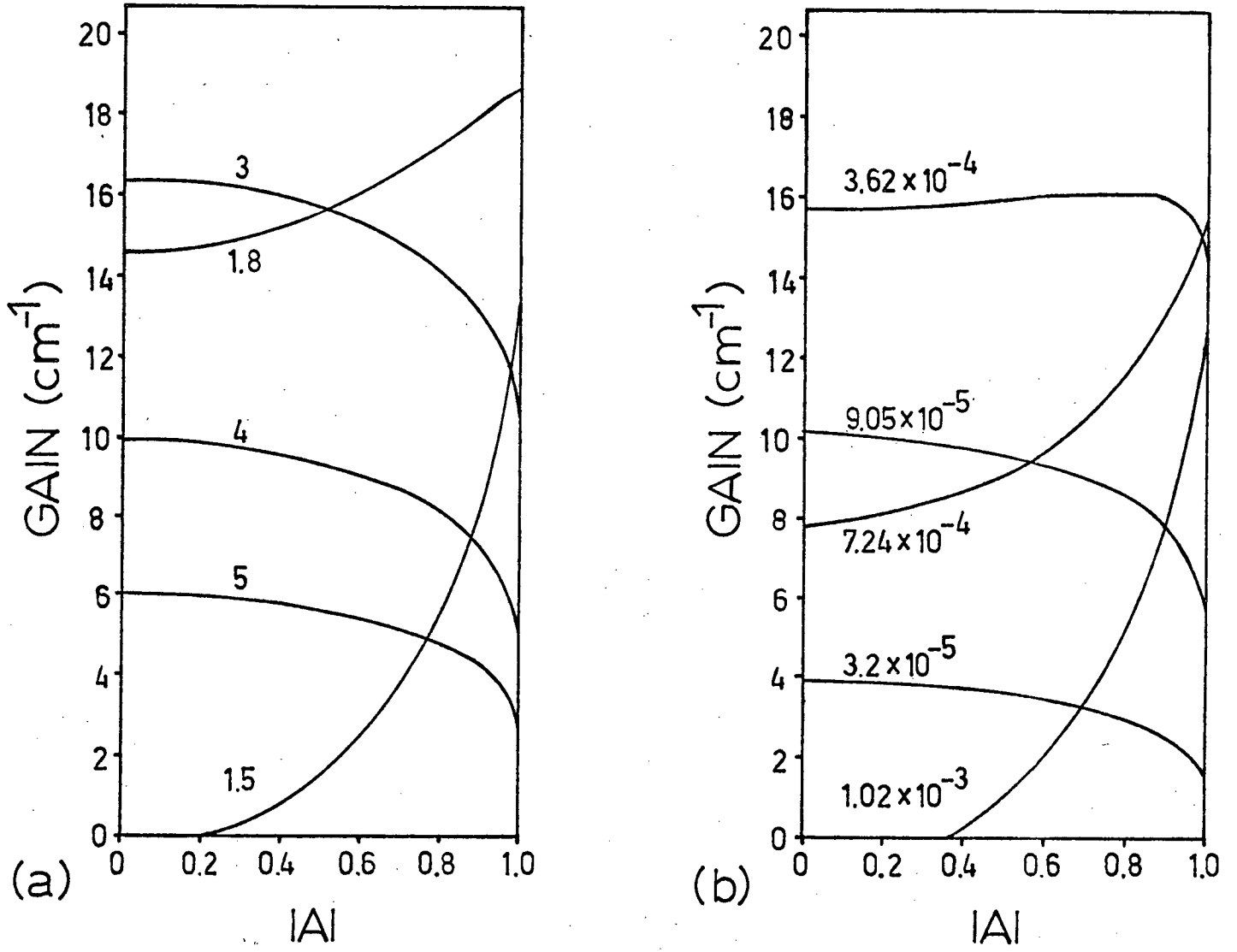

FIG 2. Nonlinear gain as a function of $|A|$, computed at the frequency of maximum gain. (a) $\sigma = 10^{-3}(\Omega cm)^{-1}$, parameter = v_D/v_s. (b) $v_D/v_s = 1.5$, parameter = $\sigma(\Omega cm)^{-1}$.

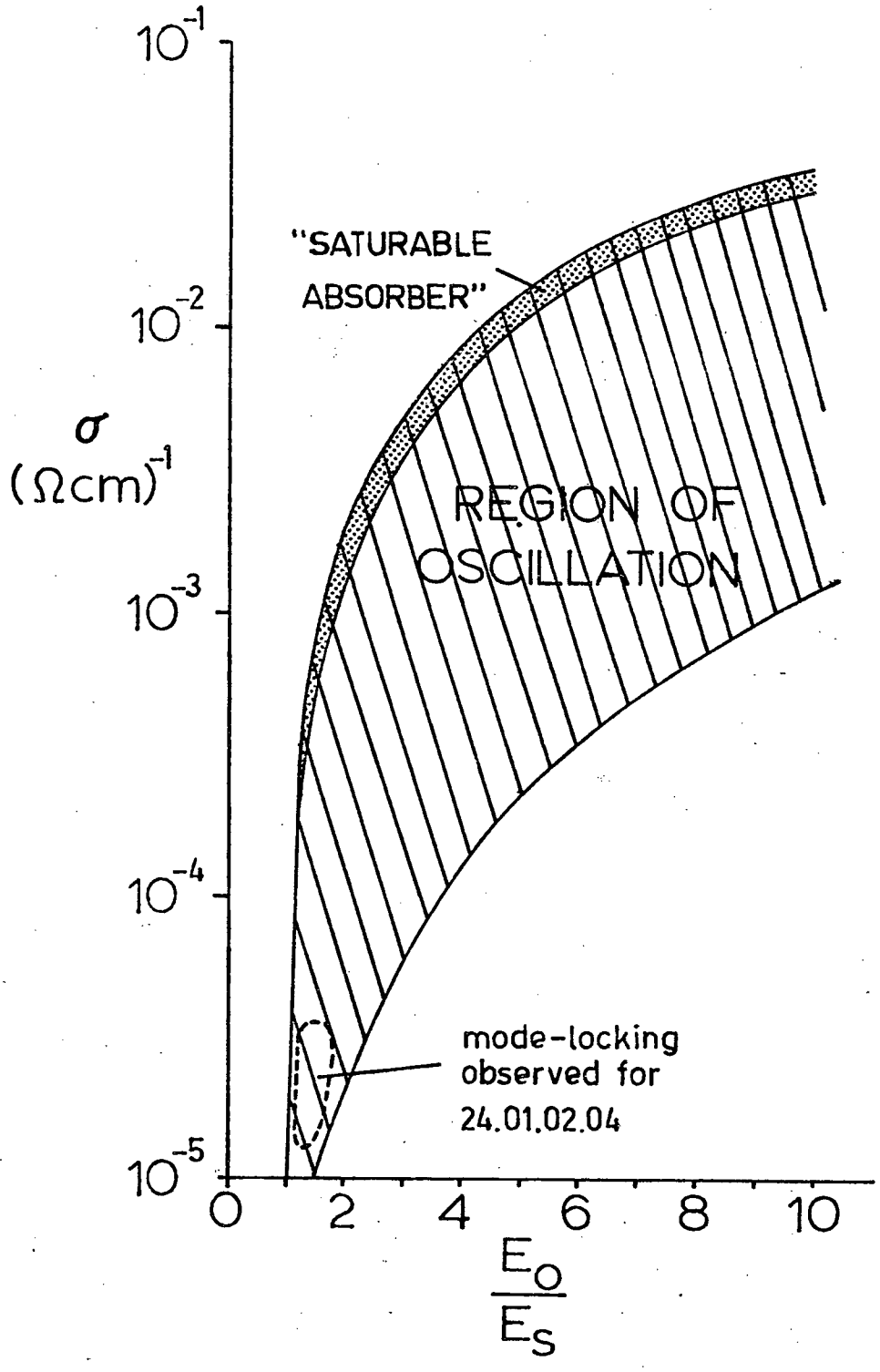

FIG 3. Behavior of the phonon maser as a function of conductivity σ and applied electric field E_o. E_s is the synchronous electric field.

The small area enclosed by a dotted line near the bottom of the figure corresponds to the regime where mode-locked operation was observed for $b\perp$ crystal 24.01.02.04. As is indicated, mode-locking was achieved at conductivities approximately an order of magnitude lower than predicted by theory.

It is worthwhile to discuss the limitations of the theory. First of all, consider the maximum allowable value for the amplitude E_1 of the self consistent A.C. electric field. From equation (1.19), with $|A| = 1$, we observe that

$$|E_1|_{Max} = E_s \left|\gamma + \frac{i\Omega}{\omega_D}\right| \tag{1.35}$$

For typical operating frequencies, it is reasonable to neglect $i\Omega/\omega_D$ in comparison with γ. Thus

$$|E_1|_{Max} \simeq E_o - E_s \tag{1.36}$$

Since $E_o/E_s \sim 1.2\text{-}2.0$, for the experiments performed, equation (1.36) predicts that $|E_1|_{Max} < 0.5E_o$. In fact, values of E_1 of the order of $2E_o$ have been inferred from experimental measurements.

As a further consideration, the behavior of the total current density as a function of $|A|$ should be examined. We observe first of all from equation (1.14) that $|A| = 1$ corresponds to a situation of complete electron depletion at the minima of the electron density wave.

This corresponds to D.C. current saturation as may be seen more concretely in the following manner. If equation (1.18) is solved for I, the resulting expression may be written in the form:

$$I = \sigma E_o (1 - F) + I_s F \tag{1.37}$$

where

$$F = 1 - (1 - |A|^2)^{\frac{1}{2}} \tag{1.38}$$

From equation (1.37) we see that the total current density I behaves as if a fraction F of the electrons were constrained to move at the velocity of sound, while the rest exhibit normal ohmic response to the local D.C. electric field. Thus F may be considered to be a trapping fraction in the sense that it specifies the portion of available electrons that are trapped in the potential wells produced by the acoustic wave. Since F increases monotonically from 0 to 1 as $|A|$ increases from 0 to 1, for $|A| = 1$, $I = I_s$ independent of the applied field E_o. Thus the present theory takes us up to the point of complete current saturation. The region of mode-locked operation is, in fact, well into the regime of current saturation.

The above limitations may be traced to the fact that we have assumed a sinusoidal electron density distribution [equation (1.14)]. As has been indicated in section 1.1, this will not be a good assumption in the case of very large acoustic amplitudes. The theory may be generalized to incorporate a more physical charge density profile by writing all variables in the form of a general Fourier expansion, and

then proceeding in much the same manner as in this section (see Butcher and Ogg 1969). For realistic profiles, however, numerical methods must be applied (see Butcher and Ogg 1970 and Tien 1968). Our purpose has not been to describe mode-locked operation per se, but to present a plausibility argument for the existence of a "saturable absorber".

1.3 Theory of the Optical Measurements

The necessary background for interpretation of the optical experiments is developed in this section. To demonstrate the usefulness of light diffraction in the study of acoustic fields, we begin by considering the photoelastic effect (Nye 1964).

1.3.1 Crystal Optics - The Photoelastic Effect

The optical properties of an anisotropic crystal are conveniently embodied in a quadric surface known as the indicatrix. It may be defined in its general form by (Nye 1964):

$$B_{ij}x_i x_j = 1 \tag{1.39}$$

where B_{ij} are components of the relative dielectric impermeability tensor defined by

$$B_{ij} = \varepsilon_o \frac{\partial E_i}{\partial D_j} \tag{1.40}$$

E_i and D_j are components of the electric field and electric displacement, and ε_o is the vacuum permittivity. If the coordinate axes x_1, x_2, x_3 are chosen to lie along the crystallographic directions which correspond to the principal axes of the dielectric tensor, equation (1.39) reduces to

$$\frac{x_1^2}{n_1^2} + \frac{x_2^2}{n_2^2} + \frac{x_3^2}{n_3^2} = 1 \tag{1.41}$$

where $\kappa_1 = n_1^2$, $\kappa_2 = n_2^2$ and $\kappa_3 = n_3^2$ are the principal dielectric constants, and n_1, n_2, n_3 are referred to as the principal refractive indices. The quadric surface defined by equation (1.41) is an ellipsoid with semiaxes n_1, n_2, n_3.

This surface has a valuable property that can be illustrated by the geometrical construction in FIG 4(a). Consider that light propagating in direction CO (O is the ellipsoid origin) impinges on the crystal. A central section of the indicatrix is made perpendicular to CO. This section will be an ellipse and is referred to as the "index ellipse". In FIG 4 the index ellipse is emphasized by shading and in FIG 4(b) is viewed along the direction of incident light (i.e. light is propagating into the page). If the incident light has its electric displacement vector $\vec{D}$ polarized in the direction indicated in FIG 4(b), it will propagate in the medium as the two independent components D_1 and D_2, which are polarized along the axes of the index ellipse. D_1, D_2 will have refractive indices equal to OA and OB, respectively. For OA $\neq$ OB (the index ellipse is not a circle) the medium exibits birefringence or double refraction, and when the light emerges from the crystal the two components D_1 and D_2 will recombine to form, in general, elliptically polarized light. For light having its wave normal parallel to one of the indicatrix axes, the two independent waves in the material will have refractive indices corresponding to the principal indices in equation (1.41). For example, light propagating along the x_3 axis will have refractive indices n_1 and n_2 [see FIG 4(a)].

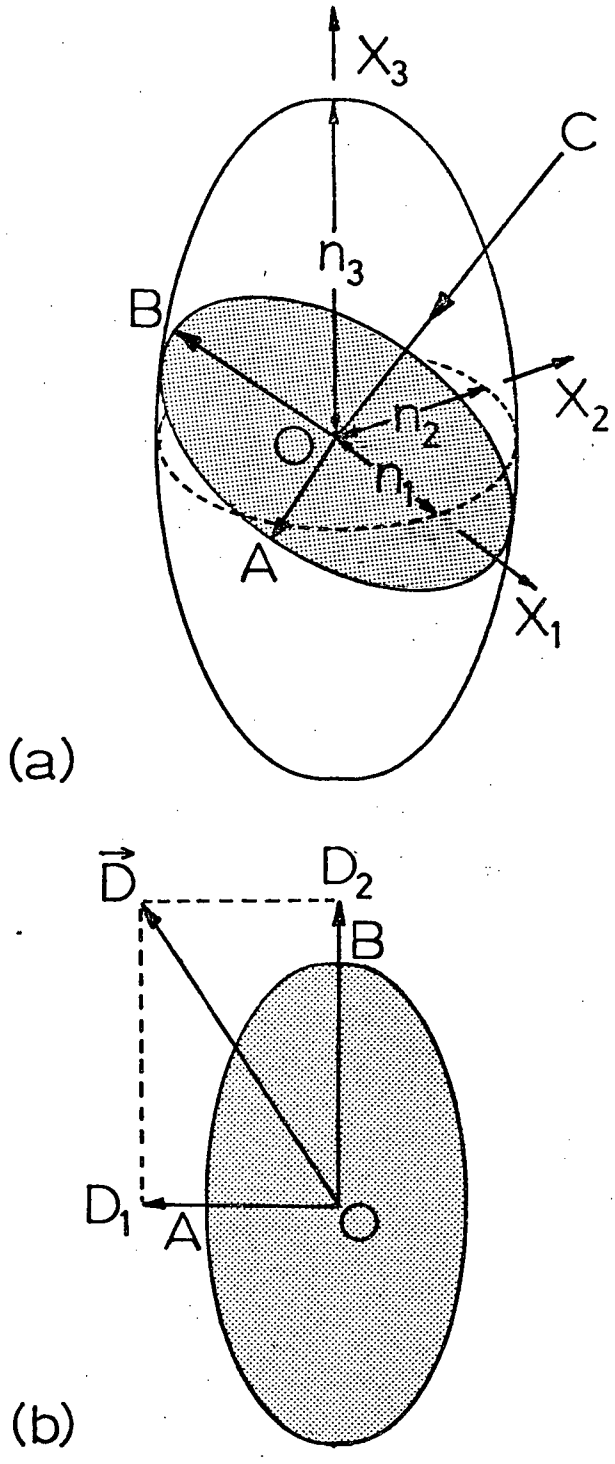

FIG 4. (a) Indicatrix construction for optical wave normal CO. The index ellipse is shaded. (b) Index ellipse viewed along direction of light propagation. The polarization of the incident light is specified by the electric displacement vector $\vec{D}$.

The shape of the indicatrix depends upon the symmetry of the medium in question. For cubic or isotropic materials, which possess one principal refractive index, it is a sphere. Hence all central sections are circles and there is no natural birefringence. For hexagonal, tetragonal and trigonal crystals there are two principal refractive indices, and the indicatrix is an ellipsoid of revolution having the form

$$\frac{x_1^2}{n_o^2} + \frac{x_2^2}{n_o^2} + \frac{x_3^2}{n_e^2} = 1 \qquad (1.42)$$

where n_o and n_e are termed the ordinary and extraordinary refractive indices. In general, central sections of (1.42) will be ellipses, implying the existence of natural birefringence. The central section perpendicular to the x_3 axis is a circle, however, and for this unique direction there is no birefringence. x_3 is called the principal or optic axis and such crystals are termed uniaxial. CdS has hexagonal crystal structure and hence is an example of a uniaxial crystal. For CdS, x_1, x_2, x_3 in equation (1.42) correspond to the a, b and c axes, respectively. For the remaining crystal classes there are 3 principal refractive indices and the indicatrix is a triaxial ellipsoid.

The permittivity and dielectric constant, and hence the index of refraction are, in general, modified by the introduction of elastic strain in a crystal. Thus the presence of an acoustic wave will be indicated by a modulation of the local refractive index which may,

in turn, be expressed in terms of small changes in the shape, size and orientation of the indicatrix. If we consider only effects that are linear in the applied strain, the change induced in the indicatrix may be written (Nye 1964):

$$\Delta B_{ij} = p_{ijkl} S_{kl} \tag{1.43}$$

p_{ijkl} and S_{kl} are components of the optoelastic and strain tensors. The strain tensor is related to the mass displacements u_i by:

$$S_{ij} = \tfrac{1}{2} \left(\frac{\partial u_i}{\partial x_j} + \frac{\partial u_j}{\partial x_i} \right) \tag{1.44}$$

If the shear strains ($i \neq j$) are redefined in equation (1.44) by omitting the factor of $\tfrac{1}{2}$, the indices in equation (1.43) may be contracted unambiguously according to the following scheme (Nye 1964):

$11 \rightarrow 1$	$32,\ 23 \rightarrow 4$
$22 \rightarrow 2$	$31,\ 13 \rightarrow 5$
$33 \rightarrow 3$	$21,\ 12 \rightarrow 6$

(1.45)

This allows equation (1.43)to be represented in matrix form.

Under the influence of strain the indicatrix ellipsoid represented by equation (1.41) will be transformed, and the new ellipsoid may be described by [refer to equation (1.39)]:

$$B_1x_1^2 + B_2x_2^2 + B_3x_3^2 + 2B_4x_2x_3 + 2B_5x_1x_3 + 2B_6x_1x_2 = 1 \qquad (1.46)$$

With reference to equations (1.41), (1.45) and (1.46), equation (1.43) may be written in matrix form:

$$\begin{pmatrix} \Delta B_1 \\ \Delta B_2 \\ \Delta B_3 \\ \Delta B_4 \\ \Delta B_5 \\ \Delta B_6 \end{pmatrix} = \begin{pmatrix} B_1 - 1/n_1^2 \\ B_2 - 1/n_2^2 \\ B_3 - 1/n_3^2 \\ B_4 \\ B_5 \\ B_6 \end{pmatrix} = \begin{pmatrix} p_{11} \cdots p_{16} \\ p_{21} \cdots p_{26} \\ p_{31} \cdots p_{36} \\ p_{41} \cdots p_{46} \\ p_{51} \cdots p_{56} \\ p_{61} \cdots p_{66} \end{pmatrix} \times \begin{pmatrix} S_1 \\ S_2 \\ S_3 \\ S_4 \\ S_5 \\ S_6 \end{pmatrix} \qquad (1.47)$$

When the form of the strain is known, the new indicatrix may be found from equations (1.46) and (1.47). With this information one is able to determine the new polarizations and indices of refraction for a given optical wave normal, using the indicatrix property illustrated by FIG 4. The general problem provides a tedious exercise in algebra and analytic geometry. General solutions have been obtained for crystals with hexagonal 6mm symmetry by Vrba and Haering (1973), and provide a useful model for solving other crystal structures.

A much simpler case, that of a shear wave propagating in an optically and acoustically isotropic medium, will be treated to illustrate the use of the indicatrix. This situation is of particular interest and the results will be used in later sections. In the absence of strain the

indicatrix is a sphere and equation (1.41) becomes:

$$\frac{1}{n_o^2}\left(x_1^2 + x_2^2 + x_3^2 \right) = 1 \tag{1.48}$$

The coordinate system is chosen so that the acoustic wave normal lies along the x_1 axis, with mass displacement along the x_2 axis. Thus the only non-zero strain component is S_6. For an isotropic material the optoelastic matrix becomes (Nye 1964):

$$\begin{pmatrix} p_{11} & p_{12} & p_{12} & 0 & 0 & 0 \\ p_{12} & p_{11} & p_{12} & 0 & 0 & 0 \\ p_{12} & p_{12} & p_{11} & 0 & 0 & 0 \\ 0 & 0 & 0 & p_{44} & 0 & 0 \\ 0 & 0 & 0 & 0 & p_{44} & 0 \\ 0 & 0 & 0 & 0 & 0 & p_{44} \end{pmatrix} \tag{1.49}$$

where $p_{44} = \frac{1}{2}(p_{11} - p_{12})$. Equation (1.47) then yields:

$$\begin{pmatrix} \Delta B_1 \\ \Delta B_2 \\ \Delta B_3 \\ \Delta B_4 \\ \Delta B_5 \\ \Delta B_6 \end{pmatrix} = \begin{pmatrix} 0 \\ 0 \\ 0 \\ 0 \\ 0 \\ p_{44} S_6 \end{pmatrix} \tag{1.50}$$

From equations (1.48) and (1.50), the coefficients in equation (1.46) may be readily inferred:

$$B_1 = B_2 = B_3 = \frac{1}{n_o^2}$$

$$B_4 = B_5 = 0 \qquad (1.51)$$

$$B_6 = p_{44} S_6$$

The new indicatrix thus becomes:

$$\frac{1}{n_o^2} \left(x_1^2 + x_2^2 + x_3^2 \right) + 2p_{44} S_6 x_1 x_2 = 1 \qquad (1.52)$$

If x_3 is chosen as the optical wave normal, the appropriate index ellipse is given by setting $x_3 = 0$ in equation (1.52) to obtain:

$$\frac{1}{n_o^2} \left(x_1^2 + x_2^2 \right) + 2p_{44} S_6 x_1 x_2 = 1 \qquad (1.53)$$

The form of the index ellipse, both in the presence and absence of the perturbing strain, is shown in FIG 5. As is indicated, the axes of the index ellipse are rotated by $\pi/4$ with respect to the coordinate axes x_1 and x_2. We therefore change to a rotated frame using the transformation:

$$x_1 = 1/\sqrt{2} \left(x_1' + x_2' \right)$$

$$x_2 = 1/\sqrt{2} \left(x_2' - x_1' \right) \qquad (1.54)$$

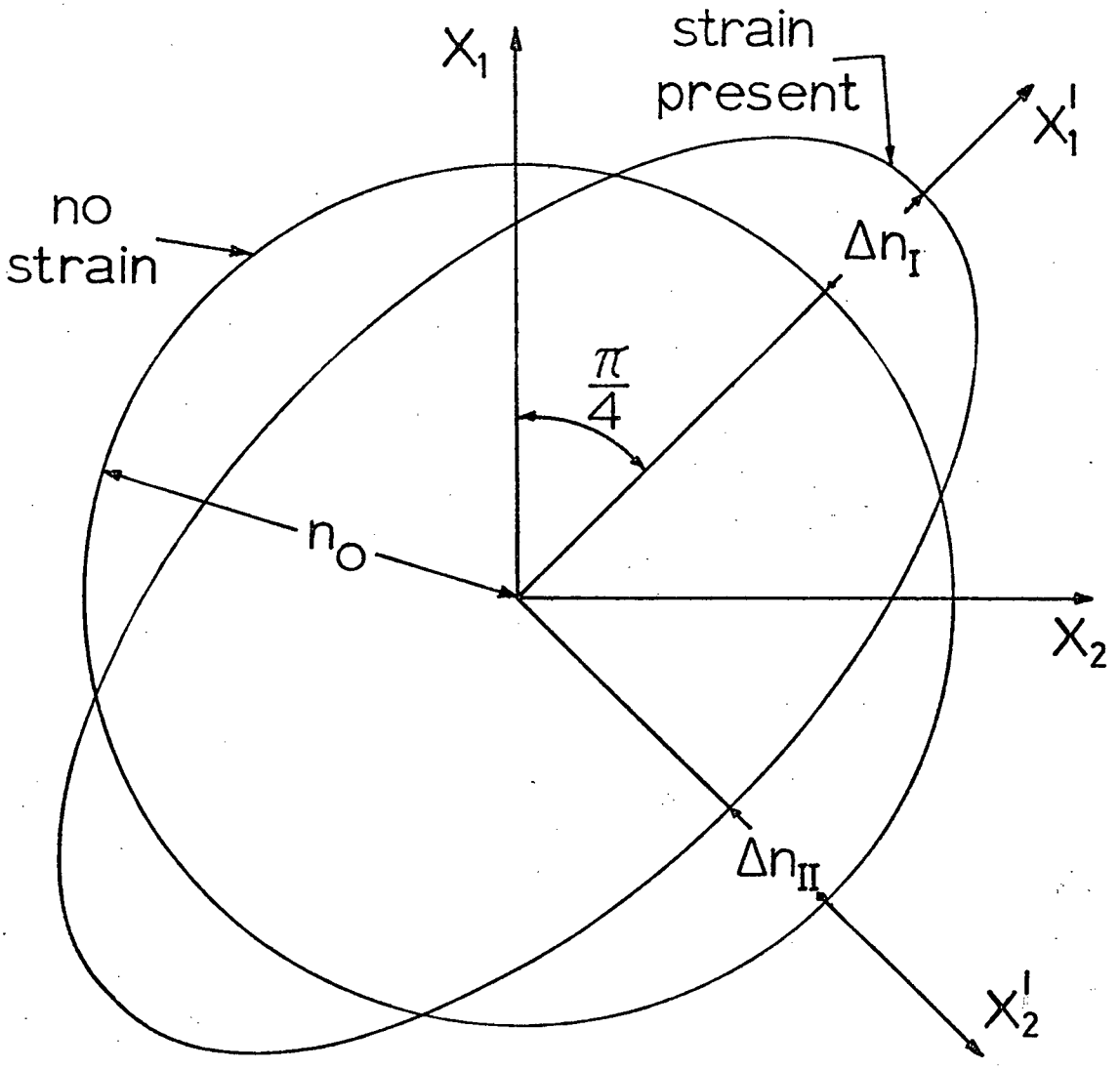

FIG 5. Form of the index ellipse in an isotropic material for optical wave normal x_3, both in the presence and absence of shear srain S_6.

so that the new coordinate axes x_1', x_2' are colinear with the axes of the ellipse. Equation (1.53) then reduces to the more standard form:

$$\frac{x_1'^2}{n_I^2} + \frac{x_2'^2}{n_{II}^2} = 1 \tag{1.55}$$

where

$$n_I = \frac{n_o}{(1 - p_{44}S_6n_o^2)^{\frac{1}{2}}}$$

$$n_{II} = \frac{n_o}{(1 + p_{44}S_6n_o^2)^{\frac{1}{2}}} \tag{1.56}$$

For typical experimental parameters $p_{44}S_6n_o^2 \leq 10^{-5}$, so to a very good approximation we may expand the square roots in (1.56) and retain only linear terms:

$$n_I \simeq n_o (1 + \tfrac{1}{2} p_{44}S_6n_o^2)$$

$$n_{II} \simeq n_o (1 - \tfrac{1}{2} p_{44}S_6n_o^2) \tag{1.57}$$

It is readily apparent from equation (1.57) that the changes in refractive index produced by the strain (see FIG 5) are:

$$\Delta n_I = -\Delta n_{II} = \tfrac{1}{2} p_{44}S_6n_o^3 \tag{1.58}$$

The time dependence of the acoustic wave has thus far been

neglected. FIG 5 is essentially a picture of the index ellipse at one instant of time. For sinusoidal time dependence, we may imagine that at time ¼ T later, where T is the period of the acoustic wave, the index ellipse will be a circle; at time ½ T it will again be an ellipse, but with the major axis now lying along x_2' ; and so on. In this manner, the local index ellipse may be visualized as pulsating with the frequency of the acoustic wave.

It is worth mentioning that, for a given strain, the wave normal of the incident light must be judiciously chosen. If in the present case, for example, the optical wave normal is taken as x_1 or x_2, it may be seen from equation (1.52) that the appropriate central sections ($x_1 = 0$ and $x_2 = 0$) are circular and completely unaltered by the strain. Thus a knowledge of the predeeding theory is essential in determining the configuration for optical experiments.

1.3.2 Interpretation of the Optical Signal - Preliminary Considerations

The intimate relationship between the refractive index and the local strain, outlined in the previous section, makes light diffraction a powerful tool in the study of the phonon maser. In order to proceed to an optical analysis of the strain profiles in a mode-locked phonon maser, it is necessary to first establish the relationship between the optical signals derived by light diffraction, and the acoustic fields that provide the diffracting mechanism. This subject has an extensive literature and will not be fully developed here [the general theory of ultrasonic light diffraction has been discussed

by Bhatia and Noble (1953) and by Klein, Cook and Mayer (1965)]. A categorized bibliography is provided at the end of this thesis.

The configuration of physical interest is depicted in FIG 6. An acoustic cavity of width L is illuminated by a unit amplitude plane light wave, propagating in the xz plane (plane optical wavefronts may be reasonably approximated in practise, since laser beams with wavefront distortions less than 0.2 optical wavelengths may be prepared by careful collimation). The optical waveform emerging from the far side ($z = L$) of the acoustic cavity is transformed due to acoustically induced modulations in the local refractive index. The near field optical distribution (i.e. the optical signal at $z = L$), denoted A_o, is imaged by a converging lens.

The direction of acoustic propagation is taken as the x-axis in FIG 6, and the acoustic waveform is assumed to have spatial variation only in the x-direction. Hence the near field distribution A_o is a function only of x and t. This assumption requires some comment. In practice, the field of view is determined by the cross section of the incident laser beam. Since the beam size used in experimental situations was smaller than the dimensions of the acoustic cavity, distortions in acoustic wavefronts introduced by edge effects were avoided and, as will be verified by the experimental results, the assumption of a one dimensional system is valid.

In the focal plane of a converging lens the criterion for Fraunhofer diffraction is satisfied (Goodman 1968). This is intuitively clear since in front of the focal plane light waves are converging and

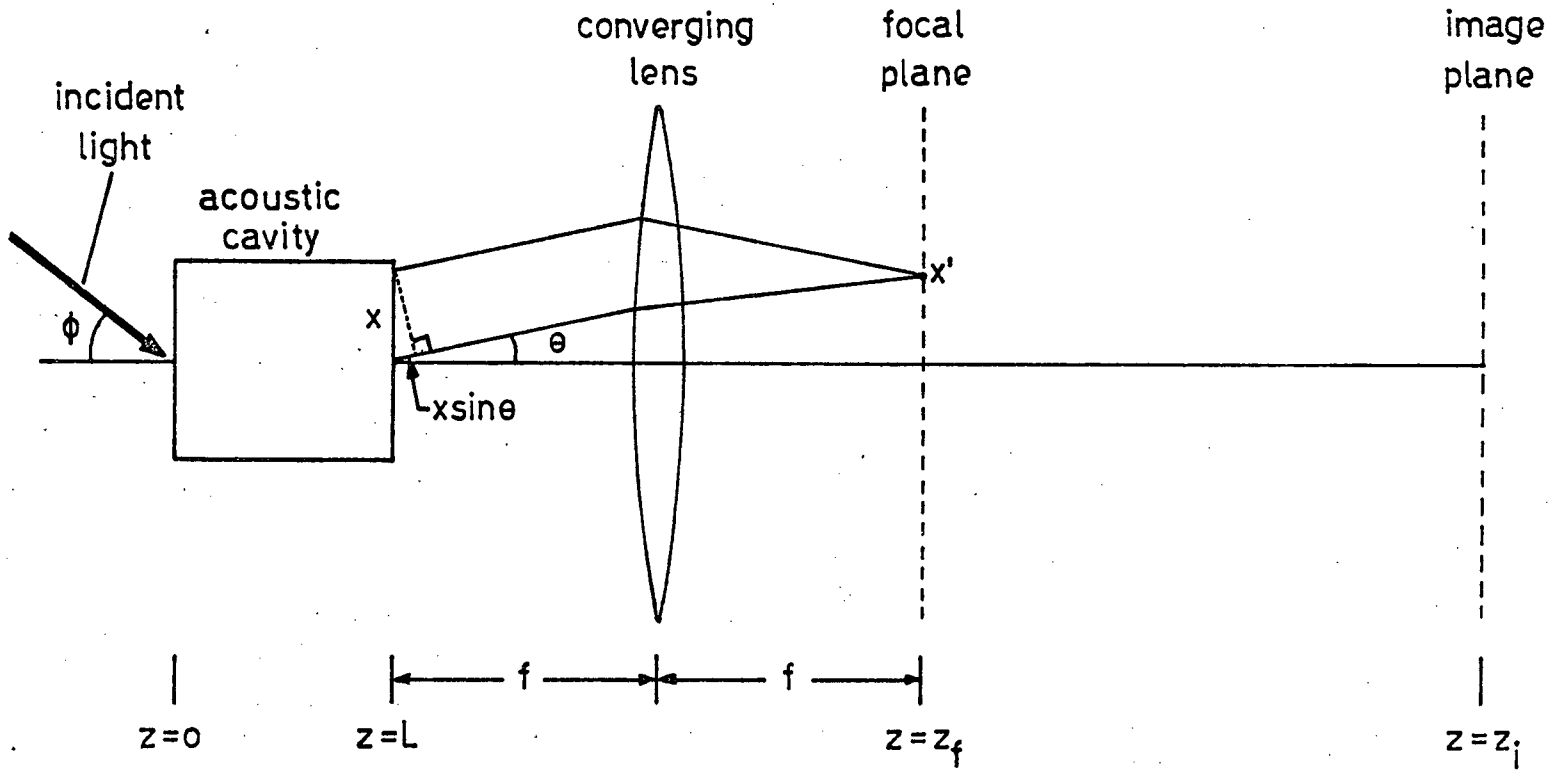

FIG 6. Schematic representation of the optical system to be studied.

behind it they are diverging. Hence at $z = z_f$ in FIG 6 we have plane optical wavefronts. In the limit of small diffraction angles ($\lesssim 18°$), the optical distribution in the focal plane, $A_f(x',t)$, is related to the near field distribution by a one dimensional form of the familiar Fraunhofer diffraction integral (Goodman 1968):

$$A_f(x',t) = \xi \int_{-\frac{W}{2}}^{\frac{W}{2}} A_o(x,t) e^{-ikx \sin\theta} dx \qquad (1.59)$$

where ξ is a phase factor determined by the physical configuration and W is the effective width of the optical beam. If we imagine two parallel rays, separated by distance x in the near field, and making an angle θ with the z axis, the term $\exp(-ikx \sin\theta)$ equals the difference in optical phase suffered by the two rays in propagating to point x' in the focal plane (see FIG 6).

The beam width W is assumed to be large compared with the acoustic wavelengths so that all diffraction orders in the focal plane are well resolved and completely separated. For this situation, we impose no restrictions on the spatial filtering experiments to be carried out, by extending the limits of integration in (1.59) to $\pm \infty$. In addition, it may be shown that the phase factor ξ reduces to unity when the separation between the near field region (object plane) and the lens is equal to the focal length of the lens (Goodman 1968). With these considerations equation (1.59) becomes:

$$A_f(x',t) = \int_{-\infty}^{\infty} A_o(x,t)e^{ik'x}dx \qquad (1.60)$$

where $k' = k \sin\theta$. There is a one to one relationship between x' and k' in equation (1.60) since specifying x' uniquely determines θ and vice-versa. Hence equation (1.60) indicates that the optical distribution in the focal plane is the Fourier transform of the near field signal. This Fourier transforming capability is a general property of converging lenses (Goodman 1968).

In propogating from the focal plane to the image plane in FIG. 6, the optical signal suffers an inverse Fourier transform. For a distortion free optical system, there is then a one to one relationship (aside from a spatial magnification factor) between the optical distributions in the image plane and in the near field or object plane.

With the preceeding considerations, it remains to determine the form of $A_o(x,t)$. We begin with the simple example of a sinusoidal, progressive acoustic wave. Assume that the cavity is optically isotropic in the absence of acoustic waves, and, to simplify notation, that the incident light is polarized along one of the axes of the index ellipse (See FIG. 5). Since the change in refractive index is, to a good approximation, linear in the local strain [see equation (1.58)], the refractive index will have the form:

$$n(x,t) = n_o + \Delta n \sin(Kx - \Omega t) \qquad (o<z<L) \qquad (1.61)$$

where n_o is the unperturbed refractive index, K and Ω are the wavenumber and frequency of the acoustic wave.

Since the refractive index has slow variation compared with optical frequencies, the wave equation governing propagation of the optical signal A in the acoustic cavity may be written (Raman and Nath 1936b) :

$$\nabla^2 A = \frac{n(x,t)^2}{c^2} \frac{\partial^2 A}{\partial t^2} \tag{1.62}$$

where c is the vacuum velocity of light. In the absence of acoustic fields, A will propogate in the region o<z<L in the form

$$a_o(x,z,t) = e^{i[n_o k (z \cos \phi + x \sin \phi) - \omega t]} \tag{1.63}$$

k,ω are the optical wavenumber and frequency and ϕ is the angle made by incident light with the z axis (see FIG. 6).

The modulation of the optical wave produced by the presence of acoustic strains will be slowly varying compared with the spatial and temporal dependence of (1.63). Thus in the presence of the acoustic wave the optical waveform may be described by:

$$A(x,z,t) = a_o(x,z,t)\, \psi(x,z,t) \tag{1.64}$$

The envelope function $\psi(x,z,t)$ will be periodic in space and time with the acoustic wave, and hence may be written as a Fourier series:

$$\psi(x,z,t) = \sum_{n=-\infty}^{\infty} \psi_n(z)\, e^{in(Kx - \Omega t)} \tag{1.65}$$

subject to the boundary conditions

$$\left.\begin{aligned} \psi_o &= 1 \\ \psi_n &= 0 \qquad n \neq 0 \end{aligned}\right\} \text{ at } z=0 \tag{1.66}$$

The near field amplitude $A_o(x,t)$ is given by setting $z=L$ in equations (1.63) to (1.65). Substituting the resulting expressions into (1.60) we obtain for the focal plane optical signal:

$$A_f(x',t) = e^{i(n_o kL\cos\phi - \omega t)} \sum_{n=-\infty}^{\infty} \psi_n(L) e^{-in\Omega t} \int_{-\infty}^{\infty} e^{-i(k'-k\sin\phi-nK)x}\, dx \tag{1.67}$$

The integral in equation (1.67) is non-zero only if

$$k' - k\sin\phi - nK = 0 \tag{1.68}$$

Light will appear in the focal plane only at those points which satisfy equation (1.68). Hence the index n labels the diffraction orders in the

focal plane. The optical intensity in the n^{th} diffraction order is given by equation (1.67) as

$$I_n = |\psi_n(L)|^2 \tag{1.69}$$

Also, the angular frequency in the n^{th} order may be inferred from (1.67) :

$$\omega_n = \omega + n\Omega \tag{1.70}$$

Equations (1.63) to (1.65) may be substituted into (1.62). If terms in $(\Delta n)^2$ and $\psi''(z)$ are neglected, coefficients of exp $i[n(Kx-\Omega t)]$ may be equated to obtain:

$$\frac{d\psi_n(z)}{dz} + \frac{v}{2L}[\psi_{n-1}(z)-\psi_{n+1}(z)] = \frac{inQ}{2L}(n-2\gamma)\psi_n(z) \tag{1.71}$$

where:

$$v = \Delta nkL \tag{1.72}$$

$$Q = \frac{K^2L}{n_o k} \tag{1.73}$$

$$\gamma = \frac{-n_o k \sin\phi}{K} \tag{1.74}$$

as indicated by equation (1.69), the optical amplitude in the n^{th}

diffraction order in the focal plane is proportional to $\psi_n(L)$. The difference - differential equation (1.71) was derived in the special case $\gamma = 0$ (normal light incidence) by Raman and Nath (1936b), and in the more general case by Klein and Cook (1967).

In equation (1.71) adjacent optical modes are coupled by the parameter v. Interaction and transfer of energy between these modes will only take place if they maintain a constant phase relationship, i.e. maintain spatial synchronization. The degree of synchronization is determined by the coefficient, to be designated β_n, on the R.H.S. of equation (1.71) :

$$\beta_n = \frac{inQ}{2L}(n-2\gamma) \tag{1.75}$$

This may be considered as a relative phase factor, and only those optical modes having the same, or nearly the same, value of this coefficient may be considered as being spatially coherent or synchronized, and hence able to exchange optical energy.

Since $\beta_o = 0$, an appreciable amount of optical energy can be coupled from the zeroth into the first order only if one or both of the coefficients $\beta_{\pm 1}$ are very small. This condition can be satisfied in two regimes : (i) $Q \ll 1$, $\gamma \simeq 0$; (ii) $Q \gg 1$, $\gamma = \pm\frac{1}{2}$. (i) and (ii) are the two limiting situations for which analytic solutions to (1.71) are practical, and each case will be discussed separately.

Raman - Nath Limit: $Q \ll 1$

For $Q = 0$ and with boundary conditions (1.66) the solution to (1.71) may be shown to be (Raman and Nath 1936 b) :

$$\psi_n(z) = J_n(\Delta n k z) \tag{1.76}$$

where J_n is a Bessel function of order n. For sufficiently small nonzero values of Q, Bessel functions form good approximate solutions of (1.71). The regime of validity of this approximation is named for the two workers who first provided a theoretical basis for this type of diffraction (see Raman and Nath 1935 a,b and 1936 a,b).

For this situation energy is symmetrically coupled from the zero order into both first order modes ($n=\pm 1$). In addition, for sufficiently large values of the coupling parameter v, energy is coupled from the first order to the second order, the second order to the third, etc. From a comparison of equations (1.73) and (1.74) it is apparent that for Q small γ can be very large, even for small values of the incident angle ϕ. Thus we optimize the condition $\beta_n \simeq 0$ $(n \neq 0)$ by choosing $\phi = 0 \Rightarrow \gamma = 0$ (normal light incidence). The optical intensity in the n^{th} diffraction order is then given from equations (1.69), (1.72) and (1.76) :

$$I_n = J_n^2(v) \tag{1.77}$$

and, setting $\phi = 0$ in equation (1.68), we obtain for the diffraction

angle θ :

$$\sin \theta = \frac{n\lambda}{\Lambda} \tag{1.78}$$

where λ is the optical wavelength in vacuo and Λ is the acoustic wavelength.

In the Raman - Nath regime the acoustic wave only modulates the phase of the optical signal. The parameter v, referred to as the Raman - Nath parameter in this situation, is equal to the maximum acoustically induced phase shift suffered by the light in traversing the acoustic cavity (see eqn. 1.72).

A practical upper limit of the Raman - Nath regime is given by (Klein and Cook 1967) :

$$Q \lesssim 0.5 \tag{1.79}$$

For large values of v (ie. large values of acoustic strain) condition (1.79) may not be sufficient to ensure true R-N diffraction. For this reason the supplementary condition (Extermann and Wannier 1936) :

$$Qv < 2 \tag{1.80}$$

is sometimes quoted. For our experimental situation, however, $v \ll 1$ and the nature of the diffraction is adequately described by the magnitude of the parameter Q.

Bragg Limit : Q>>1

For this situation, the condition $\beta_n = 0$ $(n \neq 0)$ can be satisfied only for n = 1 or n = -1. Thus for $\gamma = \frac{1}{2}(-\frac{1}{2})$ light is diffracted only into order +1(-1). Other combinations of n and γ are not allowed for a simple sinusoidal acoustic wave. For $n = \pm 2$, $\gamma = \pm 1$, for example, no light may be transferred from the zero order since only adjacent orders are directly coupled by equation (1.71). For $\gamma = \pm\frac{1}{2}$ equation (1.74) may be written in the more transparent form:

$$\frac{\lambda}{n_o} = \pm 2\Lambda \sin \phi \tag{1.81}$$

Thus $\gamma = \pm\frac{1}{2}$ implies that ϕ satisfies the Bragg condition for specular optical reflection from the acoustic wave fronts. A practical lower limit for the Bragg regime is given by (Willard, 1949) :

$$Q \gtrsim 4\pi \tag{1.82}$$

For values of Q intermediate to the Raman - Nath and Bragg regimes, analytic solutions to (1.71) are not practical. The gap between the two limiting cases has been spanned by Klein and Cook (1967), using numerical techniques. Some of their results are reproduced in FIG. 7. The curves illustrated give the percentage of optical intensity in the zero and two first order diffraction spots at normal incidence (γ=0), for different values of the parameter Q. By summing the intensities in the zeroth and first order in FIG. 7, it may be seen that second and higher orders are depleted as Q increases, until at Q = 4 almost no

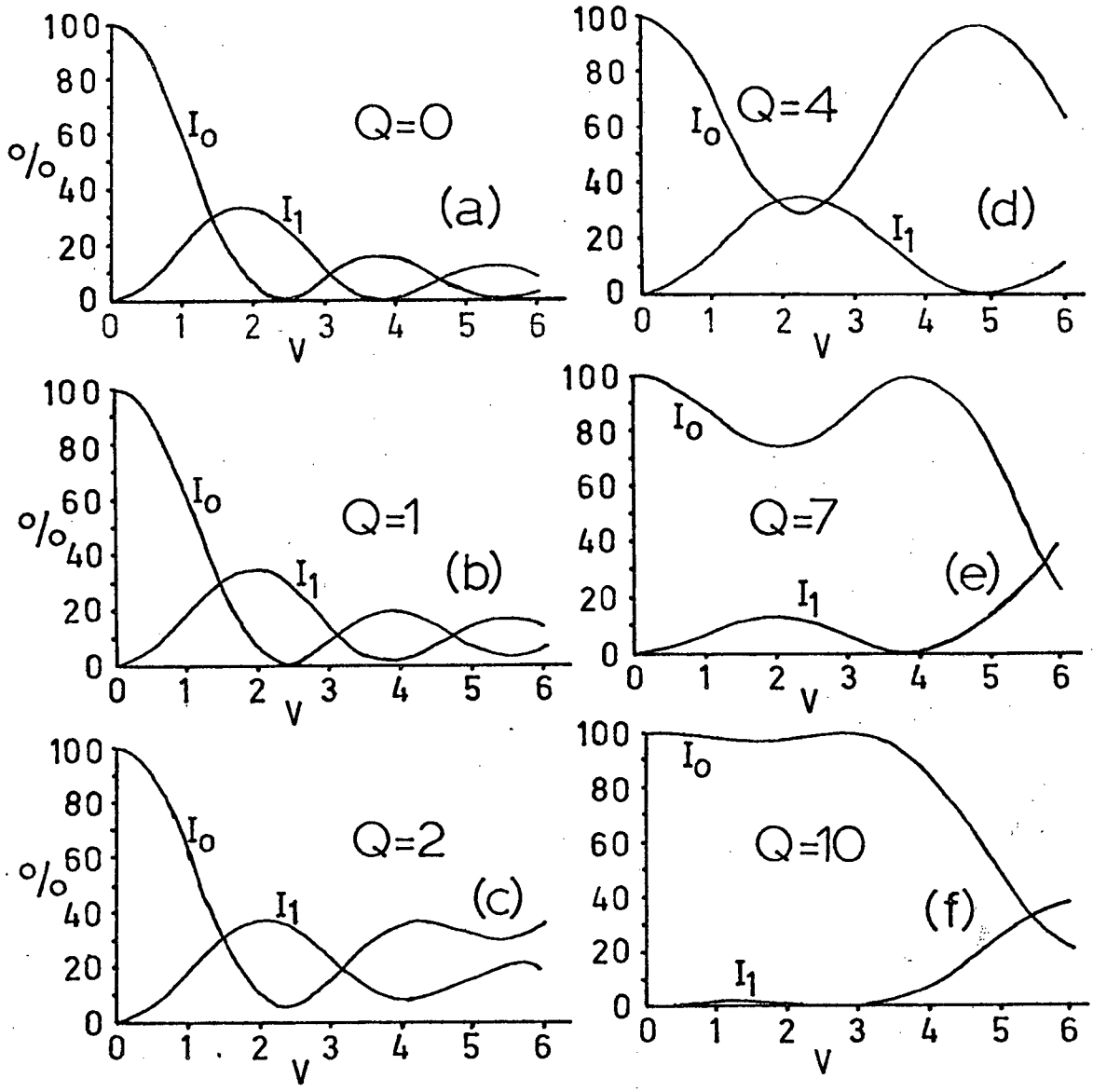

FIG 7. Percentage of optical intensity in the zero and two first order diffraction spots at normal incidence ($\gamma = 0$), for various values of the parameter Q. (after Klein and Cook 1967). v is defined in equation (1.72).

light appears beyond the first order. In the range Q = 4 to Q = 7 the amount of light in the two first orders decreases considerably, and when Q = 10 there is almost no diffraction at normal incidence for small values of v (small acoustic strains).

The values of Q encountered for mode-locked phonon maser operation can span the entire gamut from Raman - Nath to Bragg diffraction. However, the experimental results to be described in section 1.4 lie in the range $v<<1$, for which second order diffraction is completely negligible, and $Q \lesssim 5$. For these conditions, it is apparent from FIG. 7 (a) - (d) that first order diffraction does not change significantly from the Raman - Nath case. For this reason it will be assumed in all subsequent discussion that the effect of acoustic fields on a light wave may be described by an optical phase transformation, as in the Raman - Nath regime.

1.3.3 Interpretation of the Optical Signal - The Mode-Locked Phonon Maser

In applying the results of the last section to a study of the strain profile in a mode-locked phonon maser, the basic configuration illustrated in FIG. 6 will be retained. The light is now assumed to propogate in the z direction so as to be normally incident on the acoustic waveform. As discussed in section 1.3.2, this is the optimum configuration for Raman - Nath diffraction.

Following the discussion at the end of section 1.3.2, we assume that the only effect of the acoustic strain profile is to produce variations in the optical phase, via acoustically induced modulations of

the refractive index. Since the relationship between the local strain and refractive index variation is linear [eg. see equation (1.58)], the phase variation profile directly yields the acoustic strain profile. If the phase variation of the acoustic cavity is described by $\Phi(x,t)$, the near field light amplitude is given by [c.f. equations (1.63) and (1.64)]

$$A_o(x,t) = e^{i(n_o kL - \omega t)} e^{i\Phi(x,t)} \tag{1.83}$$

For mode-locked operation, the acoustic waveform is assumed to be a standing wave pattern consisting of a phase-locked harmonic series of sinusoidal waves. Using the results of Appendix A, the phase function in equation (1.83) may be written in the form:

$$\Phi(x,t) = \sum_{n=1}^{N} v_n \left\{ \sin[n(Kx-\Omega t) + \delta_n] + \sin[nK(x-2d) + n\Omega t - \delta_n] \right\} \tag{1.84}$$

where d is the thickness of the acoustic cavity, N is the number of active or participating acoustic modes and Ω, K are the angular frequency and wave number of the fundamental component. The phase amplitudes v_n are the Raman - Nath parameters discussed in section 1.3.2, and are proportional to the corresponding strain amplitudes. The set of phases δ_n will determine the exact shape of the phase variation, and hence the strain, profile. Equation (1.84) may also be written in the form:

$$\Phi(x,t) = 2\sum_{n=1}^{N} v_n \sin[nK(x-d)]\cos(nKd - n\Omega t + \delta_n) \qquad (1.85)$$

Since the acoustic cavity alters only the phase of the incident light, the strain field is not directly visible in the image plane of the focussing lens (refer to FIG 6). This problem may be overcome by means of focal plane spatial filtering techniques. If certain diffraction orders are physically removed (i.e. spatially filtered) in the focal plane, the effect is to present a modified Fourier transform of the near field signal to the image plane [refer to discussion following equation (1.60)]. Thus the image viewed will correspond to a pseudo-object whose Fourier transform is given by the modified focal plane distribution passed by the spatial filter.

By removing the zero order or undiffracted beam in the focal plane, for example, the dark field image is obtained (Born and Wolf 1959). In this situation, phase variations in the object plane produce intensity variations in the image plane. The dark field distribution will be derived in two ways. First, we begin by substituting the phase function for a mode-locked waveform, equation (1.85), into equation (1.83):

$$A_o(x,t) = e^{i\zeta} \exp i\left[\sum_{n=1}^{N} 2v_n \sin[nK(x-d)]\cos(nKd - n\Omega t + \delta_n) \right] \qquad (1.86)$$

where $\zeta = (n_o kL - \omega t)$. Making use of the Bessel function relationship (Abramowitz and Segun 1968):

$$e^{iz\sin\theta} = \sum_{m=-\infty}^{\infty} J_m(z)e^{im\theta} \tag{1.87}$$

equation (1.86) may be written:

$$A_o(x,t) = e^{i\zeta} \prod_{n=1}^{N} \sum_{p_n=-\infty}^{\infty} J_{p_n}[2v_n\cos(nKd-n\Omega t+\delta_n)]e^{ip_n nK(x-d)} \tag{1.88}$$

$$= e^{i\zeta} \sum_{p_1=-\infty}^{\infty} \cdots\cdots \sum_{p_N=-\infty}^{\infty} J_{p_1}(V_1)\cdots\cdots J_{p_N}(V_N)\exp i\left(\sum_{n=1}^{N} np_nK(x-d) \right) \tag{1.89}$$

where $V_n = 2v_n\cos(nKd-n\Omega t+\delta_n)$. (1.90)

A useful analogy may now be made with the case of a simple sinusoidal acoustic wave discussed in section 1.3.2. When equation (1.65) was substituted into equation (1.60) to obtain the focal plane optical distribution, it was found that the coefficient of the spatial factor Kx in the exponential term of (1.65), n in this case, labelled the diffraction orders in the focal plane. By analogy, the diffraction order for equation (1.89) may be inferred :

$$\text{diffraction order} = \sum_{n=1}^{n} np_n \tag{1.91}$$

This greatly simplifies the mathematics of spatial filtering. It is not necessary to Fourier transform the near field to find the focal plane distribution, perform spatial filtering, and then inverse Fourier

transform to obtain the image plane signal. Instead, we may use equation (1.90) to identify those components of $A_o(x,t)$ that correspond to the focal plane orders to be removed (passed) by the spatial filter, and hence obtain the modified image directly.

It is intuitively clear, from the cumbersome form of equation (1.89), that an analytic expression for the dark field distribution is not practical in the most general case. However, we are concerned with small values of the Raman - Nath parameters v_n. For the experiments to be discussed, $v_n \lesssim 10^{-2}$ radians. It is therefore necessary to consider only effects that are first order in v_n. In addition, we may use the asymptotic form for Bessel functions of small argument (Abramowitz and Segun 1968):

$$J_m(z) \xrightarrow[z \text{ small}]{} \frac{(\frac{1}{2}z)^m}{m!} \qquad (m \geq 0) \tag{1.92}$$

Equation (1.92) may be used for negative values of m by first using the relationship (Abramowitz and Segun 1968):

$$J_{-m}(z) = (-1)^m J_m(z) \tag{1.93}$$

In first order, the parameters p_n in equation (1.89) may only take the values 0, $\pm$ 1. Furthermore, if one of these parameters takes the value +1 or -1, all others must be zero. Let

$$p_n = +1 \quad \rightarrow \quad p_i = 0 \quad \text{for } i \neq n \tag{1.94}$$

The corresponding contribution from equation (1.89) is [using equation (1.92)]:

$$A_n = e^{i\zeta} \frac{V_n}{2} e^{inK(x-d)} \tag{1.95}$$

From equations (1.91) and (1.94) it may be seen that (1.95) constitutes the first order contribution to diffraction order +n. Similarly, the first order contribution to diffraction order -n is given by setting $p_n=-1$ in equation (1.94) and using (1.92) and (1.93) to obtain:

$$A_{-n} = -e^{i\zeta} \frac{V_n}{2} e^{-inK(x-d)} \tag{1.96}$$

The zero order amplitude must be treated separately and is given by setting $p_i = 0$ for all i. Using equation (1.92) we obtain:

$$A_o = e^{i\zeta} \tag{1.97}$$

Hence the intensity in the zero order, $|A_o|^2$, is equal to one. This indicates that, to first order in the Raman - Nath parameters, the zero order beam is unaffected by the diffraction.

Adding equations (1.95) and (1.96) we obtain:

$$ie^{i\zeta}V_n \sin[nK(x-d)] \tag{1.98}$$

It is apparent from equations (1.95) and (1.96) that the index n, as it is used in (1.98), labels symmetric diffraction orders in the focal

plane. Hence the dark field amplitude is found by summing (1.98) over all values of n except n = 0 :

$$A_{DF} = ie^{i\zeta} \sum_{n=1}^{N} V_n \sin[nK(x-d)] \tag{1.99}$$

or, using equations (1.85) and (1.90):

$$A_{DF} = ie^{i\zeta}\, \Phi(x,t) \tag{1.100}$$

Thus the first order dark field amplitude is proportional to the phase variation produced by the acoustic cavity. The corresponding optical intensity is given by:

$$I_{DF} = \Phi^2(x,t) \tag{1.101}$$

It is, in fact, the intensity distribution, equation (1.101), that may be detected experimentally.

The second method of deriving the dark field distribution is much simpler, but gives little insight into the mechanism of spatial filtering. Since we have assumed small phase variations, the exponential in equation (1.83) may be expanded to yield:

$$A_o(x,t) \simeq e^{i\zeta} [\, 1 + i\Phi(x,t) \,] \tag{1.102}$$

The dark field amplitude corresponds to removing the factor of 1 in

equation (1.102), to immediately yield equation (1.100). While this method of derivation is much simpler, it should be emphasized that it is useful only for effects that are first order in v_n. For higher order effects the factor of 1 in equation (1.102) can no longer be correctly identified as the amplitude of the zero order diffraction spot, and the image plane distribution must be derived using the first method.

The dark field intensity distribution is obtained by substituting equation (1.84) or equation (1.85), into equation (1.101). The resulting expression is very messy, having terms with all the possible combinations of spatial and frequency dependence produced by the nonlinear operation of squaring. If, however, we extract only the term which has no time dependence, we obtain the relatively simple expression (Smeaton, Hughes, Vrba and Haering 1976):

$$I_o = \sum_{n=1}^{N} v_n^2[1 - \cos 2nK(x-d)] \qquad (1.103)$$

This D.C. term is straightforward in the sense that it contains none of the phases δ_n [see equation (1.84) or (1.85)]. Thus its form depends only on the constituent amplitudes and not on the exact shape of the acoustic waveform.

Equation (1.103) is plotted in FIG 8. The relative values of the amplitudes v_n were inferred from experimental diffraction intensities, obtained for the first 13 active modes of a mode-locked phonon maser. Thus N = 13 in FIG 8. The width PW of the dark fringes is inversely proportional to the number of participating modes N, and provides an

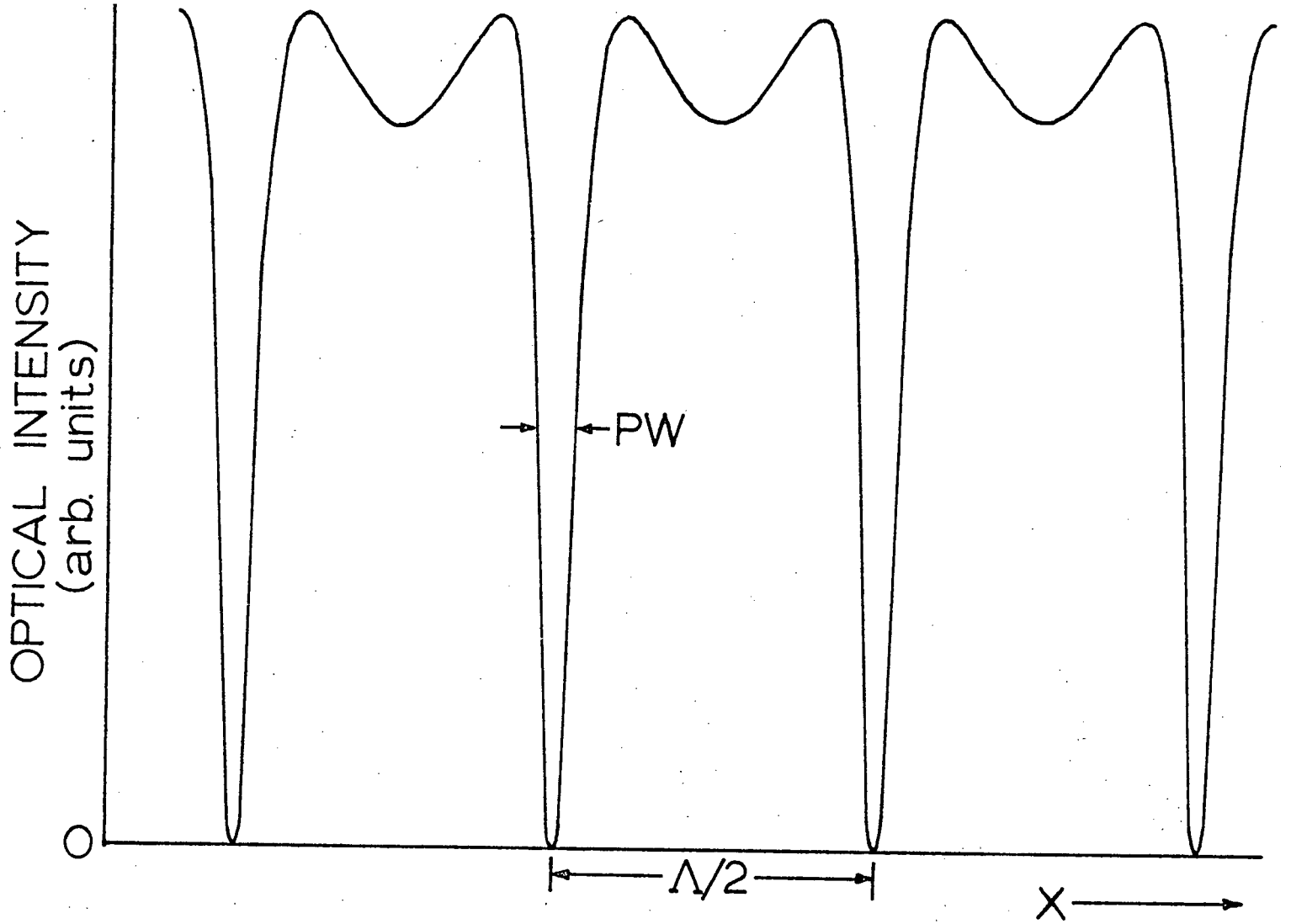

FIG 8. Profile of the dark field term, equation (1.103), plotted using the amplitudes of the first 13 active acoustic modes for mode-locked operation of DC1 (refer to section 1.4.2).

estimate of the mode-locked pulse width (refer to section 1.2). As is indicated, the basic periodicity is $\Lambda/2$, where Λ is the wavelength of the acoustic fundamental.

To obtain I_o in equation (1.103), a combination of spatial and temporal filtering was employed. That is, we first modified the optical distibution in the focal plane, and then selected only one frequency component, the D.C. component in this case, to be examined in the image plane. By extending this general technique, information about the phases δ_n, absent in equation (1.103), may be recovered. This is of considerable interest since these phases determine the exact shape and amplitude of the acoustic strain profile.

Consider, for example, that spatial orders n, n+1, and n+2 (i.e. the n^{th} pair of diffraction spots symmetric to the zero order, the $(n+1)^{th}$ pair and so on) are combined, and the intensity variation of the temporal component corresponding to the acoustic fundamental frequency Ω is scanned in the image plane. The total image plane intensity distribution is given by [refer to equation (1.99)]:

$$I_{n,n+1,n+2} = \left\{ \sum_{m=n}^{n+2} v_m \Big[\sin[m(Kx - \Omega t) + \delta_m] + \sin[mK(x-2d) + m\Omega t - \delta_m] \Big] \right\}^2 \qquad (1.104)$$

Extracting only those terms from (1.104) which have frequency dependence Ω, we obtain:

$$T^{\Omega}_{n,n+1,n+2} = 2\left\{ a_n\cos(Kd+\delta_{n+1}-\delta_n) + b_n\cos(Kd+\delta_{n+2}-\delta_{n+1}) \right\}\cos\Omega t$$

$$+ 2\left\{ a_n\sin(Kd+\delta_{n+1}-\delta_n) + b_n\sin(Kd+\delta_{n+2}-\delta_{n+1}) \right\}\sin\Omega t \qquad (1.105)$$

where

$$a_n = 2v_nv_{n+1}\sin[nK(x-d)]\sin[(n+1)K(x-d)]$$

$$b_n = 2v_{n+1}v_{n+2}\sin[(n+1)K(x-d)]\sin[(n+2)K(x-d)] \qquad (1.106)$$

We write equation (1.105) in the form

$$T^{\Omega}_{n,n+1,n+2} = a\cos\Omega t + b\sin\Omega t \qquad (1.107)$$

where a,b are defined implicitly by comparison of equations (1.105) and (1.107). Introducing notation

$$\left.\begin{aligned} a &= C\sin\eta \\ b &= C\cos\eta \end{aligned}\right\} \Rightarrow \left\{\begin{aligned} C &= (a^2+b^2)^{\frac{1}{2}} \\ \tan\eta &= a/b \end{aligned}\right. \qquad (1.108)$$

equation (1.107) may be written:

$$T^{\Omega}_{n,n+1,n+2} = C\sin(\Omega t+\eta) \qquad (1.109)$$

The Fourier transform of (1.109) has the following simple form in the

frequency (Ω') domain:

$$\tau^{\Omega}_{n,n+1,n+2} = \frac{-iC}{2}\left[e^{in\eta\delta(\Omega'-\Omega)} - e^{-in\eta\delta(\Omega'+\Omega)} \right] \qquad (1.110)$$

In practice, the magnitude of the component of (1.110) at $\Omega'=\Omega$ is monitored. Thus the detected signal becomes:

$$I^{\Omega}_{n,n+1,n+2} = \frac{C}{2} = \frac{(a^2+b^2)^{\frac{1}{2}}}{2} \qquad (1.111)$$

Using the definitions of a and b [equations(1.105) and (1.107)] we obtain (Smeaton and Haering 1976a):

$$I^{\Omega}_{n,n+1,n+2} = (a_n + b_n + 2a_nb_n\cos\Theta_n)^{\frac{1}{2}} \qquad (1.112)$$

where a_n, b_n are defined by equation (1.106) and

$$\Theta_n = \delta_n - 2\delta_{n+1} + \delta_{n+2} \qquad (1.113)$$

The observed image plane profile should therefore depend on the magnitude of Θ_n , a linear combination of the individual phases of the three combined orders. The behavior of equation (1.112) as a function of Θ_n is illustrated in FIG 9, for n=4. The relative values of v_n were calculated from experimental diffraction intensities obtained for

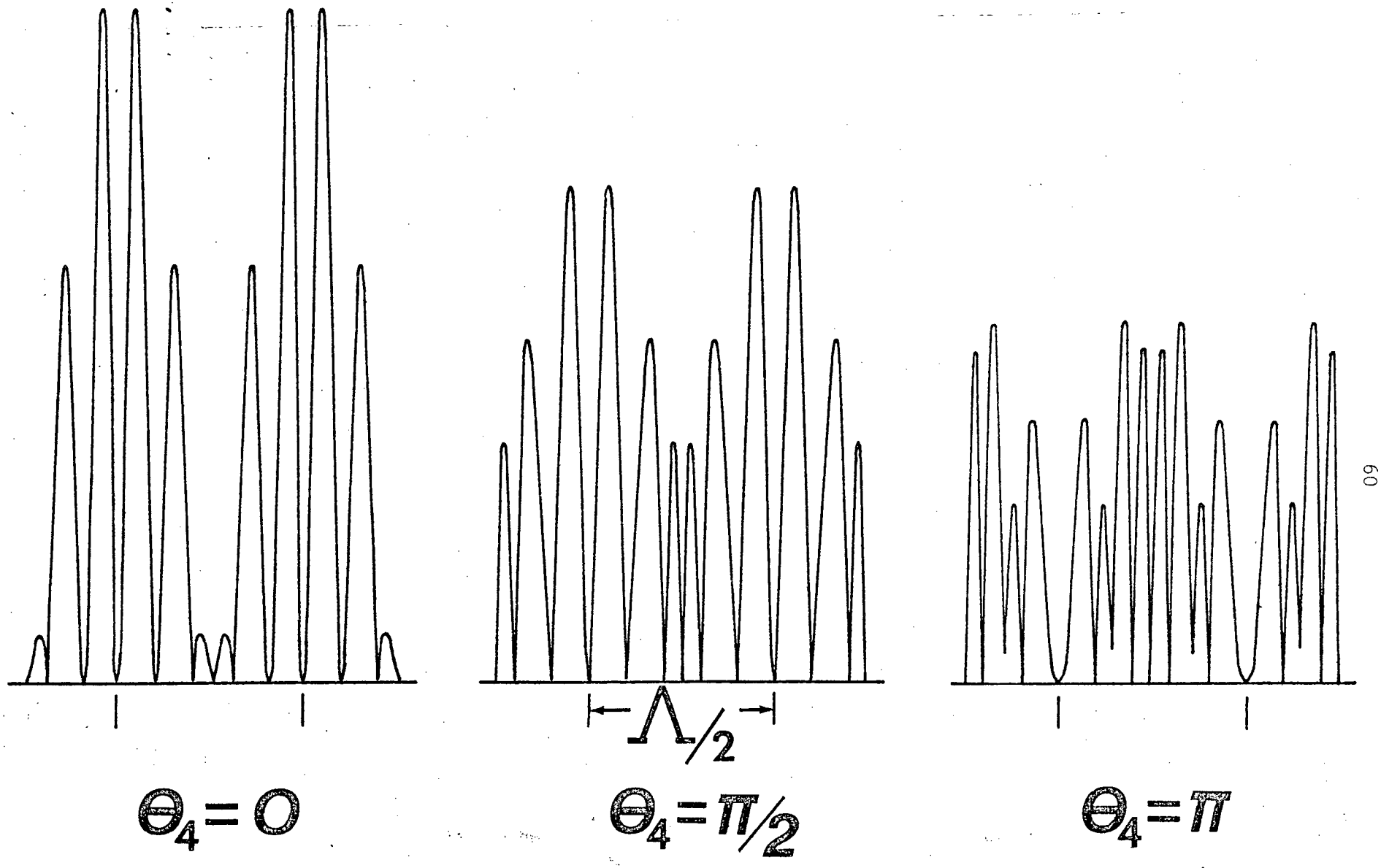

FIG 9. Theoretical image plane intensity profile of the Ω component for combined spatial orders 4,5,6, for different values of $\Theta_4 = \delta_4 - 2\delta_5 + \delta_6$.

mode-locked operation. The sensitivity of the theoretical profiles in FIG 9 to variations in θ_4 indicates that it is feasible to recover phase information by optical means. The intensity profiles for other combinations of spatial and temporal filtering may be derived in a manner similar to equation (1.112).

1.4 Experimental Results

The CdS phonon maser crystals used in these experiments were oriented so that the b-axis was perpendicular to the polished cavity surfaces. For this orientation the active acoustic modes consist of shear waves whose K-vectors lie along the b-axis. For the optical measurements, the active CdS crystals were coupled to passive fused quartz cavities by means of a high quality bond (described in Appendix C). Since the two materials have nearly the same acoustic impedance for the chosen CdS orientation, the double cavity modes were nearly harmonic (Hughes and Haering 1976). The passive cavity provided a convenient means of examining the acoustic field of the phonon maser, since high power laser light could be passed through it. Such a high intensity probe could not be used in the active cavity since the large photo-currents produced would disrupt or prevent oscillation.

The A.C. acousto-electric current signal (refer to section 1.1) from the active crystal could be displayed either in the frequency regime, by means of a spectrum analyzer, or in the time regime by means of a sampling oscilloscope. An example of both displays is shown in FIG 10, for mode-locked operation of phonon maser 24.01.02.04. The well defined waveform exhibited in the time domain in FIG 10(b), indicates that the harmonically related modes in FIG 10(a) are phase-locked. The D.C. I-V characteristics of the same phonon maser are displayed in FIG 11(a) for two different conductivities. The oblique arrows indicate the threshold for acoustic oscillation. Above threshold,

(a)

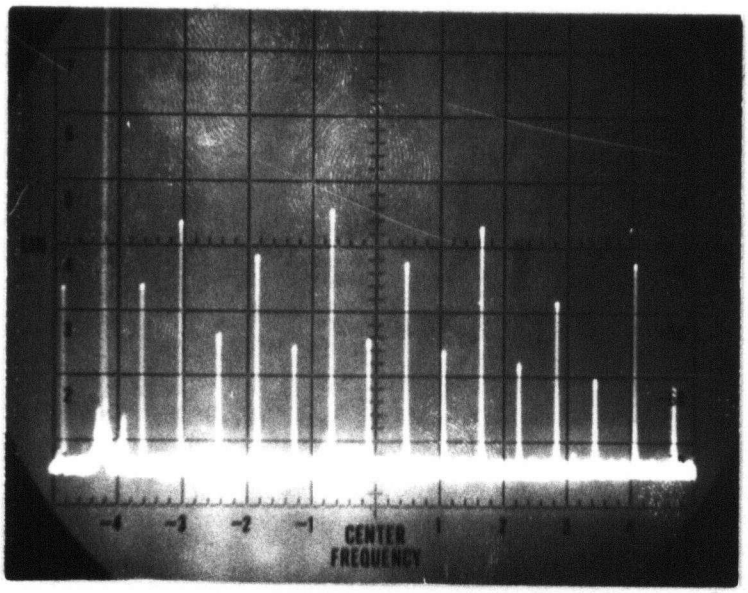

FREQUENCY DOMAIN, 20MHz/div.

(b)

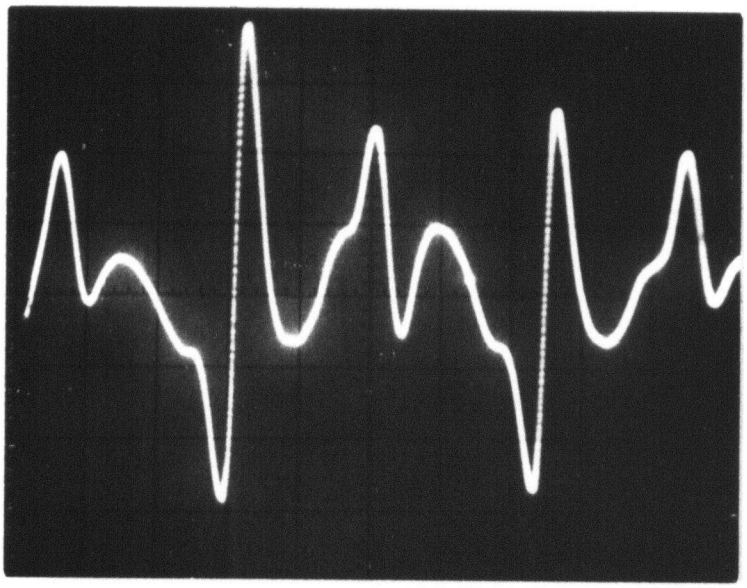

TIME DOMAIN, 10 nanosec./div.

FIG 10. Display of the acousto-electric current signal for $b_{\perp}$ phonon maser 24.01.02.04 (part of composite cavity DC1). (a) frequency domain, (b) time domain. Operating conditions: applied D.C. electric field = 0.98 KV/cm, D.C. current density = 11.1 mA/cm^2.

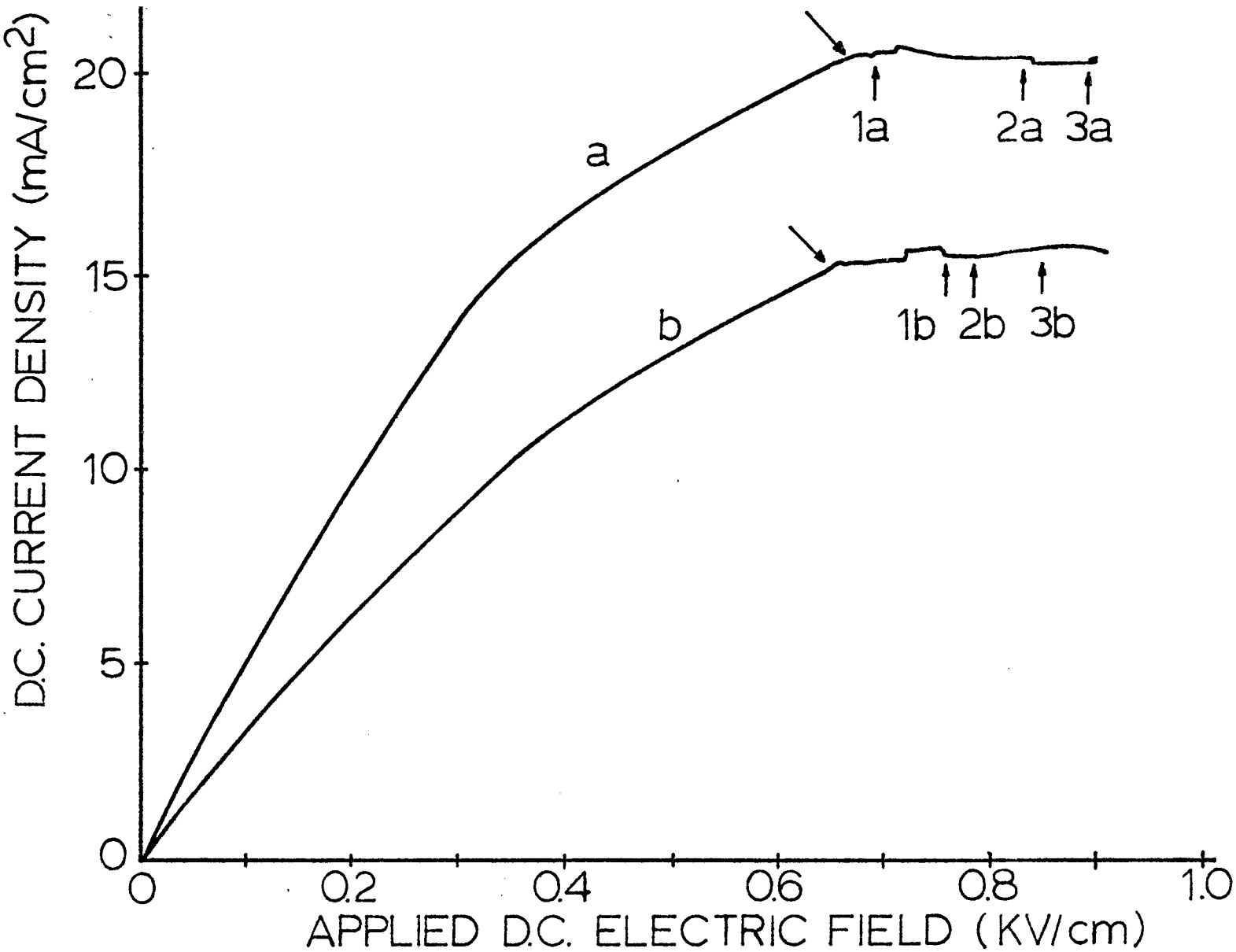

FIG 11(a). D.C. current density vs. applied D.C. electric field for b⊥ phonon maser 24.01.02.04 (part of composite cavity DC1) for two different conductivities a, b. [See text and FIG 11(b)].

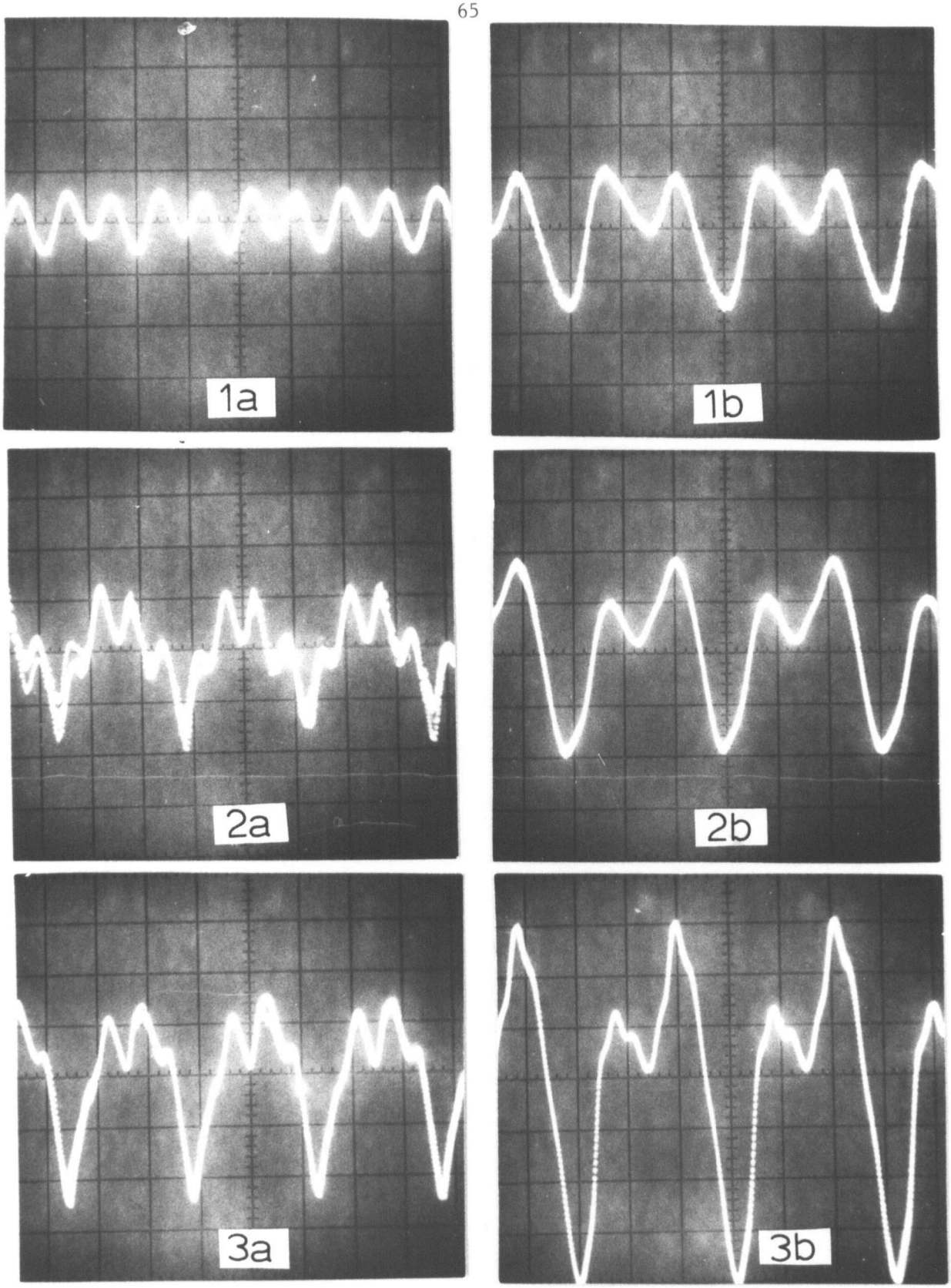

FIG 11(b). Time display of the acousto-electric current for the points indicated in FIG 11(a). Horizontal scale: 10 nanoseconds/div.

saturation of the D.C. current may be observed (refer to the discussion at the end of section 1.2). The small discontinuous steps in this region occur when the phonon maser makes sudden adjustments in its mode structure. To show the development of current spiking, the time display of the acousto-electric current was recorded at the points indicated in FIG 11(a), and may be seen in FIG 11(b). It was the observation of spiking and self-locking modes in the acousto-electric current, as evidenced in FIG 10 and 11(b), that first led to speculation that the acoustic output was also mode-locked, and hence should consist of narrow, high amplitude strain pulses (Maines and Paige 1970).

1.4.1 Experimental Apparatus and Techniques

The configuration for the optical experiments is shown schematically in FIG 12. The light source was an argon-ion laser operated at 5145 Å, with a typical output power of about 1 Watt. At this high power level, even stray scattered laser light was found to greatly disrupt oscillation in the active cavity, and careful light shielding was necessary. The incident light beams were carefully prepared to provide good collimation, and beam diameters were typically 4 - 5 mm. A mounted double cavity is shown in FIG 13(a). The goniometer mount allowed convenient orientation of the acoustic cavity for maximum diffraction efficiency.

The focussing lens was required to subtend a sufficiently large diffraction angle at the acoustic cavity that loss of optical information was negligible, and yet to provide a focal plane diffraction

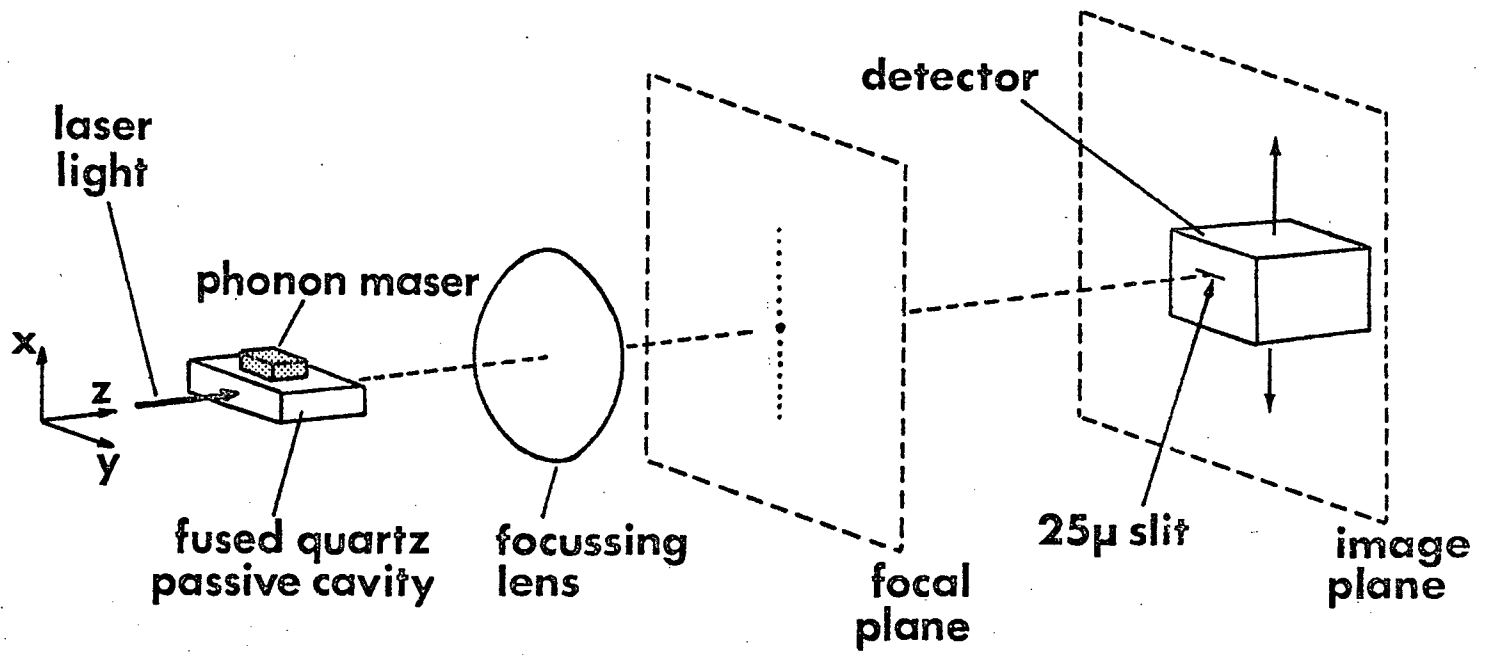

FIG 12. Experimental configuration for the optical measurements.

pattern of sufficient size to allow spatial filtering. An f/2.5, 15 cm focal length lens was found to satisfy these criteria. All optical components were maintained clean and vibration free to minimize optical noise in the image plane.

Fused quartz may be considered optically and acoustically isotropic, and the results of section 1.3.1 may be directly applied to illustrate a useful polarization property of shear acoustic waves. Consider, in FIG 5, that incident light is polarized along the x_2 axis, i.e. perpendicular to the direction of acoustic propagation. If we let $\vec{i}$, $\vec{j}$ be unit vectors along the x_1', x_2' axes in FIG 5, incident light of amplitude A may be represented by:

$$\vec{A} = \frac{A}{\sqrt{2}} (\vec{i} + \vec{j}) . \tag{1.114}$$

Light diffracted into the m^{th} order has components along the axes of the index ellipse given by (refer to Vrba and Haering 1974):

$$A_{I,m} = \frac{A}{\sqrt{2}} A_m(v_{I,m}) \exp(iv_{I,m})$$

$$A_{II,m} = \frac{A}{\sqrt{2}} A_m(v_{II,m}) \exp(iv_{II,m}) \tag{1.115}$$

where $v_{I,m}$ and $v_{II,m}$ are the Raman - Nath parameters corresponding to the x_1', x_2' axes, respectively, in FIG 5. A_m is the appropriate diffraction amplitude per unit incident amplitude, and is given by equations (1.90)

and (1.95). The exponential factors in equation (1.115) represent the optical phase variation produced by the acoustic cavity. The two components in equation (1.115) add coherently in vector form (Vrba and Haering 1974). The total amplitude may then be written:

$$\vec{A}_m = \frac{A}{\sqrt{2}} \left[A_m(v_{I,m}) \exp(iv_{I,m}) \vec{i} + A_m(v_{II,m}) \exp(iv_{II,m}) \vec{j} \right] \quad (1.116)$$

Equation (1.116) yields elliptically polarized light. The amount of ellipticity is extremely small, however, since the Raman - Nath parameters $v_{I,m}$, $v_{II,m} << 1$. Thus, to a very good approximation, the exponential factors in (1.116) may be replaced by 1. In addition, $v_{I,m} = -v_{II,m}$ from equations (1.58) and (1.72). Thus from equations (1.90) and (1.95) we see that

$$A_m(v_{I,m}) = -A_m(v_{II,m}) \qquad (|m| > 0) \qquad (1.117)$$

and equation (1.116) becomes:

$$\vec{A}_m = \frac{A}{\sqrt{2}} A_m(v_{I,m})(\vec{i} - \vec{j}) \qquad (|m| > 0) \qquad (1.118)$$

Thus the polarization of the diffracted light is rotated by 90° with respect to the incident light. This polarization flip also occurs if the incident light is polarized along x_1 in FIG 5, i.e. parallel to the direction of acoustic propagation. In either case, the polarization of

the zero order light [refer to equation (1.97)] is unaffected. Thus an exit polarizer may be used to greatly attenuate the strong background due to undiffracted light, while leaving diffracted light largely unaffected.

The exit polarizer used was an air-spaced Glan-Thompson prism, designed for high intensity laser light. The useful aperture of the polarizing prism was large, about 2.5 cm, to avoid truncation of the diffracted light, and dielectric coatings on the entrance and exit faces optimized transmission at 5145 Å. The extinction ratio was about 3×10^4.

The focal plane diffraction pattern consisted of a vertical row of spots symmetrically arranged about the zero order or undiffracted beam. At higher operating levels, 60 - 70 diffraction spots could be distinguished by eye. In the first order approximation outlined in section 1.3.3, each acoustic mode only produced one symmetric pair of spots. Thus the first two spots symmetric to the zero order were produced by the acoustic fundamental, the next pair by the first harmonic, and so on. Hence the various acoustic modes were, to second order in the Raman - Nath parameters, optically decoupled in the focal plane. The time-averaged intensity of the n^{th} order diffraction spot is given by equations (1.95) and (1.90) as $v_n^2/2$ (in practice, we are not dealing with unit amplitude incident light, and it was necessary to divide by the zero order intensity to obtain $v_n^2/2$). The corresponding strain amplitude could then be obtained using equations (1.58) and (1.72).

The form of the focal plane diffraction pattern is illustrated in FIG 13(b). The weak spots laterally displaced from the main vertical array were produced by diffraction of the acoustic waves, i.e. the active cavity effectively behaved as an aperature for acoustic waves radiating into the buffer (c.f. Fraunhofer diffraction by a single slit). This secondary feature may be ignored since it had negligible effect on the optical experiments performed.

The apparatus used for focal plane spatial filtering is shown in FIG 13(c). The V-slit was designed for processing symmetric diffraction orders, and its width could be accurately adjusted by means of a micrometer. X-Y movement was controlled by adjusting screws, to provide accurate positioning in the focal plane, and the diffraction pattern was viewed through a low power microscope to ensure precise optical "surgery".

A photomultiplier coupled to a horizontal slit was located in the image plane. The photomultiplier could be driven transverse to the optical axis, as indicated in FIG 12, in order to investigate the spatial variation of light intensity in the image plane. The slit widths used were $\leq$ 25 microns, and the length of the slit was about 5 mm. The optical gain (magnification) provided by the focussing lens was about 17, so that the slit width, referred to the near field or object plane, provided an effective resolution of better than 1.5 microns. To examine A.C. components of the image plane distribution, the photomultiplier signal was processed by a Hewlett Packard model 8555A spectrum analyzer, operated in zero-scan mode. The resulting

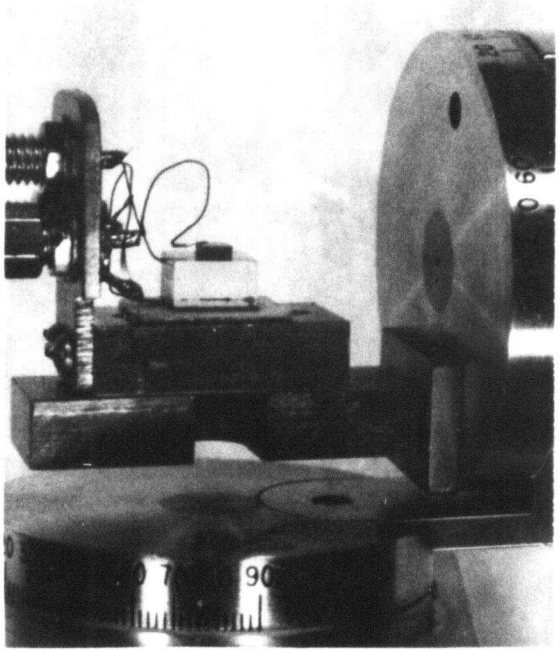

(a)

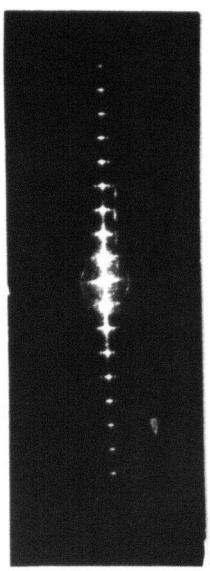

(b)

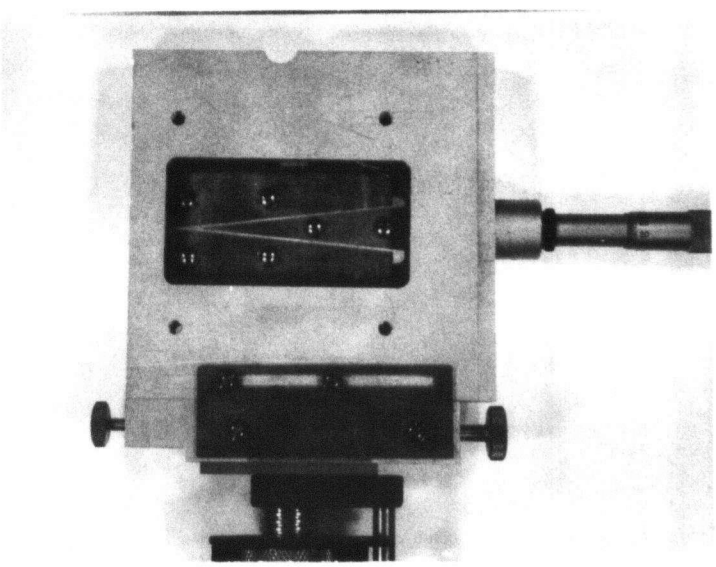

(c)

FIG 13. (a) Composite cavity DC2 on its goniometer mount, (b) typical focal plane diffraction pattern, (c) focal plane spatial filter.

signal was essentislly the magnitude of the Fourier component for the temporal term to be examined [refer to equations (1.110) and (1.11)].

1.4.2 Optical Verification of Mode-Locking

In FIG 14 photographs and traces of the image plane signal are presented for mode-locked operation of composite cavity DC1 (refer to Appendix B), with a fundamental acoustic frequency of 11.71 MHz. The corresponding wavelength Λ of the acoustic fundamental was 321 microns in fused quartz. The time and frequency displays of the acousto-electric current correspond to FIG 10. FIG 14(a) is simply a bright field photograph of DC1. FIG 14(b) shows the image plane intensity variation of the D.C. term [equation (1.103), FIG 8]. Its form agrees well with the theory of section 1.3.3, and this experimental evidence provided the first direct evidence of mode-locking of the acoustic signal in phonon masers (Smeaton, Hughes, Vrba and Haering 1976). The width of the resulting strain pulses, inferred from FIG 14(b), was about 23 microns, which corresponds to about 6 nanoseconds at the shear velocity of sound in fused quartz.

By spatially filtering symmetric pairs of diffraction spots in the focal plane, each component of the sum in equation (1.103) could be examined individually. FIG 14(c) and (d) are the profiles of the components for n=1 and n=2. If a reference was chosen at a maximum of the n=1 component, the cosine components for n odd were found to be (nearly) π out of phase with those for n even [compare FIG 14(c) and (d)], as is predicted by equation (1.103).

FIG 14. Photographs and traces of the image plane intensity distribution for DC1, corresponding to (a) the bright field image of DC1, (b) the total D.C. dark field term, (c) the n = 1 and (d) n = 2 components of the dark field term. The lengths indicated refer to the near field or object plane. The detector slit width, or effective resolution, referred to this plane is about 1.5 microns. Operating conditions: applied D.C. electric field = 0.83 KV/cm, D.C. current density = 11.1 mA/cm^2. Fundamental acoustic frequency = 11.71 MHz. (after Smeaton, Hughes, Vrba, and Haering 1976).

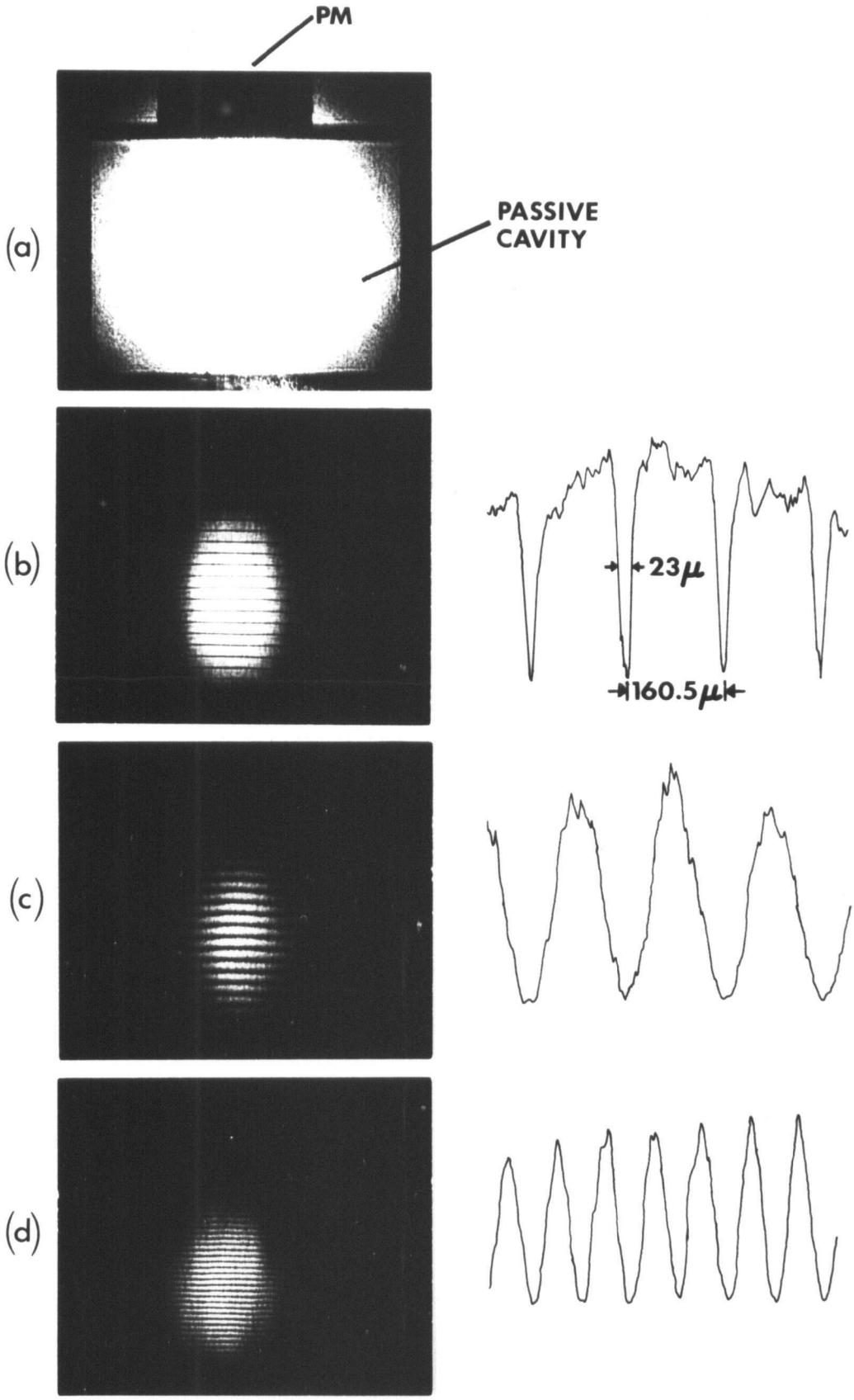
PM
PASSIVE CAVITY
(a)
(b)
23μ
160.5μ
(c)
(d)

At higher operating conditions narrower strain pulses could be achieved. In FIG 15 the profile of the D.C. term is shown for mode-locked operation of DC1 with the same acoustic fundamental as in FIG 14, but at a higher operating voltage. The average width of the dark fringes in FIG 15 is about 17.5 microns, corresponding to a pulse length of about 4.6 nanoseconds. At yet higher applied fields, pulse lengths of about 3 nanoseconds were inferred from the dark field measurements. The phonon maser was not very stable in this regime, however, possibly due to heating effects, and could only be maintained at this level for short periods of time.

The acoustic strain amplitudes used in determining the theoretical profile in FIG 8 were obtained for the same operating conditions as in FIG 15. If $\Lambda/2$ is taken as 160.5 microns in FIG 8, the width PW is about 20.2 microns. This is slightly larger than the average dark fringe width in FIG 15, owing to the fact that only the first 13 acoustic amplitudes were used in the theoretical profile.

While the intensity profile of the D.C. term (FIG 14(b), 15) provides an estimate of the strain pulse width, it contains no information about the exact form of the strain profile, since the phases δ_n [equations (1.84), (1.85)] are not present in equation (1.103). By applying spatial and temporal filtering techniques of the type outlined in section 1.3.3, it has been shown (Smeaton and Haering 1976a) that the necessary phase information can be recovered. Examples of experimental data, together with their best fitting theoretical curves, are presented

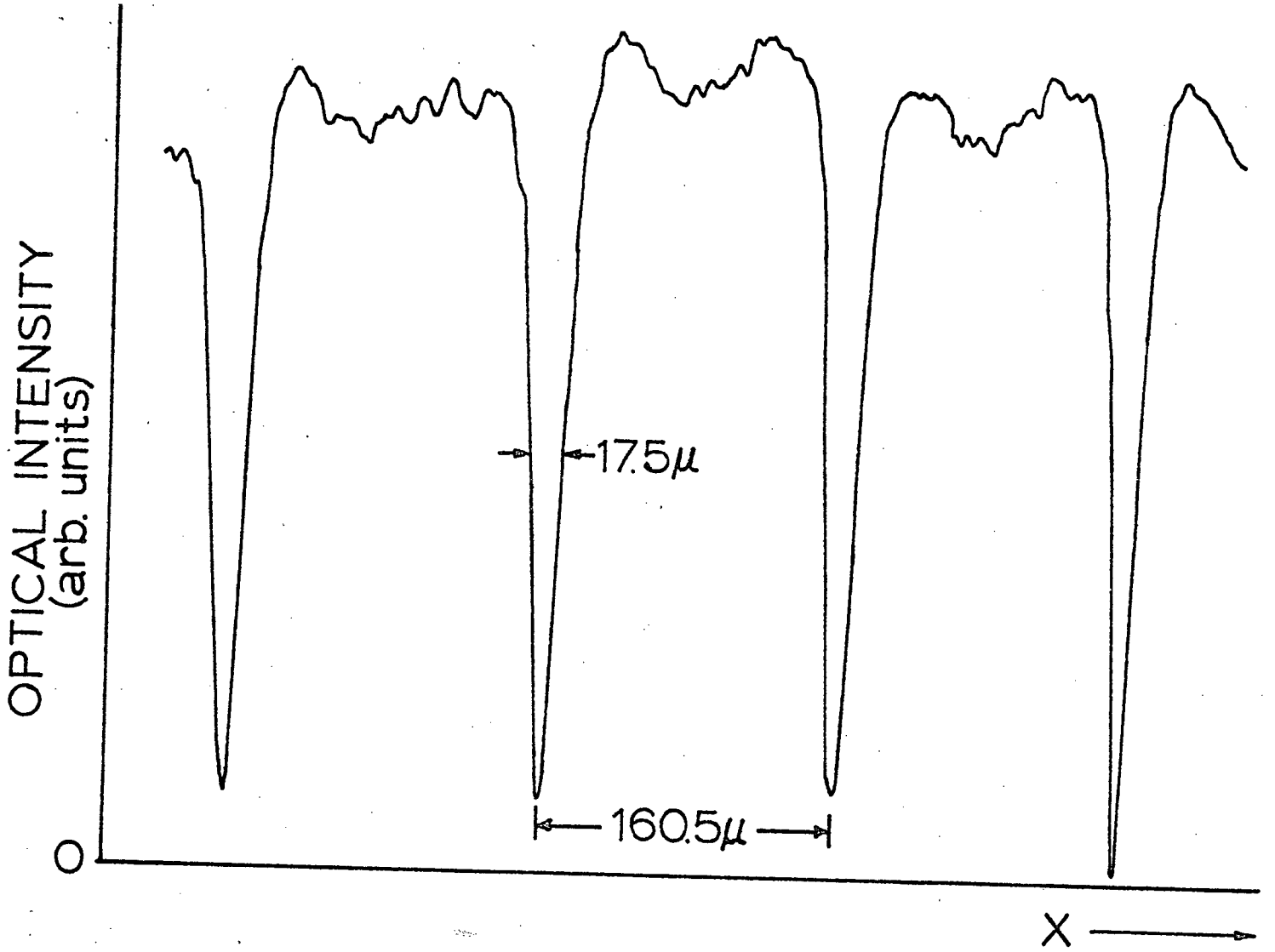

FIG 15. D.C. dark field term for DC1 under the operating conditions: applied D.C. electric field = 1.17 KV/cm, D.C. current density = 24 mA/cm^2. The fundamental acoustic frequency = 11.71 MHz.

in FIG 16. This data was taken for mode-locked operation of DC1 at the same fundamental frequency of 11.71 MHz as in FIG 10,14,15, and under the same operating conditions as in FIG 15. FIG 16(b) corresponds to the same conditions of spatial and temporal filtering as FIG 9. The success of the theoretical model is readily apparent. It was usually possible to fit the experimental profiles to within 10 degrees.

By employing various combinations of spatial and temporal filtering, it was determined that, to within experimental error, the phases δ_n formed an arithmetic series of the form

$$\delta_1,\delta_2,\delta_3,\ldots\ldots = 0,\alpha,2\alpha,\ldots\ldots \qquad (1.119)$$

where $\alpha \simeq 238°$ for the situation depicted in FIG 16. The phases in (1.119) are measured relative to δ_1 , i.e. a reference has been chosen corresponding to $\delta_1 = 0$. The strain amplitudes and phases obtained for the fundamental and the first 12 harmonics are given in TABLE 1. FIG 17 is the strain profile reconstructed from the data listed in TABLE 1.

It should be mentioned that, due primarily to the fact that the measurements allowed only the magnitude of different linear combinations of the phases to be determined, the data obtained allowed for two possible strain profiles: that presented in FIG 17 and a second profile obtained by inversion. The physically correct profile was inferred from the form of the acousto-electric current signal for mode-locked operation. In the active cavity, the piezoelectric potential corresponding to the strain profile in FIG 17 would be consistent with strong electron

FIG 16. Experimental (upper) and corresponding theoretical (lower) image plane intensity profiles for DC1 under different conditions of spatial and temporal filtering:

(a) spatial orders 3,4,5 with temporal filter at Ω; theoretical profile: $\delta_3 - 2\delta_4 + \delta_5 = 0$

(b) " 4,5,6 " Ω; " $\delta_4 - 2\delta_5 + \delta_6 = 0$

(c) " 1,3 " 2Ω; " $3\delta_1 - \delta_3 = 115°$

(d) " 3,4,5,6 " 2Ω; " $\delta_3 - \delta_4 - \delta_5 + \delta_6 = 0$

(e) " 4,5,6,7 " 2Ω; " $\delta_4 - \delta_5 - \delta_6 + \delta_7 = 0$

(f) " 5,6,7,8 " 2Ω; " $\delta_5 - \delta_6 - \delta_7 + \delta_8 = 0$

In all cases the periodicity of the profiles is $\Lambda/2$ = 160.5 microns, but different scaling factors have been used. Operating conditions: applied D.C. electric field = 1.17 KV/cm, D.C current density = 24 mA/cm^2. The fundamental acoustic frequency = 11.71 MHz.

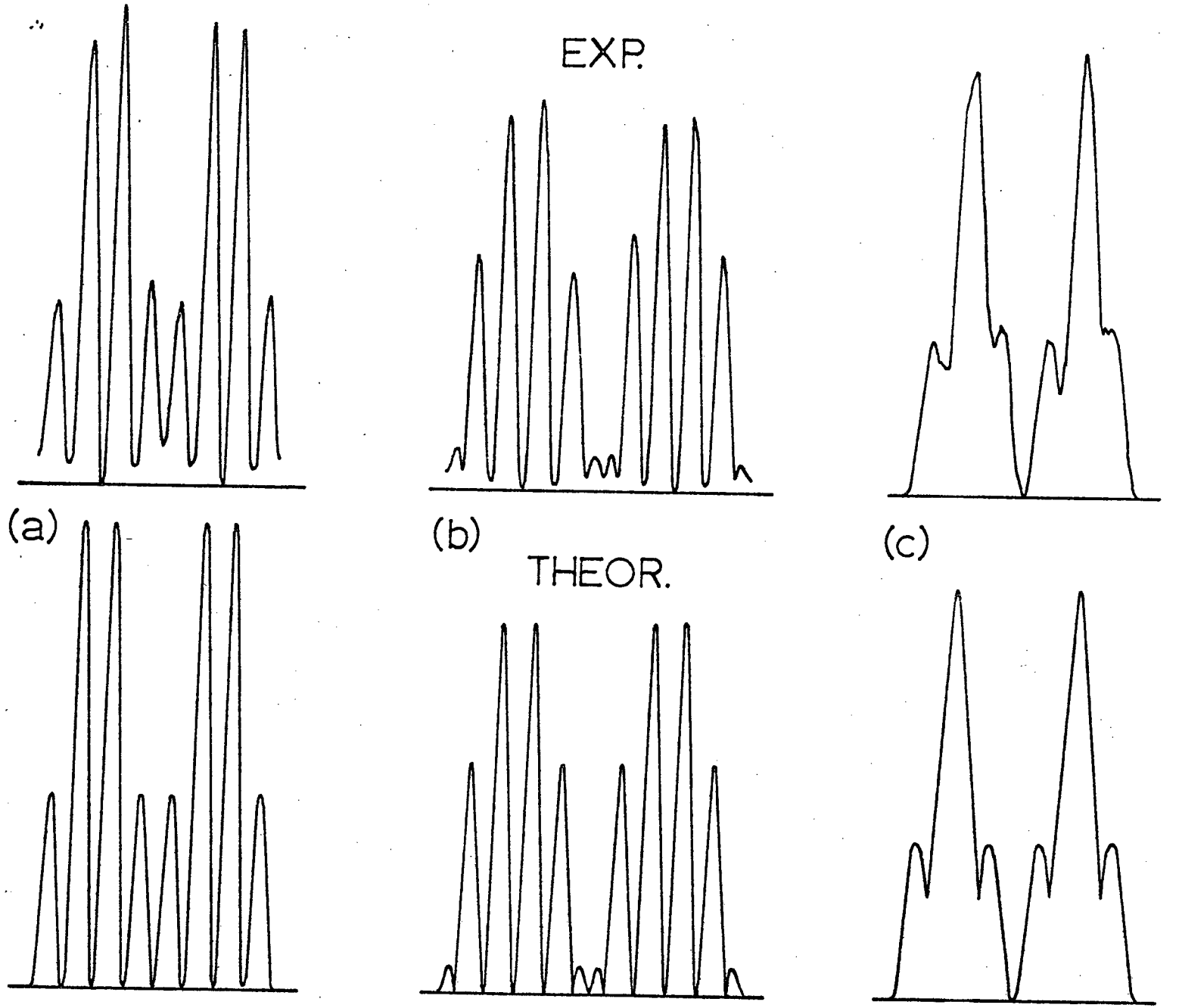
EXP.
(a)
(b)
(c)
THEOR.

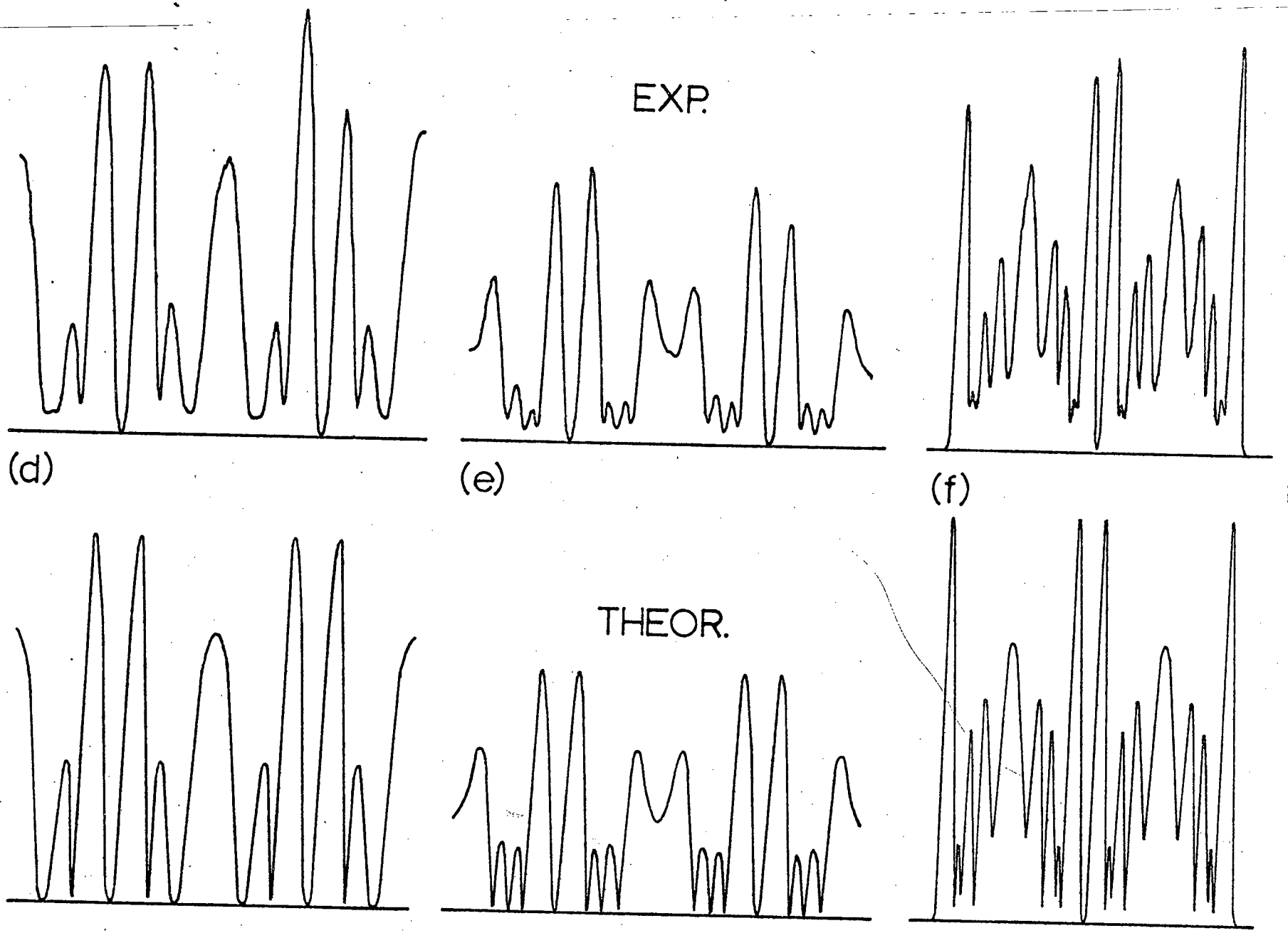
EXP.
(d)
(e)
(f)
THEOR.

TABLE 1

Experimentally determined strain amplitudes and phases for mode-locked operation of DC1 under the conditions: fundamental acoustic frequency = 11.71 MHz, applied D.C. electric field = 1.17 KV/cm, D.C. current density = 24 mA/cm^2. (after Smeaton and Haering 1976a).

n	STRAIN x 10^6	δ_n (degrees)
1	5.87	0
2	6.62	238
3	5.47	115
4	4.39	353
5	3.33	230
6	2.45	108
7	1.68	345
8	1.28	223
9	1.06	100
10	0.86	338
11	0.71	215
12	0.55	93
13	0.50	330

Fig 17. The acoustic strain profile for DC1, reconstructed from the experimentally determined strain amplitudes and phases listed in TABLE 1. Operating conditions: applied D.C. electric field = 1.17 KV/cm, D.C. current density = 24 mA/cm^2. Fundamental acoustic frequency = 11.71 MHz. (after Smeaton and Haering 1976a).

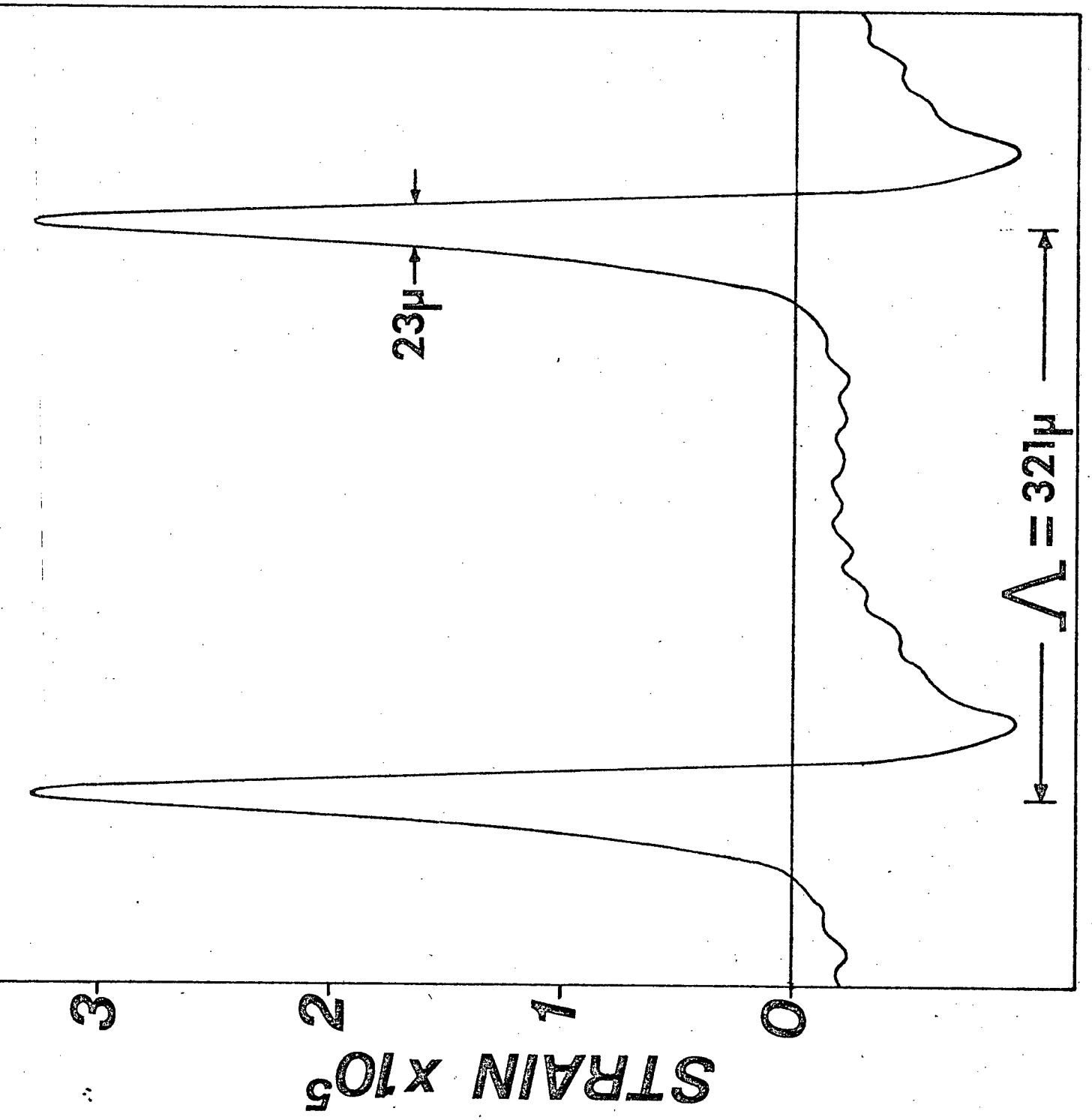
STRAIN x10⁵
3
2
1
0
23μ
Λ = 321μ

bunching, giving rise to dominant negative spikes in the acousto-electric current. This is, in fact, what is generally observed [see FIG 11(b)].

The width of the pulses in FIG 17 is about 23 microns, which corresponds to a pulse duration of about 6 nanoseconds at the shear velocity of sound in fused quartz. This is somewhat larger than the width of the dark fringes for the corresponding dark field term, FIG 15, due primarily to the fact that only the first 13 modes were used in obtaining the profile in FIG 17. A more direct comparison may be made between FIG 17 and FIG 8, since the number and relative amplitudes of the acoustic modes are the same for both these profiles. The width PW in FIG 8 is about 20.2 microns for $\Lambda/2 = 160.5$ microns, in reasonable agreement with the pulse width in FIG 17. Hence the dark field profile does, in fact, provide a reasonable estimate of the corresponding strain pulse width.

As has been mentioned, the minimum pulse duration achieved, as inferred from dark field measurements, was about 3 nanoseconds. Also, it was possible to achieve peak strains, as estimated from measurement of diffraction intensities, in excess of 5×10^{-5}. Due to instability of the phonon maser in this high operating range, detailed optical measurements were not possible.

The acoustic pulses produced by a mode-locked phonon maser are unique for their narrow width. There is no other known source of nanosecond acoustic strain pulses. An additional unique property may be seen if one considers the product of center frequency, or frequency

of maximum gain, and pulse width. The phonon maser has a center frequency of about 10^8 Hz and a pulse width of $\lesssim 5 \times 10^{-9}$ sec.. Hence it produces "D.C." pulses which only contain about 1/2 cycle of the carrier.

The composite cavity fundamental frequency, or reciprocal of the round-trip transit time, was 323.4 KHz for DC1. The frequency spacing of the active modes in strong mode-locked operation was usually close to a multiple of the reciprocal of the round-trip transit time of the active cavity, about 736 KHz. While it was not possible to achieve true mode-locking at the composite cavity fundamental frequency, an interesting multimode form of operation could be achieved, and the corresponding acousto-electric signal is shown in FIG 18. The display in FIG 18(a) consists of groups of lines separated by the composite cavity fundamental frequency. The modes within a single group [see FIG 18(b)] had amplitudes randomly varying in time, indicating the absence of phase-locking.

The acoustic modes participating in mode-locked operation were found to be harmonically related to better than 1 part in 10^4. For single frequency oscillation, composite cavity modes are not harmonic, but differ from harmonicity by an amount determined by the acoustic impedance mismatch between the two members of the composite cavity (Hughes and Haering 1976). For fused quartz and the chosen orientation of CdS, the maximum deviation from harmonicity is less than 3 KHz, and the amount of mode-pulling required to induce harmonicity for mode-locked operation is minimal. On this basis, one would predict that mode-locking should be difficult to achieve in composite cavities

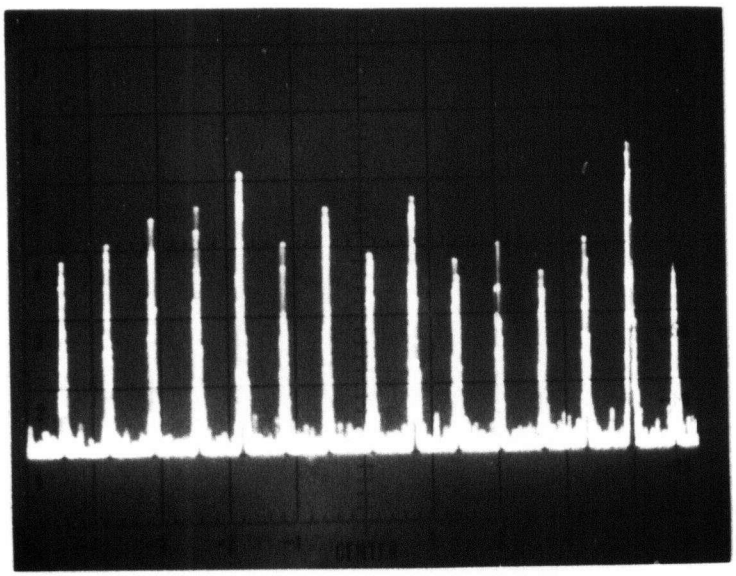

(a)

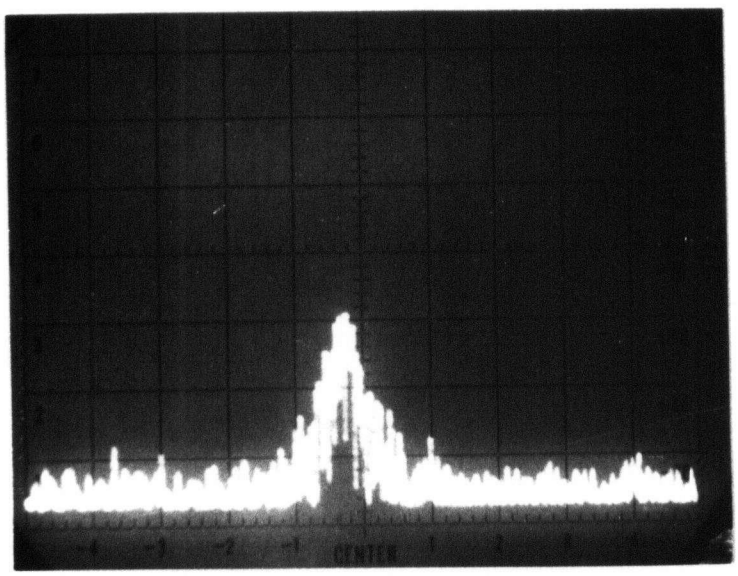

(b)

FIG 18. Frequency display of the acousto-electric current for DC1 operated under the conditions: applied D.C. electric field = 1.32 KV/cm, D.C. current density = 13.3 mA/cm^2. Horizontal scale is (a) 0.5 MHz/div., (b) 20 KHz/div.

whose members differ considerably in acoustic impedance. For example, if sapphire is substituted for fused quartz as the material for the passive cavity, the maximum deviation from harmonicity is greater than 100 KHz (Hughes and Haering 1976). A composite cavity formed with a $b\perp$ phonon maser and a sapphire passive cavity (DC3) was found, in fact, not to display strong mode-locking characteristics.

1.5 Optical Determination of the Normal Modes of Composite Cavities

The normal modes of composite cavities have previously been obtained by measurement of the active admittance as a function of frequency (Hughes and Haering 1976). In this situation, the composite cavity was located in one arm of a symmetrical admittance bridge. Since the bandwidth of the phonon maser is $\gtrsim$ 300 MHz, the bridge was required to be accurately balanced over a wide range in order to examine the cavity modes of interest.

A much simpler, optical technique may be applied in many situations. Using a configuration similar to FIG 12, the normal modes of composite cavity DC1 were measured by monitoring the intensity of diffracted light as a function of frequency. The active crystal was driven by a Hewlett Packard model 8601A sweep oscillator (maximum output voltage 3 V rms). No attempt was made to optimize signal to noise by use of phase sensitive detection or other techniques. A typical spectrum is shown in FIG 19. The spacing of the lines ($\simeq$ 323 KHz) corresponds to the reciprocal of the round trip transit time of the composite cavity.

The ratio of the line width to the center frequency for the modes in FIG 19 is a factor of 2 larger than for the electrical impedance measurements of Hughes and Haering (1976). This is due to Q-spoiling of the active cavity produced by the presence of residual scattered laser light. With proper light shielding and optimization of the experimental arrangement, the optical technique should easily match

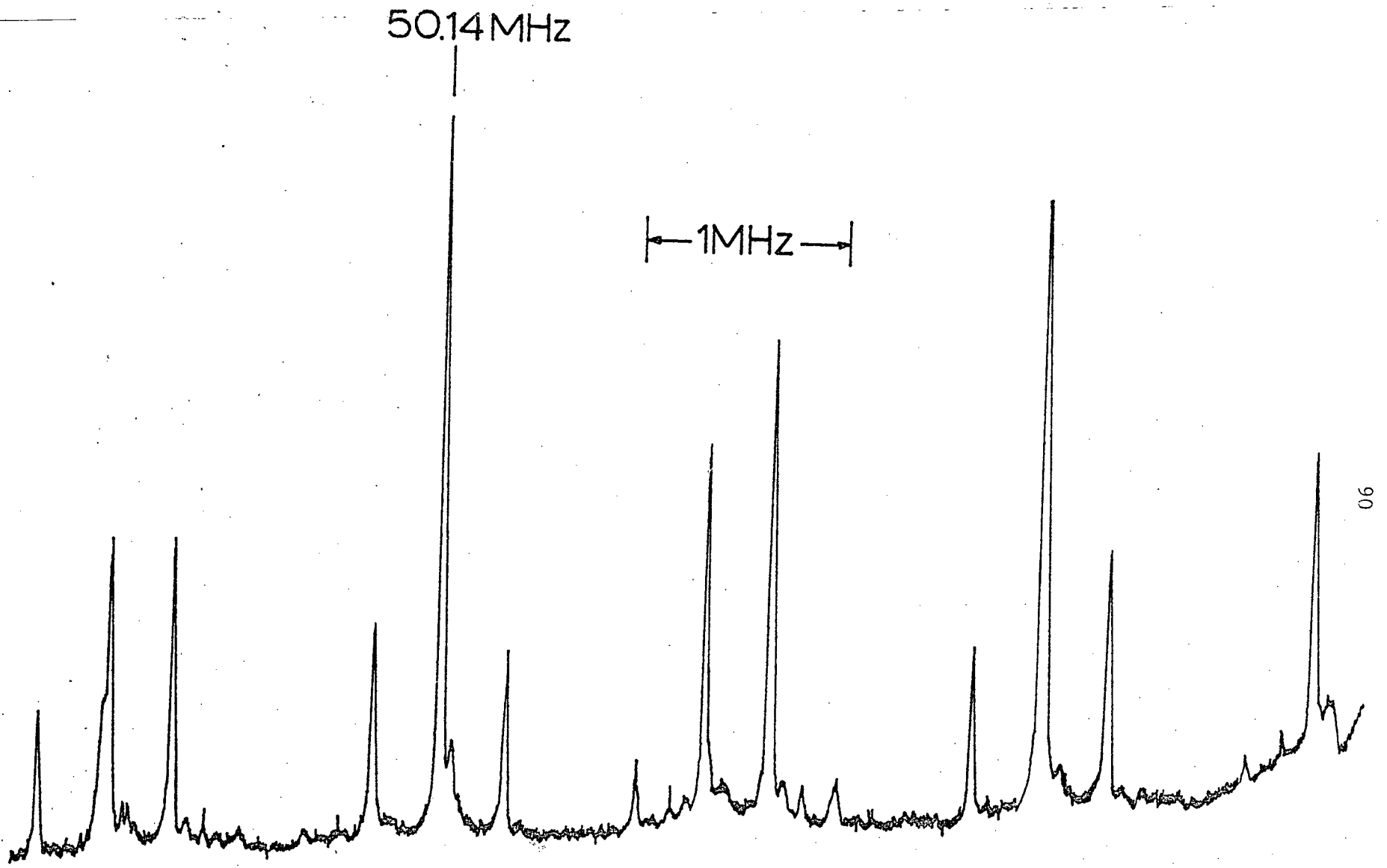

FIG 19. Mode structure of composite cavity DC1, obtained by optical diffraction techniques.

the resolution of the electrical measurements.

Aside from inherent simplicity, the optical technique has the advantage of wide frequency capability. Using a Hewlett Packard model 3200B VHF oscillator to drive the active crystal, diffraction could be observed by eye for frequencies in excess of 400 MHz. In fact, if the Bragg condition is optimized, there is, in principle, no restriction on the frequencies to be examined.

The major disadvantage of this technique is that it restricts the form of the passive cavity. The passive cavity must be transparent for one of the laser lines available, and should have a thickness $\gtrsim$ 200 microns. In addition, anisotropic materials must be oriented so that the appropriate optoelastic constants are non-zero. These constraints are satisfied, however, for many cases of practical interest.

1.6 Conclusions and Summary of Contributions

By applying the nonlinear theory of Butcher and Ogg (1968, 1969, 1970), it was shown that mode-locking can be predicted as a natural consequence of the structure of the phonon maser and nonlinear properties of the acousto-electric amplifying mechanism. The first direct evidence of mode-locking was provided by employing laser diffraction and spatial filtering techniques (Smeaton, Hughes, Vrba and Haering 1976), and by means of a unique combination of spatial and temporal filtering sufficient phase information was recovered to allow reconstruction of the mode-locked strain profile (Smeaton and Haering 1976a). The general technique of combining spatial and temporal filtering provides a powerful method of processing and analyzing optical signals.

At high operating conditions, strain pulses of width $\simeq$ 3 nanoseconds and amplitude $> 5 \times 10^{-5}$ were achieved. For future experiments, it would be of interest to investigate mode-locking for phonon masers at low temperatures. The lattice loss term, which reduces the acoustic bandwidth (Burbank 1971), should be smaller in this situation. Hence wider bandwidths and correspondingly narrower strain pulse widths should be achieved.

CHAPTER 2

APPLICATION OF OPTICAL PROCESSING TO A STUDY OF ACOUSTICALLY INDUCED SPACE CHARGE GRATINGS IN CdS

2.1 Introduction

Acoustic echo phenomena in piezoelectric semiconductors have received considerable experimental and theoretical attention (Yushin et al 1975, Chaban 1972, 1974, 1975, Shiren et al 1973, Shiren 1975, Melcher and Shiren 1975, Maerfeld and Tournois 1975). These effects result from a nonlinear interaction of the electric field produced by an active acoustic mode of wave number K and angular frequency Ω, with an externally applied, spatially invariant A.C. electric field of frequency equal, or harmonically related to Ω.

Of present interest are so-called 3 pulse echoes (Shiren et al 1973) which are produced in the following manner. At t=0 an acoustic pulse of wave number K and angular frequency Ω is introduced into a piezoelectric crystal. This may be achieved by means of an external transducer, or, more commonly, by applying an R.F. pulse to the sample, thus producing an acoustic pulse via the piezoelectric interaction. At a later instant $t=\tau$, an R.F. pulse of frequency Ω (or harmonically related to Ω - Melcher and Shiren 1975) is applied to the crystal. Aside from piezoelectric effects, this second pulse will produce a spatially invariant A.C. field in the crystal. If, at time $t=\tau+T$, another R.F. pulse is applied, an echo pulse is recorded at time $t=2\tau+T$.

In some recently proposed models (Melcher and Shiren 1975, Chaban 1975), localized electron traps play a fundamental role in the formation of echoes. It is postulated that a nonlinearity in the system produces a redistribution of the trapped charge, which, in turn, produces a static electric field distribution whose spatial variation mirrors the periodicity of the propagating acoustic wave. There is some controversy over the nonlinear mechanism involved, and there are two basic models of the interaction:

(i) Electron "bunching": In this model, set forth in theoretical papers by Chaban (1972, 1974, 1975), the periodic piezoelectric potential associated with the propagating acoustic wave gives rise to a modulation ("bunching") in the conduction band electron density. The electron density then has the form [see equation (1.9)]:

$$n(x,t) = n_o + n_1 e^{i(Kx-\Omega t)} + c.c. \qquad (2.1)$$

where n_o is the equilibrium electron density. At the instant $t=\tau$ an A.C. electric field of the form

$$E_1 e^{i\Omega t} + c.c. \qquad (2.2)$$

is applied along the x-axis of the crystal. Since the current density, equation (1.6), contains a nonlinear term proportional to the product of (2.1) and (2.2), it will have a time invariant component of the form e^{iKx}.

A periodic space charge will be built up to compensate for this current. Hence trapping will be more intense in some parts of the crystal than in others and, in the absence of the acoustic and electrical signals, a bound space charge will exist, having the spatial periodicity of the acoustic wave.

(ii) Electric field-assisted detrapping (Shiren et al 1973, Shiren 1975, Melcher and Shiren 1975): In this model one considers the total electric field E_t in the crystal at time $t=\tau$. It is given by the sum of the piezoelectric field (amplitude E_2) of the propagating acoustic wave, and the spatially uniform A.C. electric field:

$$E_t(x,t) = E_1 e^{i\Omega t} + E_2 e^{i(Kx-\Omega t)} + c.c. \qquad (2.3)$$

It is assumed that the total electric field in equation (2.3) produces field-assisted detrapping of electrons initially uniformly distributed in shallow traps. Since this process is highly nonlinear (Haering 1959), it gives rise to many components in the conduction electron density harmonically related in time and space to the total electric field. In a manner similar to (i), the nonlinear current density [equation (1.6)] will then contain spatially nonuniform, time invariant terms and, in the absence of the perturbing fields, a stored periodic space charge pattern will exist.

For both (i) and (ii), the charge grating will decay with a time constant related to the lifetime of the traps involved. If the A.C. electric field is again pulsed at time $t=\tau+T$, it will interact

with the periodic electic field of the space charge grating to produce a backward propagating (time reversed) acoustic wave (as well as a forward wave), which is detected as a pulse echo at the surface of the crystal at time $t=2\tau+T$.

Experimental data regarding acoustically induced space charge gratings has been obtained almost exclusively by pulse echo measurements, and it is of considerable interest to find an experimental technique that will provide supplementary information. Since the electric field produced by a static space charge grating will modulate the refractive index in a piezoelectric crystal, via the primary and secondary electro-optic effect (Nye 1964), optical measurements are indicated. The variation in the indicatrix produced by the electro-optic effect may be represented by (Nye 1964) [c.f. equation (1.43)]:

$$\Delta B_{ij} = z_{ijk} E_k \tag{2.4}$$

where z_{ijk}, E_k are components of the electro-optic tensor and the electric field. Contracting the indices ij according to equation (1.45) allows equation (2.4) to be represented in matrix form, in a manner exactly analogous to equation (1.47).

For hexagonal 6mm symmetry, appropriate for CdS, the electro-optic matrix has the form (Nye 1964):

$$\begin{pmatrix} 0 & 0 & z_{13} \\ 0 & 0 & z_{13} \\ 0 & 0 & z_{33} \\ 0 & z_{42} & 0 \\ z_{42} & 0 & 0 \\ 0 & 0 & 0 \end{pmatrix} \tag{2.5}$$

For the case of an electric field parallel to the c-axis, for example, the appropriate electric field component is E_3 and one obtains:

$$\begin{pmatrix} \Delta B_1 \\ \Delta B_2 \\ \Delta B_3 \\ \Delta B_4 \\ \Delta B_5 \\ \Delta B_6 \end{pmatrix} = \begin{pmatrix} z_{13}E_3 \\ z_{13}E_3 \\ z_{33}E_3 \\ 0 \\ 0 \\ 0 \end{pmatrix} \tag{2.6}$$

The coefficients in equation (1.39) become:

$$B_1 = B_2 = \left(\frac{1}{n_o^2} + z_{13}E_3 \right)$$

$$B_3 = \left(\frac{1}{n_e^2} + z_{33}E_3 \right) \tag{2.7}$$

$$B_4 = B_5 = B_6 = 0$$

n_o, n_e are the ordinary and extraordinary refractive indices [refer to equation (1.42)]. The new indicatrix thus becomes:

$$\left(\frac{1}{n_o^2} + z_{13}E_3 \right)(x_1^2 + x_2^2) + \left(\frac{1}{n_e^2} + z_{33}E_3 \right) x_3^2 \tag{2.8}$$

For light propagating along the b or x_2 axis, the appropriate index ellipse is given by:

$$\left(\frac{1}{n_o^2} + z_{13}E_3 \right) x_1^2 + \left(\frac{1}{n_e^2} + z_{33}E_3 \right) x_3^2 \tag{2.9}$$

and has semiaxes:

$$\begin{aligned} n_o' &= \frac{n_e}{(1 + n_o^2 z_{13}E_3)^{1/2}} \\ n_e' &= \frac{n_e}{(1 + n_e^2 z_{33}E_3)^{1/2}} \end{aligned} \tag{2.10}$$

Since $n_e^2 z_{33}E_3$, $n_o^2 z_{13}E_3 \ll 1$, the square roots in (2.10) may be expanded to yield:

$$\begin{aligned} \Delta n_o &\simeq -\frac{1}{2} n_o^3 z_{13}E_3 \\ \Delta n_e &\simeq -\frac{1}{2} n_e^3 z_{33}E_3 \end{aligned} \tag{2.11}$$

∴

Equation (2.11) may be directly compared with equation (1.58). This strong analogy with the photoelastic effect indicates that it should be possible to apply the laser diffraction and spatial filtering techniques of CHAPTER 1, to directly observe acoustically induced space charge gratings.

2.2 Application of Optical Processing

In principle, it should be possible at low temperatures to observe diffraction from stored charge gratings which have been previously prepared by the application of suitable electric fields. In practice this has not proved possible with our crystals, presumably because the trapped charge is disturbed by the probing light used in the diffraction experiment. This is consistent with the experimental findings of Shiren et al (1973). For this reason, optical measurements were made with c⊥ CdS phonon masers which were driven at a resonant frequency by an external oscillator. In this steady state situation, the acoustically induced charge gratings exist in the presence of light. However, it is then necessary to devise a measurement technique which can distinguish between diffraction from a static charge grating and diffraction from the acousto-electric fields which are simultaneously present.

The electric field in the crystal may be written:

$$E(x,t) = E_1 e^{i\Omega t} + E_2[e^{i(Kx-\Omega t)} + e^{i(Kx+\Omega t)}] + c.c. \qquad (2.12)$$

where x is taken along the c-axis. It consists of a spatially invariant

term of frequency Ω and amplitude E_1, related to the driving field of the external oscillator; and an acousto-electric field of frequency Ω and wave number K, consisting of right and left going waves of equal amplitude E_2. The latter fields are produced via the piezoelectric interaction of the crystal with the driving field. Equation (2.12) does not take into account the electric fields produced by modulations of the space charge.

The static space charge grating is produced from the fields E_1 and E_2 in equation (2.12) by one of the nonlinear effects described in section 2.1, and, as was indicated, will produce a periodic modulation of the local refractive index of the crystal via the electro-optic effect. It thus presents a fixed phase grating to incident laser light and results in diffraction. In the Raman - Nath regime (refer to section 1.3.2 of CHAPTER 1) the diffraction patterm will consist of a row of spots symmetrically arranged about the zero order or undiffracted beam. The acousto-electric field E_2 will also produce diffraction due to photoelastic (section 1.3 of CHAPTER 1) and electro-optic coupling. In the experiments performed, this diffraction was roughly two orders of magnitude more intense than that produced by the static space charge. Moreover, since the spatial periodicity was the same in both cases, both diffraction patterns were superimposed. It was possible to completely separate the two optical signals, however, by means of spatial and temporal filtering.

This may be demonstrated by examining the optical phase transformation produced by the acoustic standing waveform. In analogy with equations (1.83) and (1.85), it may be written:

$$e^{i\phi_A} = e^{i2v\sin Kx\ \cos\Omega t} = \sum_{n=-\infty}^{\infty} J_n(2v\cos\Omega t)e^{inKx} \qquad (2.13)$$

The Bessel function relationship, equation (1.87), has again been used. The optical amplitude in the n^{th} order diffraction spot in the focal plane is proportional to $J_n(2v\cos\Omega t)$. Consider that only diffraction spots n and m are combined and imaged. The image plane intensity distribution is then proportional to

$$I_{n,m} = J_n^2(V) + J_m^2(V) + 2J_n(V)J_m(V)\cos(n-m)Kx \qquad (2.14)$$

where $V = 2v\cos\Omega t$ (2.15)

If we extract those components of (2.14) that have no time variation, the first two terms will contribute only a uniform background. From the well known relationship (Abramowitz and Segun 1968)

$$J_m(-z) = (-1)^m J_m(z) \qquad (2.16)$$

and the form of V in equation (2.15), it is apparent that the cross term in (2.14) will only contain a D.C. component if n+m is an even number. Thus for n+m odd, the D.C. part of the image plane signal will contain no terms with spatial variation. This is rigorously true, even if weak acoustically induced variations of the optical absorption coefficient are taken into account.

Consider a few special cases of particular interest:

[1] Adjacent diffraction orders, m = n+1 : the D.C. signal consists solely of a uniform background, produced by the first two terms in equation (2.14).

[2] Symmetric diffraction orders, m = -n : using equation (1.93), it is apparent that the D.C. component of (2.14) is proportional to $(1 - \cos 2nKx)$ [c.f. individual components of the dark field term, equation (1.103), see FIG 14(c),(d)]. Thus for n=1, for example, the image plane intensity distribution consists of a cosine pattern of bright and dark fringes with periodicity $\Lambda/2$, where $\Lambda = 2\pi K^{-1}$.

[3] m = n+2 : for this situation, the third term in (2.14) provides a D.C. component proportional to $\cos 2Kx$. Thus cosine fringes appear having periodicity $\Lambda/2$, similar to [2] with symmetric orders ±1. The fringes will be less distinct in this case, however, due to the presence of a uniform background D.C. component produced by the first two terms in (2.14).

Image plane photographs which illustrate the above results are shown in FIG 20. This data was taken with a model system consisting of two orthogonally arranged quartz transducers (resonant frequency 10 MHz) mounted in a cell of distilled water. The two transducers were driven simultaneously by a General Radio model 1211-C oscillator and a two dimensional diffraction pattern, FIG 20(a), resulted. In obtaining FIG 20(b)-(g) only the central vertical row of diffraction spots was used. It should be noted that the different spots in FIG 20(a) correspond

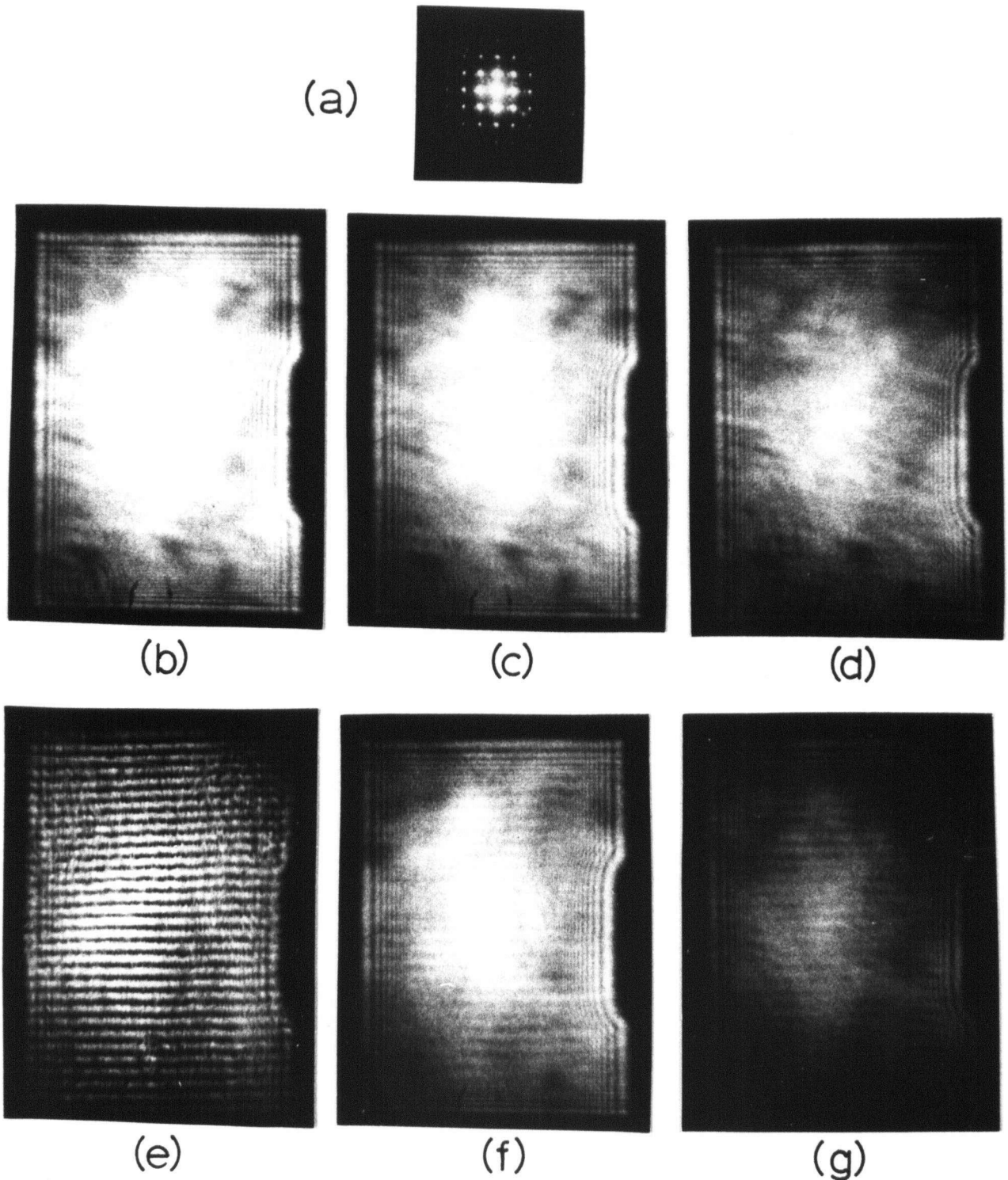

FIG 20. Experimental data obtained from a model system consisting of two orthogonal quartz transducers (resonant frequency 10 MHz) mounted in a cell of distilled water. (a) focal plane diffraction pattern. (b) zero order light imaged with sound generator off. Image plane distributions produced by combining and imaging diffraction spots (c) 0,1, (d) 1,2, (e) ± 1, (f) 0,2 and (g) 1,3.

to different orders of Raman - Nath diffraction from a simple sinusoidal acoustic waveform. In contrast, all spots in FIG 13(b) correspond to first order Raman - Nath diffraction from a waveform consisting of many harmonically related components.

In FIG 20(c) and (d) adjacent diffraction orders 0,1 and 1,2 , respectively, have been combined and imaged. By comparison with FIG 20(b), the zero order light with the sound generator off, it is apparent that no fringes are present, as was predicted in [1]. In FIG 20(e) symmetric orders ±1 have been imaged. A pattern of periodicity $\Lambda/2$, consisting of alternating dark and bright fringes is produced, in agreement with [2]. In FIG 20(f) and (g) orders 0,2 and 1,3 , respectively, have been imaged. A fringe pattern of periodicity $\Lambda/2$ is produced. As predicted in [3], the fringes are less distinct than in FIG 20(e).

If, in addition to ϕ_A in equation (2.13), a static phase grating is present, such as would be produced by a fixed space charge pattern, the image plane signal will be modified. A sinusoidal grating of period $\Lambda = 2\pi K^{-1}$ will produce a phase transformation

$$e^{i\phi_S} = e^{iv_o \sin Kx} \tag{2.17}$$

where v_o is the amplitude of the optical phase variation ($v_o << 1$). ϕ_S may be considered to be the fundamental component of the periodic space charge pattern. The phase ϕ_S (or the combination of ϕ_S and ϕ_A) produces an image plane D.C. term of the form cosKx, if diffraction

orders 0,1 (or any other pair of adjacent diffraction orders) are combined and imaged.

In practice, it was necessary to amplitude modulate the external oscillator and to phase-lock the image plane detector to the modulation frequency, in order to remove extraneous signals and optical noise in the image plane. With this in mind, the total phase transformation given by equations (2.13) and (2.17) may be written:

$$\exp i\left[(2v\cos\Omega t + v_o)(1 + M\cos\omega_m t)\sin Kx\right]$$

$$= \sum_{n=-\infty}^{\infty} J_n[(2v\cos\Omega t + v_o)(1 + M\cos\omega_m t)]e^{inKx} \qquad (2.18)$$

where M is the modulation index ($\simeq 0.1$ in practice) and ω_m is the modulation frequency. The Bessel functions in (2.18) may be Taylor expanded to yield:

$$J_n(2v\cos\Omega t + v_o) \;+\; (2v\cos\Omega t + v_o)M\cos\omega_m t\; J_n'(2v\cos\Omega t + v_o) \;+\; \ldots. \qquad (2.19)$$

In practice, $v_o, v \ll 1$ and $v_o \sim v^2$. It is therefore necessary to retain contributions to first order in v_o, and to second order in v. Only the first two terms in (2.19) need be considered since they contain all contributions to second order in both v and v_o. The derivative of the Bessel function in (2.19) may be expanded using the relation (Davis 1968):

$$zJ_n'(z) = nJ_n(z) - zJ_{n+1}(z) \qquad (n = 0,1,2.....) \qquad (2.20)$$

If diffraction orders 0,1 in equation (2.18) are combined and imaged, the resulting image plane intensity distribution is proportional to [see equation (2.14)]:

$$J_o^2(V') + J_1^2(V') + 2J_o(V')J_1(V')\cos Kx \qquad (2.21)$$

where $$V' = (2v\cos\Omega t + v_o)(1 + M\cos\omega_m t) \qquad (2.22)$$

Using equations (2.19), (2.20), the small argument expression for the Bessel function, equation (1.92), and extracting the component of (2.21) at frequency ω_m, the appropriate image plane signal is (to first order in v_o and second order in v):

$$I_{1,0}^{\omega_m} = M(v_o\cos Kx - v^2) \qquad (2.23)$$

Thus the presence of the static space charge grating is indicated by a cosine fringe pattern of periodicity Λ. The component $-Mv^2$ in equation (2.23) is a uniform background produced by acoustic diffraction effects. Its negative sign indicates that it is π out of phase with the amplitude modulating reference.

2.3 Experimental Results

The experimental arrangement for optical measurements was essentially the same as in FIG 12. The samples used were c$\perp$ CdS phonon masers, driven by an external oscillator. For this configuration, the piezoelectically active acoustic modes consist of longitudinal waves whose K-vectors lie along the c-axis. The light source was a 5 mW HeNe laser (λ = 6328 Å) and incident polarization was parallel to the c-axis. Aside from the laser light, no ancillary illumination of the crystals was used. A slit width of 250 microns was used for the scanning photomultiplier in the image plane (refer to FIG 12), and the magnification provided by the focussing lens was about 27. All measurements were made at room temperature.

FIG 21 shows examples of image plane profiles for c$\perp$ crystal 24.06.06.01. The external oscillator in this case was an Arenburg model PG-650C. The photographs on the LHS of FIG 21(b) and (c) were obtained by imaging diffraction orders ±1. The spacing of the bright fringes is thus $\Lambda/2$ (refer to section 2.2). The photographs on the right side of the figure were obtained by imaging orders 1,2. Weak, poorly defined fringes of spacing Λ may be discerned, suggesting the presence of a static phase grating.

To obtain more reliable data, the technique outlined in section 2.2 was employed. The crystals were driven by a Hewlett Packard model 3200B VHF oscillator, which was amplitude modulated at 3 KHz by a Wavetek model 114 oscillator. The amplitude modulating signal provided

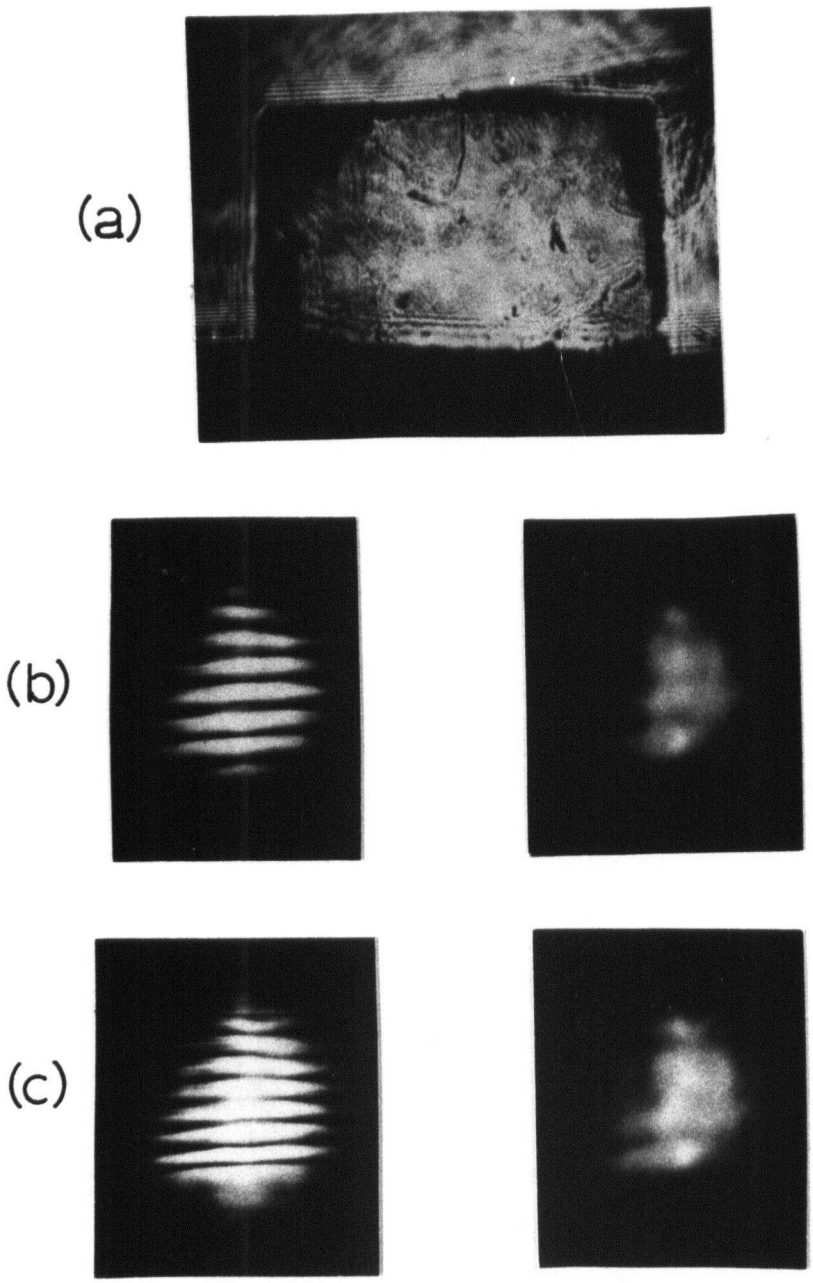

FIG 21. (a) Bright field image of $c_{\perp}$ crystal 24.06.06.01, and intensity profiles produced by imaging diffraction spots ±1 (LHS) and 1,2 (RHS) for driving frequencies (b) 15.619 MHz and (c) 19.062 MHz.

the reference for a P.A.R. model HR-8 lock-in amplifier, which was used to process the signal from the image plane detector. For typical operating conditions, the Raman - Nath parameter $v \leq 5 \times 10^{-2}$, as calculated from the diffraction intensities.

An example of the image plane signal for $c\perp$ crystal 24.06.06.01 is shown in FIG 22. The upper curve was obtained by imaging orders ±1. As has been indicated, the resulting profile has periodicity $\Lambda/2$ and is presented as a reference. The lower curve in FIG 22 was obtained by combining orders 0,1 (the variable amplitude of the optical signals is a reflection of the intensity profile of the laser beam). The appearance of sinusoidal fringes of spacing Λ is direct evidence for the presence of a fixed charge grating of the form sinKx [refer to equation (2.17)]. This sinusoidal term is superimposed on a larger negative (i.e. π out of phase with respect to the amplitude modulating reference) background term, in agreement with equation (2.23). By comparing the amplitude of these two signals it was possible, with the aid of equation (2.23), to estimate the value of v_o. Hence, with the aid of equations (1.2), (1.72) and (2.11), the peak electron density modulation associated with the static space charge grating could be calculated, and was found to be $\sim 10^{12}$ electrons/cm^3 at $\Omega/2\pi$ equal to 33 MHz. Much higher modulations have been reported in pulse echo measurements, performed at correspondingly higher frequencies and driving amplitudes (Shiren 1975).

To check these results, a double cavity (DC4) was constructed by bonding together two similarly oriented $c\perp$ CdS crystals. Either side

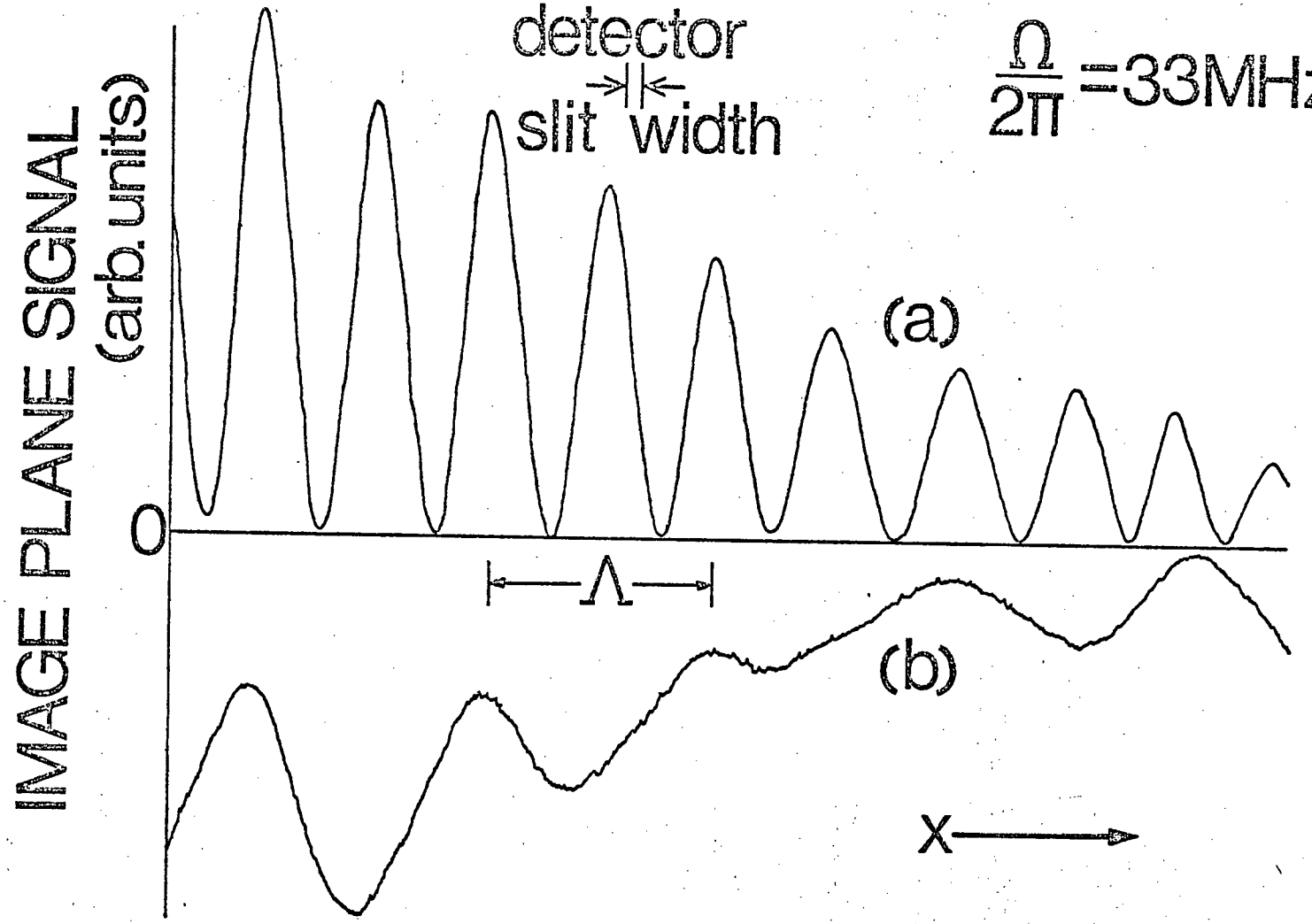

FIG 22. Image plane signal for c⊥ crystal 24.06.06.01, produced by imaging diffraction spots (a) ± 1 and (b) 0,1.

of the resulting composite cavity could be driven by an external oscillator. This produced a situation in which the acousto-electric field E_2 [see equation (2.3)] was of nearly constant amplitude throughout the composite cavity, but the external driving field E_1 was present only in one part. Laser diffraction could be done in one or both parts of DC4 and, as is demonstrated in FIG 23, the optical signals could be completely separated by focal plane spatial filtering. The image plane signal for one part of DC4, both in the presence and absence of the driving field E_1, is presented in FIG 24. The fact that the fringes require the simultaneous presence of E_1 and E_2 [equation (2.3)] indicates that they are not an artifact of the acousto-electric field alone.

For the measurement technique used, it was not possible to establish whether the static charge grating was associated with trapped or mobile charge. However, the strong sample dependence of our measurements is an indication of the importance of defects in producing the observed results. To determine the presence of shallow traps of the type postulated by Melcher and Shiren (1975), thermoluminescence measurements were performed. CdS samples, freshly etched in concentrated HCl, were mounted in a LHe dewar at 4.2°K. After being illuminated with strong band gap light, the crystals were maintained in the dark. Once the afterglow had subsided (10 - 15 min. after illumination), the samples were warmed up and the luminescent intensity was recorded as a function of time. The resulting glow curves were analyzed using the techniques of Garlick

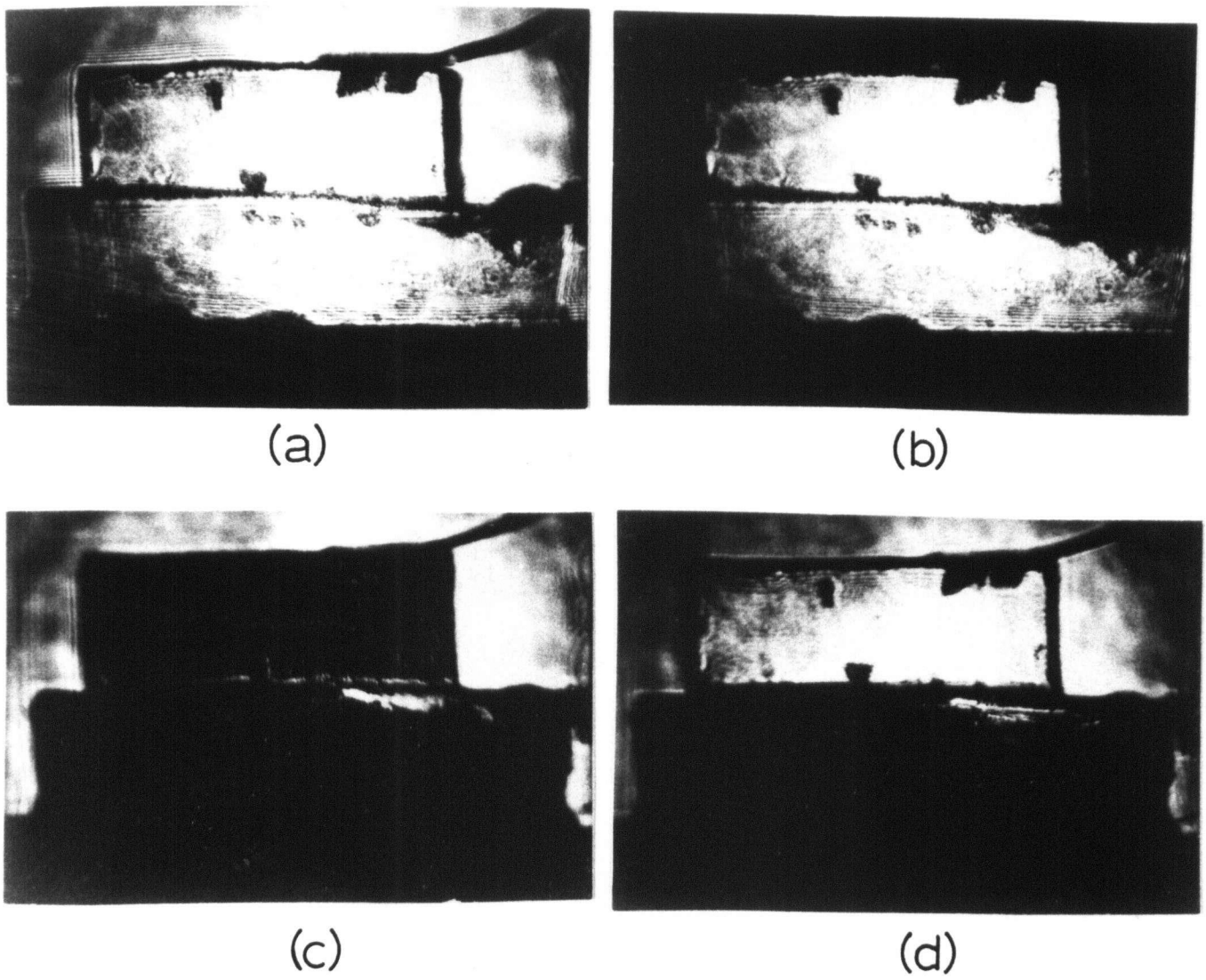

FIG 23. Image plane photographs of DC4, illustrating that different components of the optical signal may be examined individually. (a) all light has been imaged, (b) the background light has been removed, (c) only the background light has been imaged, (d) the light from the lower member of DC4 has been removed.

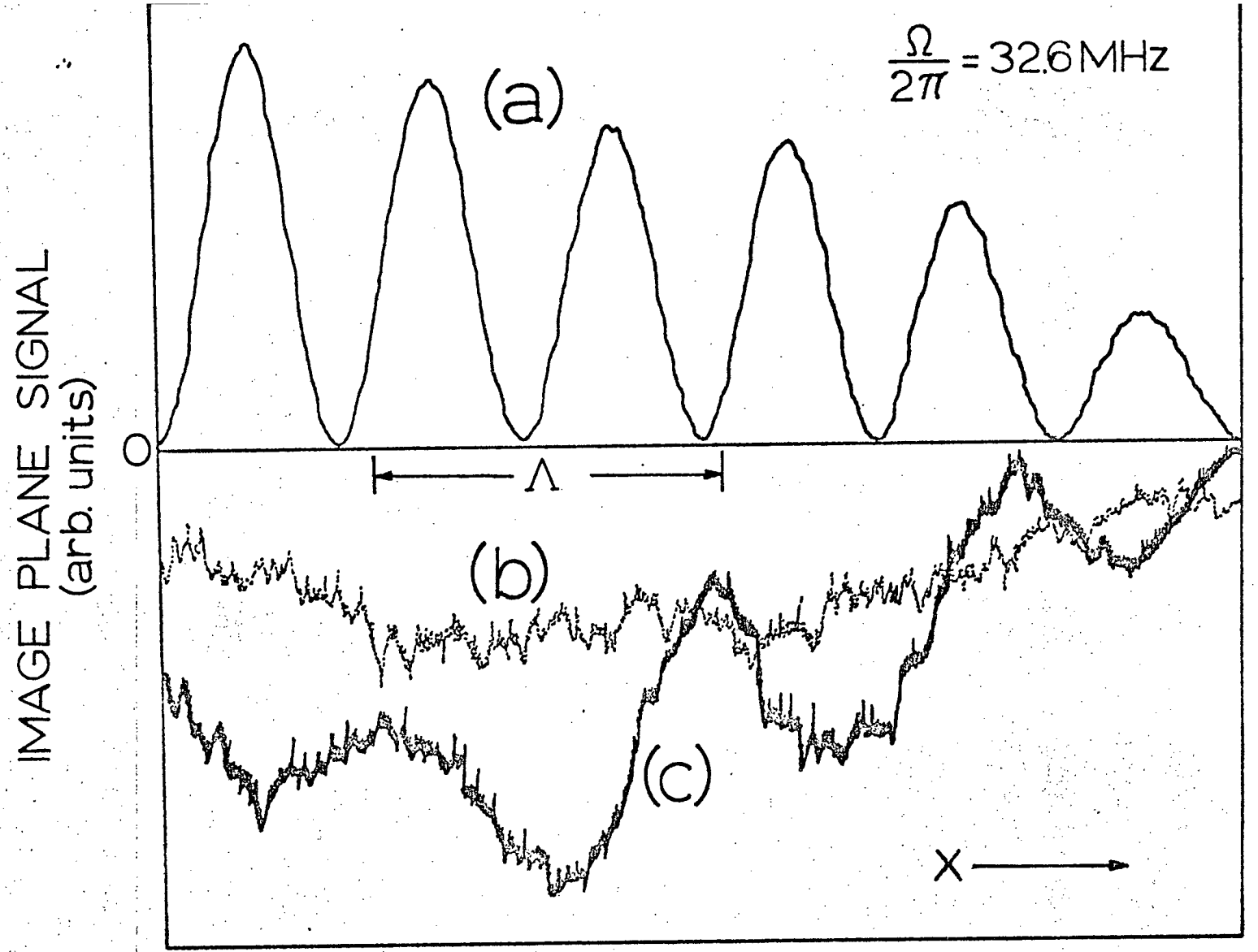

FIG 24. Image plane signals obtained from the upper member of DC4 in FIG 23. The profiles correspond to (a) orders ± 1 combined and imaged; and orders 0,1 imaged (b) in the absence and (c) in the presence of the external driving field.

and Gibson (1948), Grossweiner (1953) and Booth (1954). A typical spectrum is shown in FIG 25. As indicated, these measurements verified the existence of shallow traps with an ionization energy of about 20 meV, as required for the model proposed by Melcher and Shiren (1975) [refer to model (ii) in section 2.1].

In principle, the diffraction experiments could be extended to study the higher Fourier components of the static charge grating. This would be of interest since these components would yield information about the nature of the underlying nonlinearity. In practice, this extention has not been possible with our crystals because the observed diffraction effects were too weak.

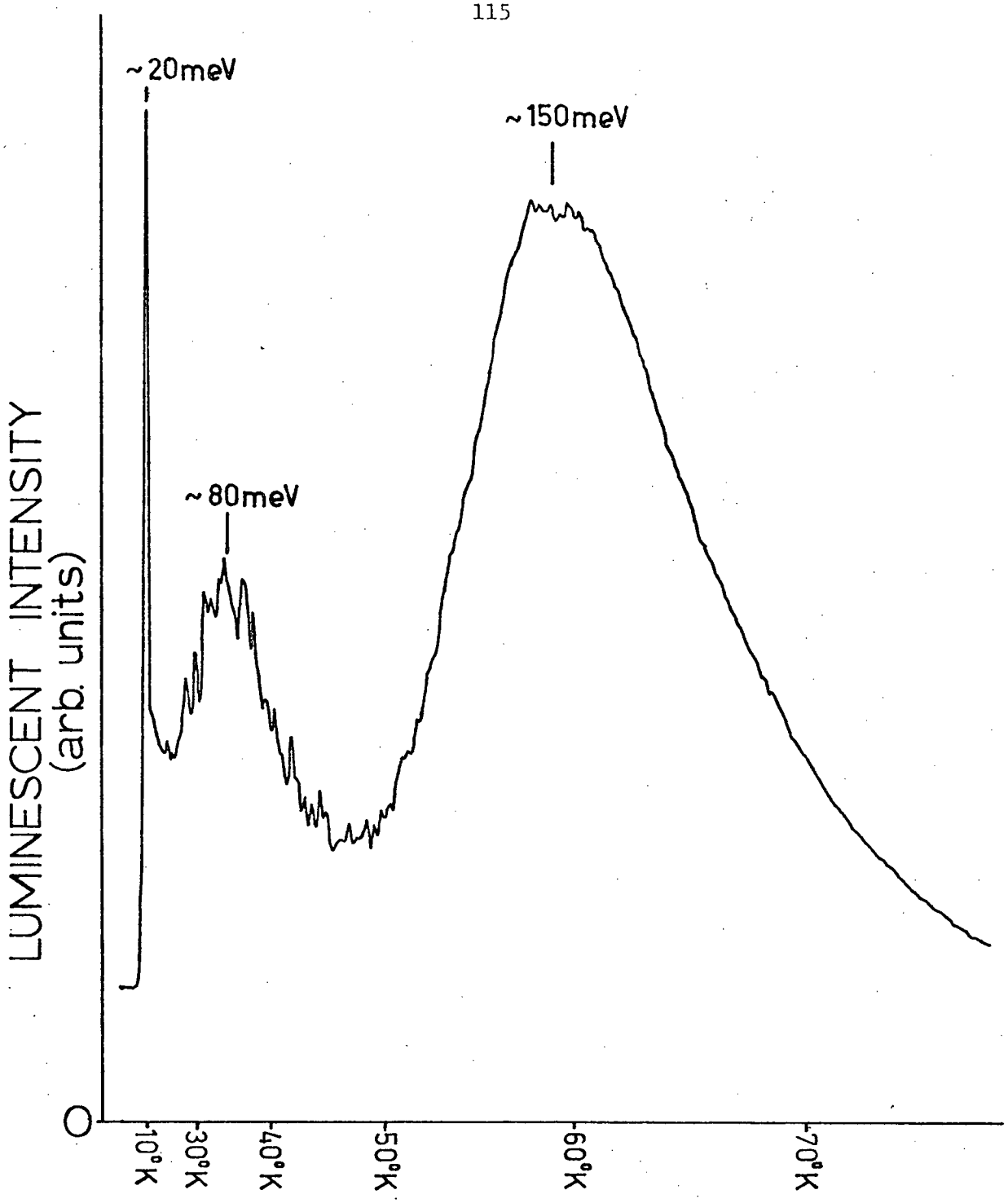

FIG 25. A typical glow curve obtained from a CdS crystal of the type used to construct phonon masers. The points at which different temperatures occurred are indicated on the horizontal axis, and the calculated trap ionization energies corresponding to the major thermoluminescent peaks are given.

2.4 Conclusions and Summary of Contributions

By means of the spatial and temporal filtering techniques outlined in CHAPTER 1, optical experiments were performed that allowed the first direct observation of acoustically induced space charge gratings in CdS (Smeaton and Haering 1976b). The information obtained by optical means should be of considerable supplimental value to data obtained by pulse echo measurements. Proper exploitation of the techniques described could provide insight into the underlying physical processes involved in the formation of the static charge gratings.

CHAPTER 3

NEW PHOTOVOLTAIC EFFECTS IN CdS

3.1 Introduction

Photovoltaic effects constitute a class of phenomena in which light generates a voltage across a portion of a semiconductor. Such effects have been observed for several decades in CdS and other semiconductors (for a review see Pankove 1971). The samples used in the present experiments were polished phonon maser crystals, constructed from high resistivity [10^{10} - 10^{12} $(\Omega cm)^{-1}$ in the dark] photoconductive CdS. For this situation, the dominant known photovoltage is produced via the Dember effect (Williams 1962). The Dember voltage results when strongly absorbed radiation generates a high density of electron-hole pairs, which then diffuse away from the illuminated surface. The electrons have a higher mobility than the holes and hence extend further into the crystal, tending to make the surface positive with respect to the bulk. This effect, and the resulting voltage, are named for their discoverer (see Dember 1931).

In this chapter some initial results from on-going experiments are presented to illustrate the existence of two new photovoltaic effects in CdS. As will be shown, these effects provide D.C. voltages which are several orders of magnitude larger than the Dember voltage. As yet, the underlying physical mechanisms are not understood.

3.2 The Photoacousto Voltaic Effect

A D.C. voltage, requiring the simultaneous presence of light and propagating acoustic fields, has been discovered in CdS phonon masers. The basic experimental configuration for measurement of the photoacoustic voltage is shown in FIG 26. Composite cavities, consisting of two similarly oriented $b\perp$ or $c\perp$ phonon maser crystals, were used in the experiments. The active side of the double cavity was used as a source of acoustic waves and was either driven by an external oscillator, or operated with a D.C. electric field to achieve phonon maser action. The free surface of the passive cavity was illuminated and the D.C. voltage appearing across the crystal was measured with a Keithley model 153 electrometer, or a Fluke model 8120A digital voltmeter.

The form of the photoacoustic voltage for DC5 as a function of light intensity is shown in FIG 27(a). The corresponding short circuit photoacoustic current had a maximum value $\lesssim 0.1$ mA/cm^2, and mirrored the light intensity dependence of the photoacoustic voltage. For comparison,

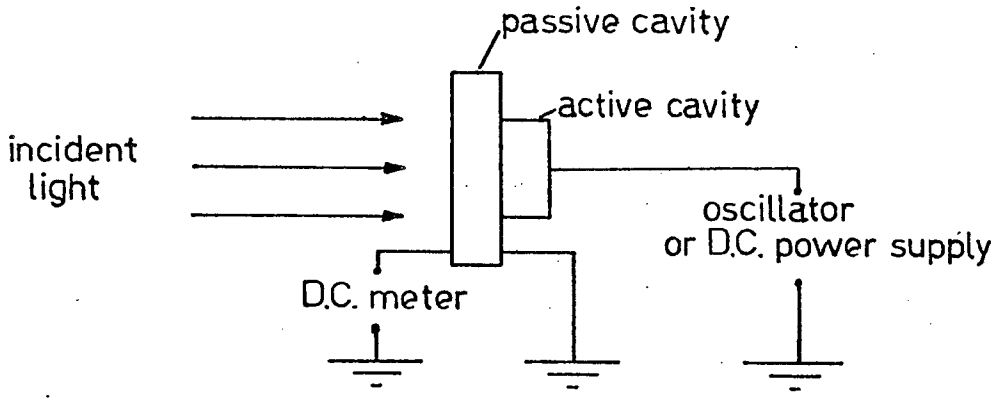

FIG 26. Experimental configuration for measuring the photoacoustic voltage.

FIG 27. (a) Photoacoustic voltage measured across $b\perp$ crystal 29.04.03.02 (passive part of DC5) illuminated with 4880 Å light. The active part of DC5 ($b\perp$ crystal 29.04.01.02) was operated in mode-locked fashion, under the conditions: applied D.C. electric field = 1.35 KV/cm, D.C. current density = 15 mA/cm^2, fundamental acoustic frequency = 18.2 MHz.

(b) Dember voltage as a function of light intensity at 5145 Å for $b\perp$ crystal 33.09.01.01 (part of DC2).

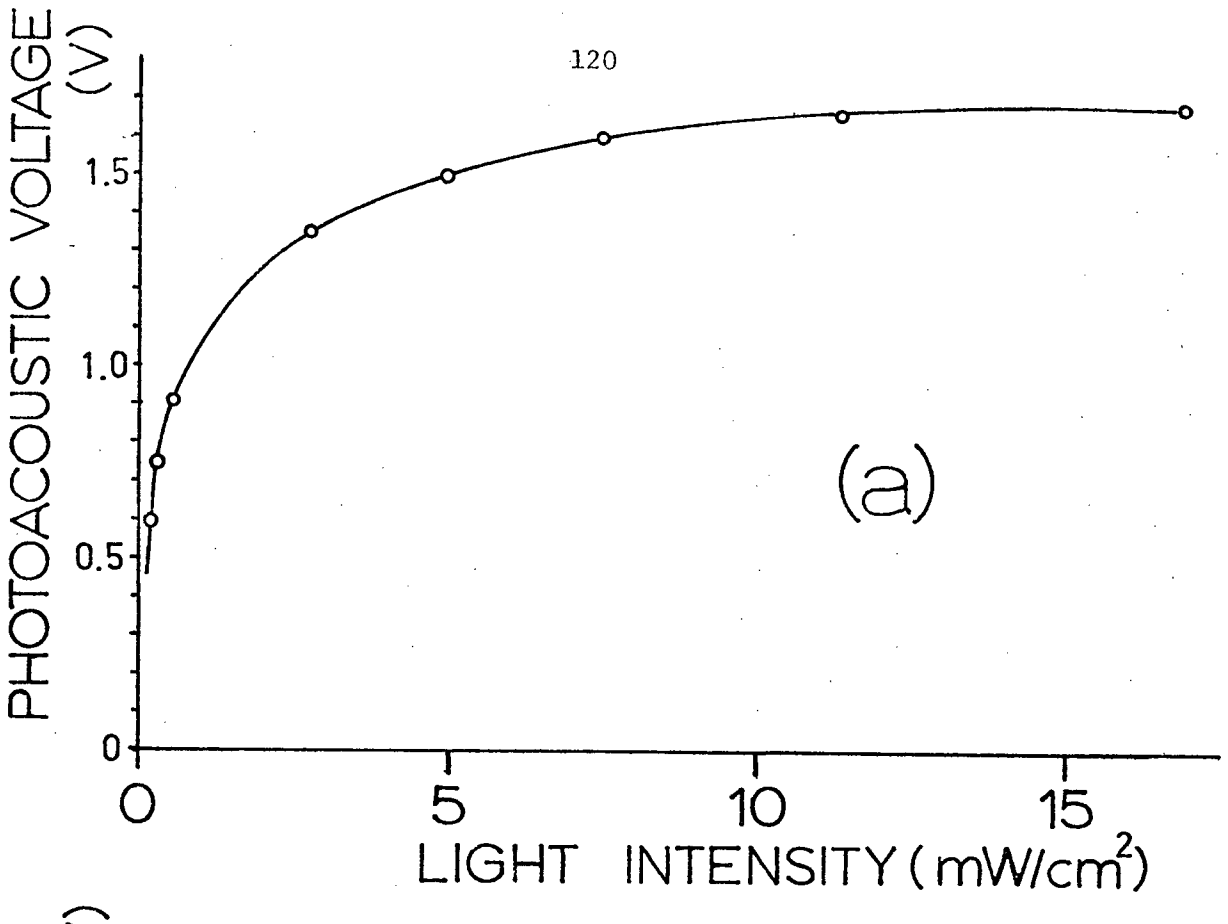
PHOTOACOUSTIC VOLTAGE (V)
1.5
1.0
0.5
0
(a)
0
5
10
15
LIGHT INTENSITY (mW/cm²)

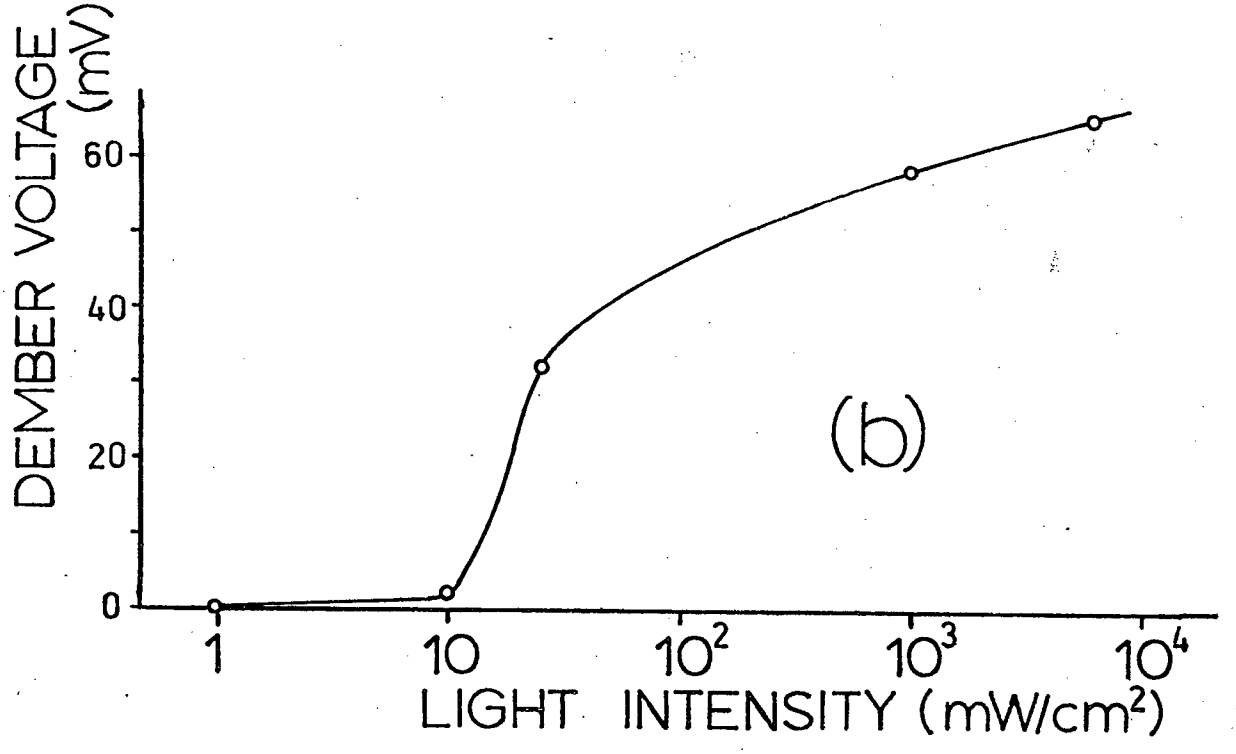
DEMBER VOLTAGE (mV)
60
40
20
0
(b)
1
10
10²
10³
10⁴
LIGHT INTENSITY (mW/cm²)

the Dember voltage for b$\perp$ crystal 33.09.01.01 is presented in FIG 27(b). The photoacoustic voltage was 3 to 4 orders of magnitude larger than the corresponding Dember voltage. For strongly absorbed light, the sign of the photoacoustic voltage was generally the same as the Dember voltage, i.e. the illuminated side of the passive cavity was positive with respect to the dark side. However, anomalous sign reversals could be observed at low strain amplitudes and for certain acoustic frequencies.

The spectral response of the photoacoustic voltage generally took the form illustrated in FIG 28(a), and displayed strong correllation with the response of the photoconductivity, FIG 28(b). This seems to indicate that the effect is proportional to the number of mobile carriers. When the active crystal was driven by an external oscillator, the photoacoustic voltage only appeared at multiples of the reciprocal of the round trip transit time of the composite cavity ($\simeq$ 1.28 MHz for DC5). This is illustrated in FIG 29. At higher conductivities (i.e. higher light intensities), the peak of the photoacoustic voltage shifted to lower frequencies [compare curves (1) and (2) in FIG 29], in agreement with the known conductivity tuning characteristics of CdS phonon masers (Burbank 1971). When the passive crystal was illuminated at ~ 5200 Å [the peak wavelength in FIG 28(a)] it was possible to achieve photoacoustic voltages of up to 15 volts.

3.2.1 Discussion

While the underlying physical mechanisms that produce the photoacoustic voltage are poorly understood, two qualitative models deserve mention:

FIG 28. (a) The spectral response of the photoacoustic voltage for $b_{\perp}$ crystal 29.04.03.02 (part of composite cavity DC5). The active part of DC5 ($b_{\perp}$ crystal 29.04.01.02) was driven at 7.55 MHz by an external oscillator.

(b) The spectral response of the photocurrent for $b_{\perp}$ crystal 29.04.03.02 under the same conditions of illumination as (a). The light was provided by a 200 W tungsten halogen lamp in series with a Heath monochromator.

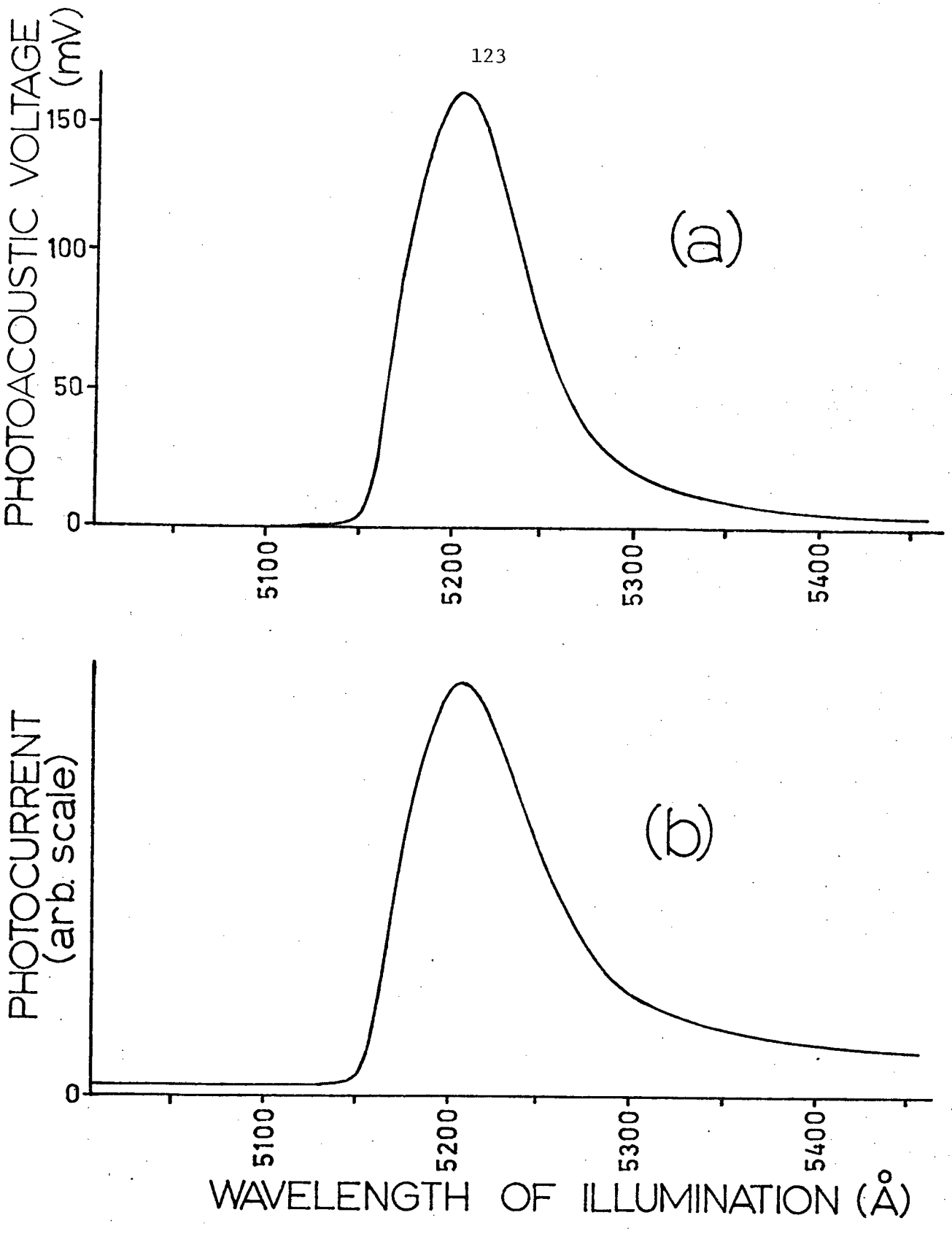
PHOTOACOUSTIC VOLTAGE (mV)
150
100
50
0
5100
5200
5300
5400
(a)
PHOTOCURRENT (arb. scale)
0
5100
5200
5300
5400
(b)
WAVELENGTH OF ILLUMINATION (Å)

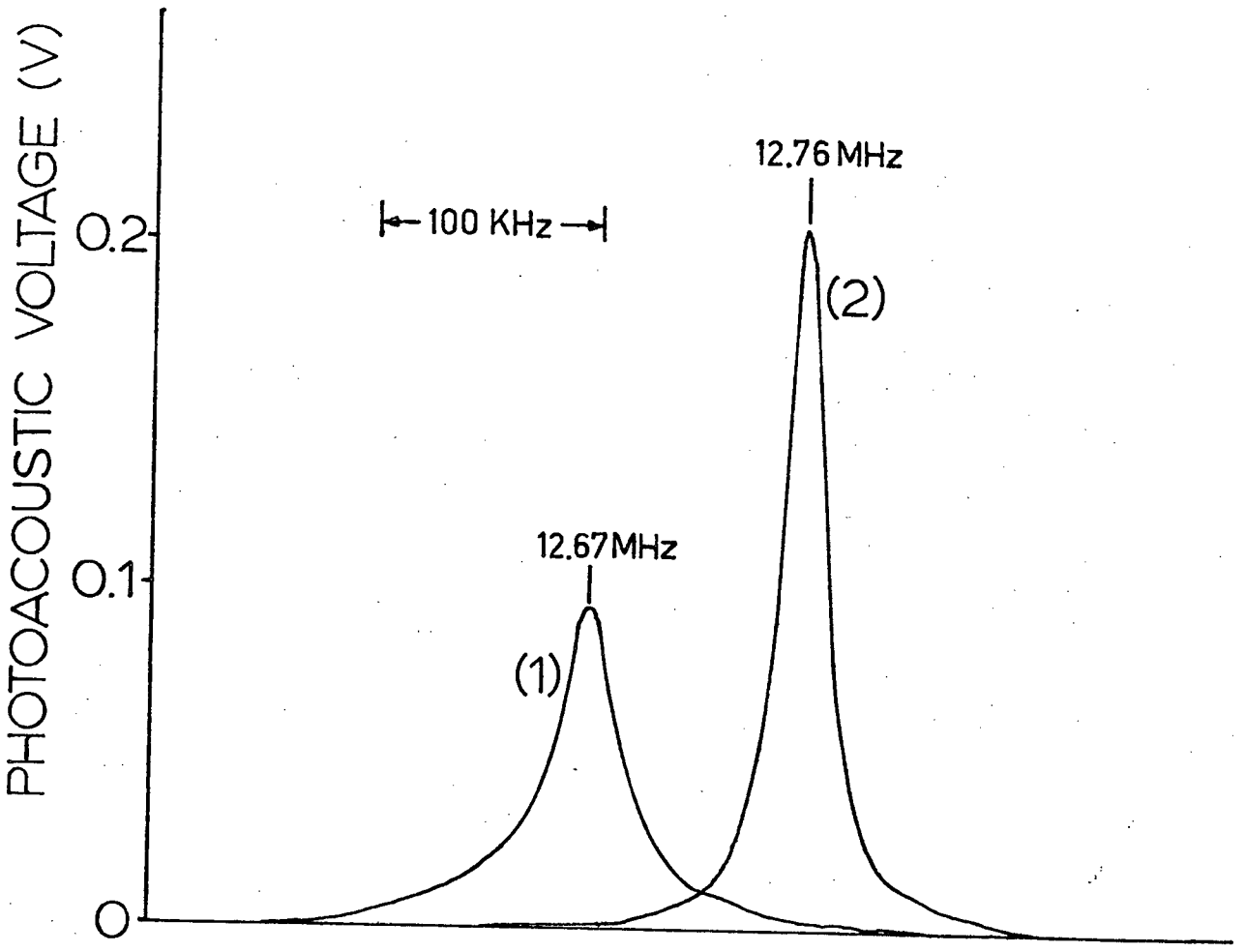

FIG. 29. Behavior of the photoacoustic voltage for DC5 as a function of the A.C. driving field applied to the active part of the composite cavity. Weakly absorbed (orange) light was used. The curves for two different conductivities (light intensities) are presented: $\sigma \simeq$ (1) $2 \times 10^{-4} (\Omega cm)^{-1}$ and (2) $4 \times 10^{-7} (\Omega cm)^{-1}$.

(1) "Mode-pulling"

The active modes in a phonon maser must satisfy the phase condition (Vrba and Haering 1973):

$$\Omega d\left(\frac{1}{v_{s+}} + \frac{1}{v_{s-}}\right) + 2\theta = 2n\pi \qquad (3.1)$$

where n is an integer, d is the cavity length, v_{s+} (v_{s-}) is the velocity of sound parallel (antiparallel) to the applied D.C. electric field. It is well known, from the linear theory of acoustic amplification in piezoelectric semiconductors (see, for example, McFee 1966), that the velocity of sound is a function of both conductivity and electric field. This forms the qualitative basis for the tuning characteristics of phonon masers, since varying the conductivity or electric field modifies the velocity of sound and requires the phonon maser to adjust its frequency in order to satisfy (3.1).

In the present case, illumination modifies the conductivity in the passive part of the composite cavity, thus changing the velocity of sound and spoiling the resonance condition, equation (3.1). It is conceivable that resonance can be restored, however, if the crystal establishes a D.C. electric field of the proper magnitude, thus returning the velocity of sound to its value before illumination. This highly qualitative model does not establish the sign of the photoacoustic voltage.

(2) Electron transport

In this model we assume that the piezoelectric potential wells associated with the acoustic wave act as "buckets" to transport optically created electrons from the illuminated surface to the dark surface. The resulting D.C. voltage should have the same sign as the corresponding Dember voltage. This model does not readily account for voltages of opposite sign to the Dember voltage, or for effects observed with weakly absorbed light.

It has not yet been possible to form a conclusive link between the experimental results and the preceeding models.

3.3 The A.C. Electric Field Induced Photovoltaic Effect

A second D.C. voltage, requiring the simultaneous presence of light and an externally applied A.C. electric field, has been discovered in CdS crystals. The experimental configuration for measurement of this photovoltage is shown in FIG 30. The capacitor C_1 in FIG 30 served to D.C. decouple the external oscillator from the rest of the circuit. The combination of L and C_2 formed a low pass filter to protect the D.C. voltmeter from the A.C. driving voltage. The samples used in these experiments were polished phonon maser crystals and hence had In diffused surfaces (see APPENDIX B).

The spectral response of the D.C. voltage is shown in FIG 31. Similar to the photoacoustic voltage, it contained one dominant peak, shifted ~ 100 Å to shorter wavelengths with respect to the peak in FIG 28(a). Also, the sign of the voltage generally reversed for wavelengths $\gtrsim$ 5250 Å. As a function of light intensity, the D.C. voltage

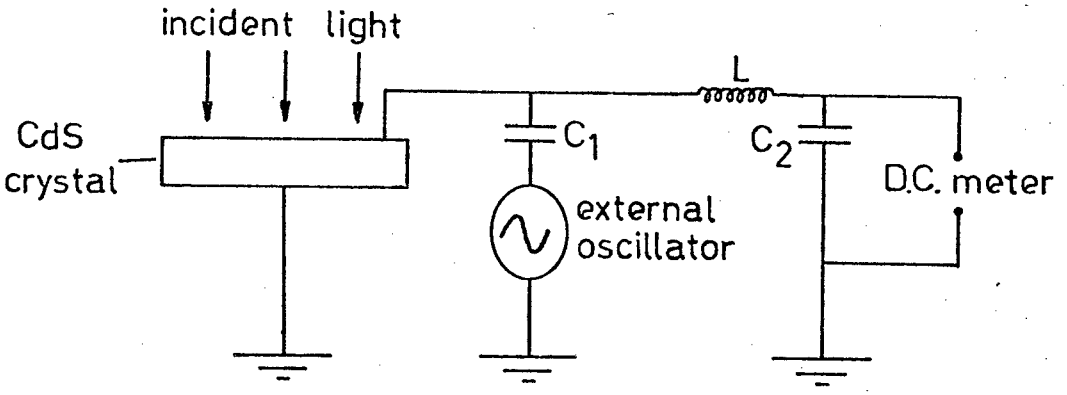

FIG 30. Experimental configuration for measuring the A.C. electric field induced photovoltage.

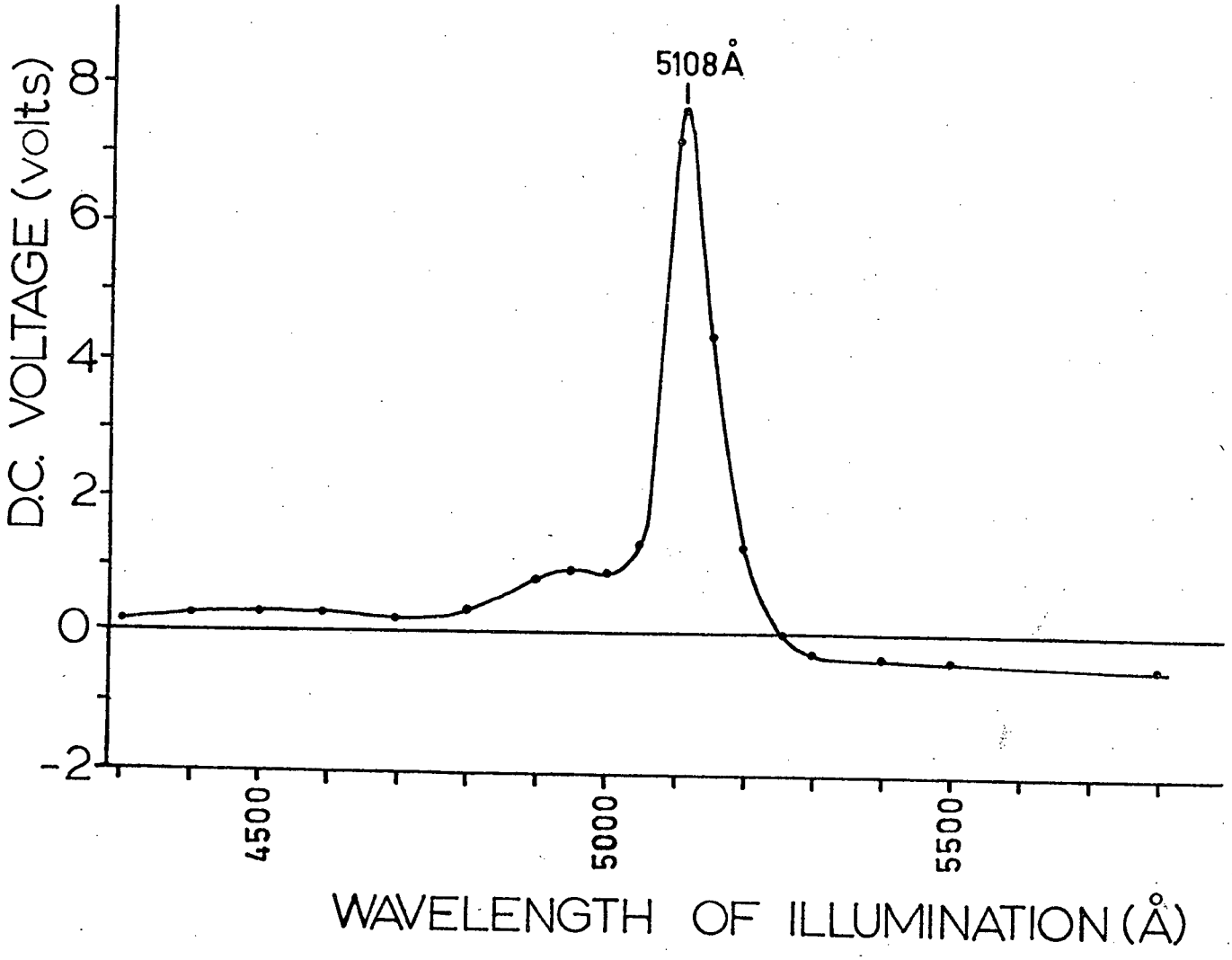

FIG 31. Spectral response of the D.C. photovoltage for b$\perp$ crystal 29.04.01.02 (part of DC5). The intensity of illumination was ~ 0.5 mW/cm^2. The light was provided by a 200 W tungsten halogen lamp in series with a Jarrell Ash monochrometer.

saturated very quickly, in a manner similar to FIG 27. It displayed a quadratic dependence on the amplitude of the A.C. driving voltage, as illustrated in FIG 32(a), and as the driving frequency was increased the D.C. voltage fell off quickly, as is shown in FIG 32(b).

The D.C. photovoltage appeared at all frequencies, indicating that its presence was probably not related to the resonant acoustic structure of the crystal. At frequencies corresponding to acoustic resonances of the crystal, the photoacoustic voltage was also present. In FIG 33(a) the D.C. photovoltage is shown as a function of frequency for illumination with small amounts of weakly absorbed light. As the light level (and hence the conductivity) was reduced, the photoacoustic voltage became dominant [compare curve (3) in FIG 33(a) with curve (2) in FIG 29]. For higher light levels, and particularly in the case of strongly absorbed light, the nonresonant photovoltage dominated, as illustrated in FIG 33(b).

To further investigate the behavior of this photovoltage, pulse measurements were performed at temperatures from 5°K to 300°K. The crystals used were mounted in a variable temperature LHe dewar, and were illuminated with white light provided by a 100 W Hg arc lamp. When the light was shut off, by means of a mechanical shutter, an R.F. pulse, whose width and delay time with respect to the end of the optical signal could be varied, was applied to the crystal. The R.F. pulses were obtained from a Hewlett Packard model 3200B VHF oscillator, which was pulse modulated by a Hewlett Packard model 214A pulse generator.

FIG 32. (a) The D.C. photovoltage as a function of the amplitude of the applied A.C. voltage (12 MHz) for $b\perp$ crystal 29.04.01.02 (part of DC5). The illumination was at 5100 Å, with an intensity of about 0.5 mW/cm^2. The solid curve through the experimental points corresponds to $V_{D.C.} = (2.78 \times 10^{-2})V^2_{A.C.}$.
(b) The D.C. photovoltage as a function of driving frequency at constant amplitude for $b\perp$ crystal 29.04.03.02 (part of DC5), illuminated with a small amount of weakly absorbed (orange) light.

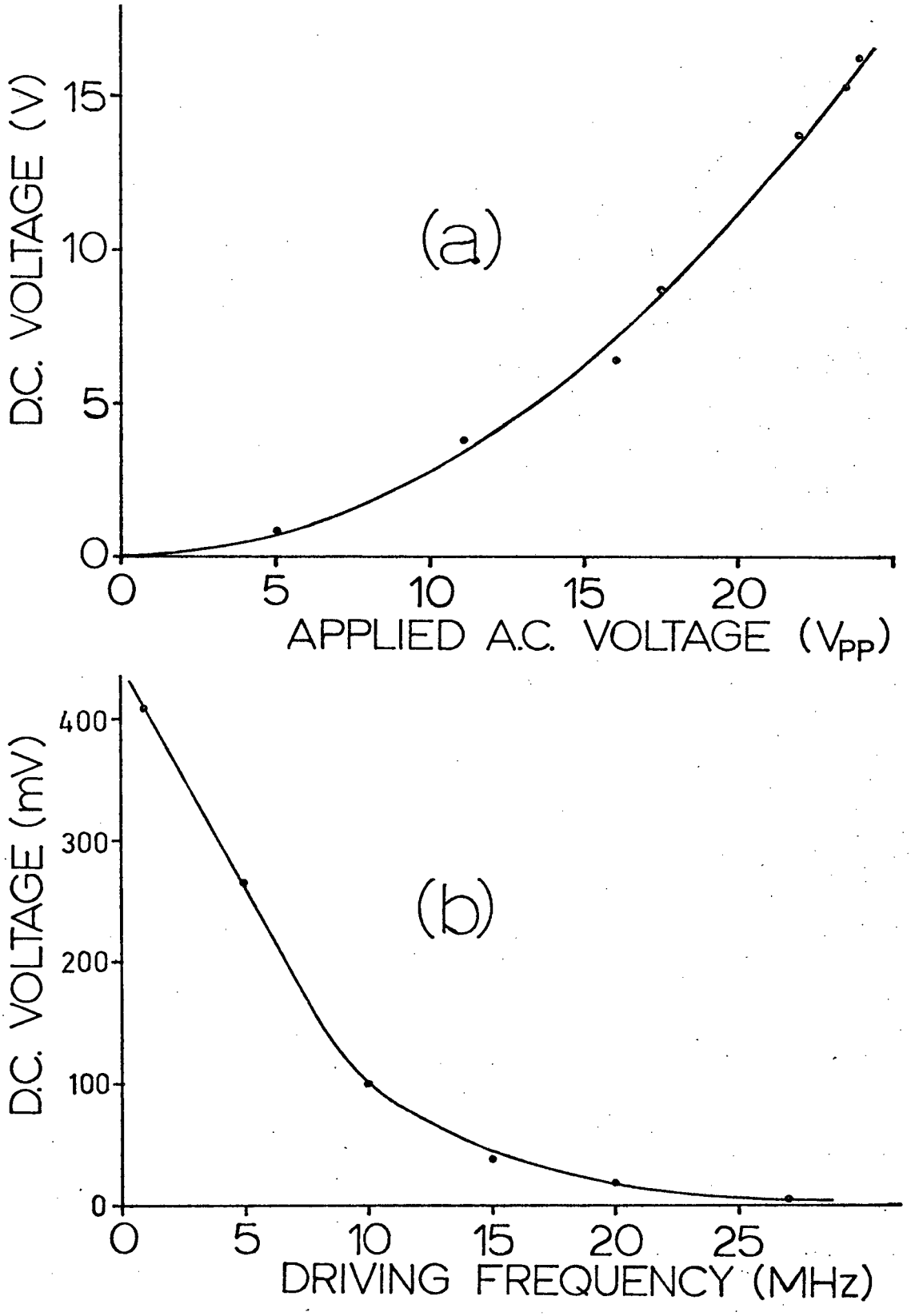
D.C. VOLTAGE (V)
15
10
5
0
(a)
0
5
10
15
20
APPLIED A.C. VOLTAGE (V_{PP})
D.C. VOLTAGE (mV)
400
300
200
100
0
(b)
0
5
10
15
20
25
DRIVING FREQUENCY (MHz)

FIG 33. (a) The D.C. photovoltage for $b\perp$ crystal 29.04.01.02 (part of DC5) as a function of frequency, for low levels of weakly absorbed (orange) light. Curves for three different conductivities (light levels) are presented: $\sigma \simeq$ (1) $1.4 \times 10^{-4}(\Omega cm)^{-1}$, (2) $5 \times 10^{-5}(\Omega cm)^{-1}$ and (3) $4 \times 10^{-7}(\Omega cm)^{-1}$.

(b) The D.C. photovoltage for $b\perp$ crystal 29.04.01.02 as a function of frequency (the driving amplitude was not constant). The crystal was illuminated with about 0.5 mW/cm^2 at 5100 Å. The separation of the small negative peaks is equal to the reciprocal of the round trip transit time of DC5 ($\simeq$ 1.28 MHz).

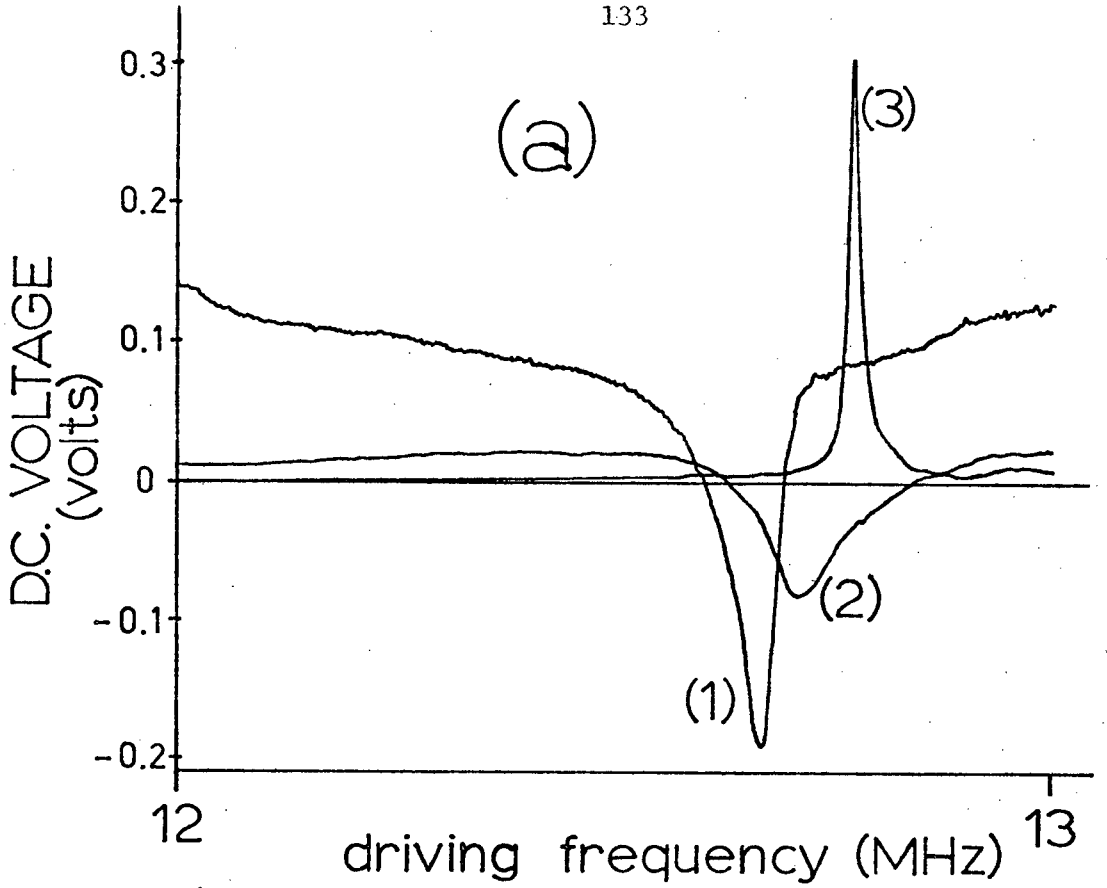
(a)
0.3
0.2
0.1
0
-0.1
-0.2
D.C. VOLTAGE (volts)
(1)
(2)
(3)
12
13
driving frequency (MHz)

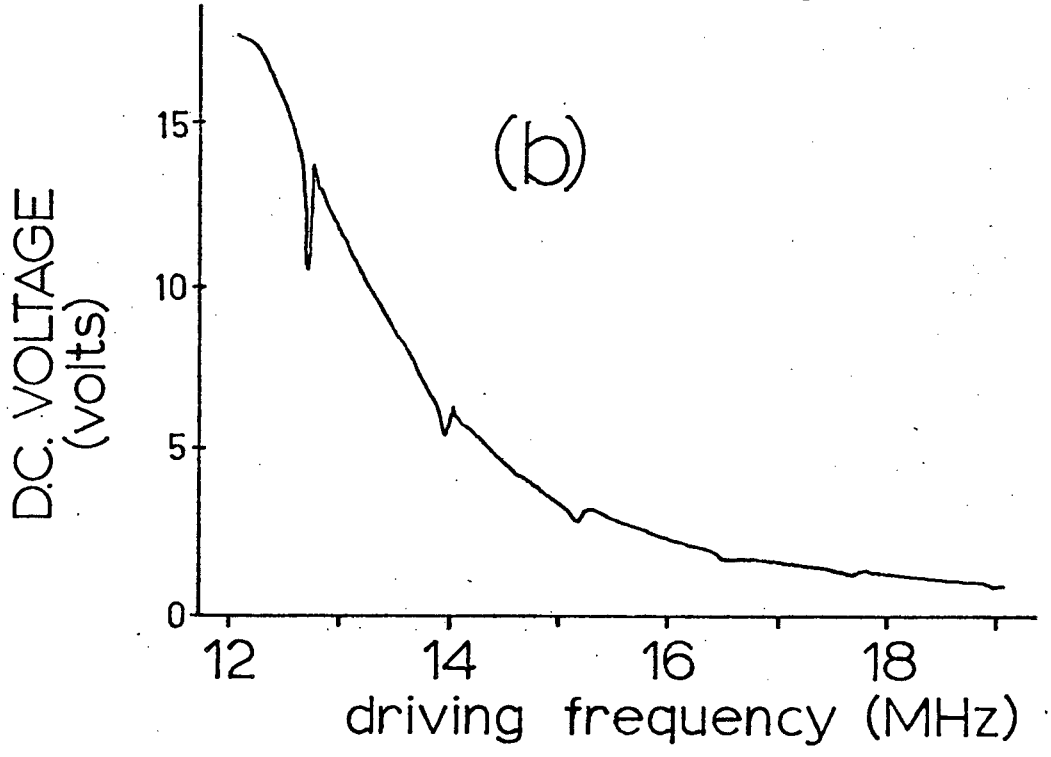
(b)
15
10
5
0
D.C. VOLTAGE (volts)
12
14
16
18
driving frequency (MHz)

The trailing edge of the optical signal and the form of the R.F. pulse are shown in FIG 34(a). For a given set of conditions, it was found that both the lifetime and amplitude of the pulse generated voltages increased by a factor of 2-3 in cooling the samples from room temperature to 100°K. At temperatures much below 70°K, however, the signals rapidly became weaker, and were almost nonexistent at 5°K. The voltage signals generated at ~ 80°K by R.F. pulses of different delay times are shown in FIG 34(b). If the time for generation t_g was measured from the end of the optical signal [see lower traces in FIG 34(a), (c), (d)] the amplitude of the generated voltage decayed roughly as $e^{-t_g/\tau}$, where τ ~ 10ms. The decay time of the voltage dependended strongly on the level of illumination. As is shown in FIG 34(c) and (d), the amplitude of the generated voltage increased, while the decay time of the voltage decreased, with increasing light intensity.

3.3.1 Discussion

Even less is understood about the physical processes involved in this photovoltage than in the case of the photoacoustic voltage. Its dominant characteristics, however, do not appear to be strongly correlated with the acousto-electric properties of the CdS samples. The characteristic decay time illustrated in FIG 34(b) is approximately the same size as the electron lifetime, as determined using A.C. photoconductivity measurements. This suggests that the photovoltage is associated with mobile rather than trapped charge. The behavior illustrated in FIG 34(c) and (d) is consistent with the crystal behaving as a battery with a

FIG 34. Some results of the pulse measurements:

(a) lower trace shows trailing edge of (negative) signal produced by sample illumination; upper trace shows the R.F. pulse (11 MHz), in this case having a length of 200 μsec and a delay of 10 msec with respect to the end of the optical signal, (b) voltages produced by R.F. pulses of 1 msec width, applied at various delay times to c$\perp$ crystal 33.05.01.01 (T ≈ 80°K), and voltages produced in c$\perp$ crystal 33.04.02.00 (upper traces) by 10 msec delayed R.F. pulses (width 200 μsec) at T ≈ 100°K for (c) weak illumination and (d) intensity of illumination increased by a factor of 10 with respect to (c).

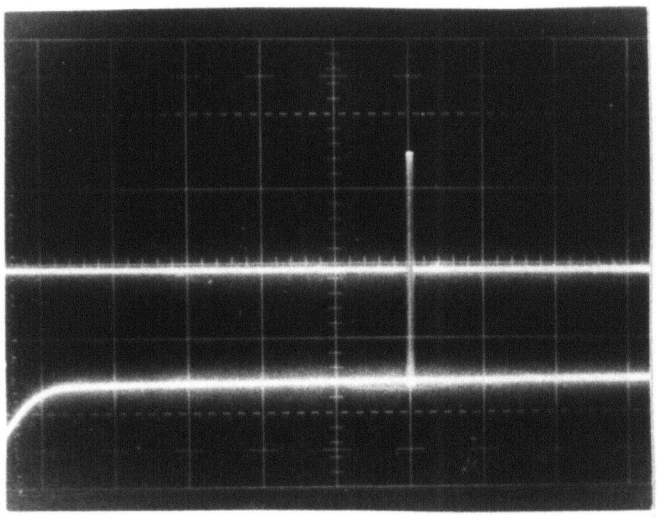

Horizontal scale: 2ms/div.

Vertical scale: Upper trace - 10V/div.
Lower trace - 0.5V/div.

(a)

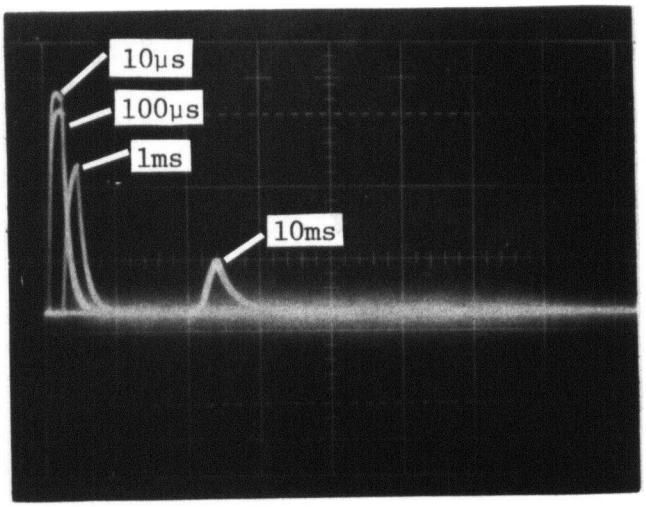

Horizontal scale: 5ms/div.

Vertical scale: 0.5V/div.

(b)

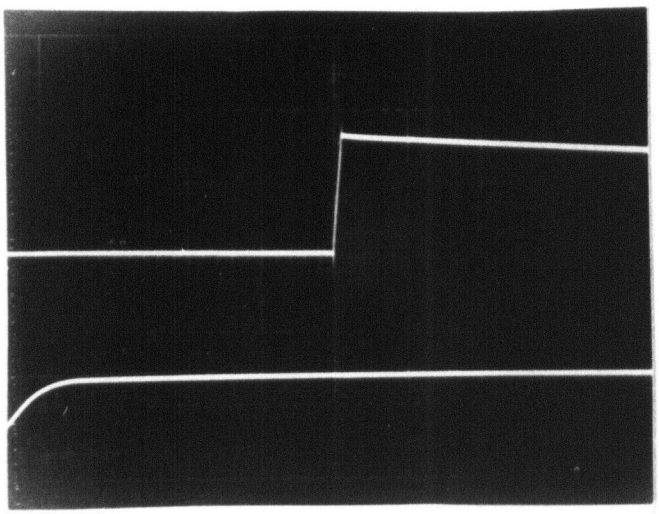

Horizontal scale: 2ms/div.

Vertical scale: Upper trace - 20mV/div.
Lower trace - 0.5V/div.

(c)

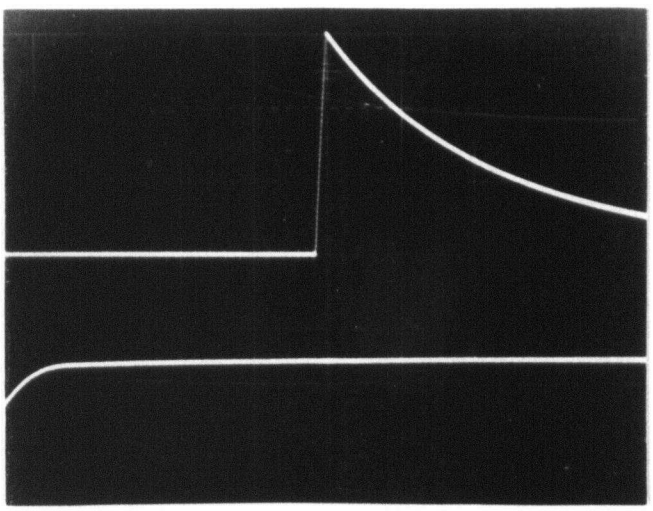

Horizontal scale: 2ms/div.

Vertical scale: Upper trace - 0.2V/div.
Lower trace - 0.5V/div.

(d)

variable internal impedance. At high light levels, the conductivity of the crystal is larger. Hence its internal impedance is smaller and it "discharges" more quickly than for low light levels.

3.4 Conclusions and Summary of Contributions

Two new photovoltaic-type effects have been discovered in CdS. The voltages incurred are remarkable for their magnitude: photoacoustic voltages of about 15 V and A.C. electric field induced photovoltages of about 25 V were achieved with very small light levels ($\lesssim 1$ mW/cm^2). These voltages are several orders of magnitude larger than the normal photovoltages encountered at similar light levels in CdS. At this time, the experimental results are not understood and more work is warranted in this area.

APPENDIX A

ACOUSTIC STANDING WAVE PATTERN FOR MODE-LOCKED OPERATION

In practice, the strain profiles of the phonon maser were observed by acoustic coupling to a passive cavity of fused quartz. This allowed the strain profile to be optically probed in the passive cavity, without disturbing the phonon maser (refer to section 1.4 of CHAPTER 1). The acoustic strain at a point x in the passive cavity, represented in FIG A1, may be written as a superposition of an incident waveform F_i, coupled from the phonon maser, and a waveform F_r, which

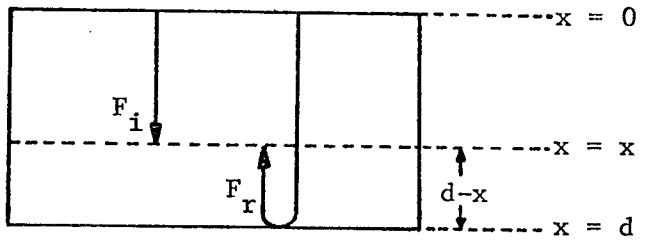

FIG A1.

has been spatially reflected from the surface x=d of the passive cavity. We make the assumption that in steady state all waves moving in the same direction maintain the same phase at any plane x = constant, for all times (i.e. no anomalous effect due to multiple reflections).

Then, to obtain the correct relative phase for F_i and F_r, it may be inferred from FIG A1 that it is necessary to set $x \rightarrow 2d-x$ for F_r.

Assuming periodic form for the acoustic strain, F_i may be written in Fourier series form:

$$F_i(x,t) = \sum_{n=1}^{\infty} \left[a_n \cos[n(Kx-\Omega t)] + b_n \sin[n(Kx-\Omega t)] \right] \tag{A1}$$

where a_n, b_n are the usual Fourier coefficients and K, Ω are the wave number and angular frequency of the acoustic fundamental. (A constant term has been omitted in (A1) from the general form of the Fourier series, since no D.C. strains are associated with the acoustic waves.) Assuming no losses upon reflection, it is apparent from the preceeding discussion that

$$F_r(x,t) = F_i(2d-x,t) = \sum_{n=1}^{\infty} \left[a_n \cos[nK(2d-x)-n\Omega t] + b_n \sin[nK(2d-x)-n\Omega t] \right]$$

$$= \sum_{n=1}^{\infty} \Big[a_n \cos(2nKd)\cos[n(Kx+\Omega t)] + a_n \sin(2nKd)\sin[n(Kx+\Omega t)]$$

$$+ b_n \sin(2nKd)\cos[n(Kx+\Omega t)] - b_n \cos(2nKd)\sin[n(Kx+\Omega t)] \Big]$$

$$= \sum_{n=1}^{\infty} \left[c_n \cos[n(Kx+\Omega t)] + d_n \sin[n(Kx+\Omega t)] \right] \tag{A2}$$

where

$$c_n = a_n \cos(2nKd) + b_n \sin(2nKd)$$

$$d_n = a_n \sin(2nKd) - b_n \cos(2nKd) \tag{A3}$$

We now introduce phases δ_n in equation (A1) such that

$$\begin{aligned} a_n &= S_n \sin\delta_n \\ b_n &= S_n \cos\delta_n \end{aligned} \tag{A4}$$

where $$\tan\delta_n = a_n/b_n \tag{A5}$$

and $$S_n^2 = a_n^2 + b_n^2 \tag{A6}$$

Equation (A1) now takes the form:

$$F_i(x,t) = \sum_{n=1}^{\infty} S_n \sin[n(Kx-\Omega t) + \delta_n] \tag{A7}$$

In a similar manner, phases β_n may be defined in equation (A2) such that:

$$\begin{aligned} c_n &= C_n \sin\beta_n \\ d_n &= C_n \cos\beta_n \end{aligned} \tag{A8}$$

where $$\tan\beta_n = c_n/d_n \tag{A9}$$

Making use of equation (A3) one obtains:

$\therefore$

$$C_n^2 = c_n^2 + d_n^2 = [a_n\cos(2nKd) + b_n\sin(2nKd)]^2 + [a_n\sin(2nKd) - b_n\cos(2nKd)]^2$$

$$= a_n^2 + b_n^2 \equiv S_n^2 \qquad \text{from equation (A6)}$$

Hence $$C_n = \pm S_n \tag{A10}$$

Using equation (A3) in equation (A9):

$$\tan\beta_n = \frac{a_n\cos(2nKd) + b_n\sin(2nKd)}{a_n\sin(2nKd) - b_n\cos(2nKd)}$$

$$= \frac{\tan\delta_n + \tan(2nKd)}{\tan\delta_n\tan(2nKd) - 1} \qquad \text{using equation (A5)}$$

$$= -\tan(\delta_n + 2nKd)$$

Hence $$\beta_n = -(\delta_n + 2nKd) \tag{A11}$$

With (A10) and (A11), equation (A2) now takes the form:

$$F_r(x,t) = \pm \sum_{n=1}^{\infty} S_n\sin[nK(x-2d) + n\Omega t - \delta_n] \tag{A12}$$

From equations (A7) and (A12), the total acoustic strain may be written:

$$F(x,t) = \sum_{n=1}^{\infty} S_n\left\{\sin[n(Kx-\Omega t)+\delta_n] \pm \sin[nK(x-2d)+n\Omega t-\delta_n]\right\} \tag{A13}$$

The boundary at x=d may be considered a free surface. Thus, for the one-dimensional system considered, both the stress and strain must vanish at x=d. This can be satisfied by F(x,t) only if the +sign is chosen in equation (A13). Equation (A13) may then be written in the alternate form:

$$F(x,t) = 2\sum_{n=1}^{\infty} S_n \sin[nK(x-d)]\cos(nKd-n\Omega t+\delta_n) \qquad (A14)$$

The boundary at x=0 is not free since the passive cavity is bonded to the phonon maser at this point. The value of the strain at x=0 is determined by the parameters K,Ω,δ_n and d in equation (A14). The acoustic modes participating in mode-locked operation may be considered as being harmonically related. Thus, for this case, the upper limit of the summation in equations (A13) and (A14) will equal the number of active acoustic modes N.

APPENDIX B

PHYSICAL PROPERTIES

Material Parameters For CdS:

Density[1] (10^3 Kg/cm^3) $\rho = 4.820$

Elastic stiffness constants[1] (10^{10} newton/m^2)

$c_{11} = 9.07$, $c_{12} = 5.81$, $c_{13} = 5.10$,

$c_{33} = 9.38$, $c_{44} = 1.504$

Piezoelectric stress constants[1] (coulomb/m^2)

$e_{15} = -0.21$, $e_{31} = -0.24$, $e_{33} = 0.44$

Dielectric constants (constant strain)[1]

$\kappa_1 = 9.02$, $\kappa_2 = 9.02$, $\kappa_3 = 9.53$

Refractive indices[2]

$n_o = 2.506$, $n_e = 2.491$

Photoelastic constants[3,4]

$p_{11} = 0.11$, $p_{12} = 0.051$, $p_{13} = 0.072$,

$p_{31} = 0.050$, $p_{33} = 0.13$, $p_{44} = 0.054$

Electro-optic constants[5,6] (10^{-12} m/V)

$$z_{42} = 3.7,\ z_c = z_{33} - \left(\frac{n_o}{n_e}\right)^3 z_{13} = 5.5,\ z_{33} \simeq \frac{2z_c}{3}$$

---

[1] Auld (1973)

[2] Neuberger (1969)

[3] Dixon (1967)

[4] Maloney and Carleton (1967)

[5] Gainon (1964)

[6] Kaminow (1968)

Material Parameters For Fused Quartz:

Density[3] (10^3 Kg/m^3) $\rho = 2.2$

Refractive index[3] $n_o = 1.46$

Photoelastic constant[3] $p_{44} = 0.075$

Shear acoustic velocity[3] (10^3 m/sec) $v_s = 3.76$

Longitudinal acoustic velocity[3] (10^3 m/sec) $v_\ell = 5.95$

The techniques used for fabrication of phonon masers have been detailed by Burbank (1971). The CdS crystals were oriented by means of X-ray diffraction to an accuracy of ±0.5°. For typical sample dimensions, a flatness of from 1/5 to 1/10 of an optical wavelength could be achieved for the polished surfaces. Transparent electrical contacts were provided by means of In diffusion. Techniques similar to those used for phonon masers were applied to fabricate acoustic cavities from fused quartz, sapphire, and Barium Fluoride. Composite acoustic cavities were bonded together using the technique outlined in APPENDIX C. The physical data for the samples mentioned in the main text of the thesis are listed in TABLE B1.

TABLE B1 - Physical Data For Acoustic Cavities

Acoustic Cavity†		Dimensions (mm)	Surface Finish		
			polished	wire saw	In diffused
DC1	24.01.02.04	d = 1.193, b-axis	X		X
		ℓ = 2.166		X	
		w = 1.999		X	
	FQ1 (fused quartz)	d = 3.306	X		
		ℓ = 10.781		X	
		w = 10.760	X		
DC2*	33.09.01.01	d = 1.090, b-axis	X		X
		ℓ = 3.541		X	
		w = 2.775		X	
	FQ2 (fused quartz)	d = 4.414	X		
		ℓ = 7.844	X		
		w = 7.778	X		
DC3	24.07.10.01	d = 0.830, b-axis	X		X
		ℓ = 2.228		X	
		w = 2.022		X	
	S1 (sapphire)	d = 3.351, x_1-axis	X		
		ℓ = 10.949		X	
		w = 7.087	X		
DC4	27.02.04.02	d = 0.744, c-axis	X		X
		ℓ = 3.252	X		
		w = 2.288	X		
	27.01.01.02	d = 0.819, c-axis	X		X
		ℓ = 3.579	X		
		w = 3.207		X	
DC5	29.04.01.02	d = 0.318, b-axis	X		X
		ℓ = 3.210		X	
		w = 1.976		X	
	29.04.03.02	d = 0.379, b-axis	X		X
		ℓ = 4.731		X	
		w = 4.132		X	

†Unless otherwise indicated, the acoustic cavities are CdS crystals.

*b⊥ crystal 33.08.06.00 was later bonded to DC2 to form a triple cavity.

Acoustic Cavity†	Dimensions (mm)	Surface Finish		
		polished	wire saw	In diffused
24.06.06.01	d = 1.265, c-axis	X		X
	ℓ = 7.225	X		
	w = 2.170	X		
33.04.02.00	d = 0.376, c-axis	X		X
	ℓ = 3.111		X	
	w = 1.838		X	
33.05.01.01	d = 0.854, c-axis	X		X
	ℓ = 4.037		X	
	w = 2.289		X	

APPENDIX C

ACOUSTIC BONDS

To provide high quality acoustic bonds between a CdS phonon maser and a second acoustic cavity (buffer), a cold welding procedure similar to that of Sittig and Cook (1968) was employed (Hughes 1974). The two samples to be bonded were first thoroughly cleaned. This step was crucial since the evaporated layers that formed the bond were only ~ 3000 Å thick. Following thorough ultrasonic washes in acetone and subsequent rinsing in distilled water, a final cleaning was performed in a laminar flow box, using lens tissues moistened with ether. An optical flat (also carefully cleaned) was used to check for the presence of dust particles using interference techniques. Systematic wiping of the surfaces was continued until no interference fringes could be observed, indicating that all dust particles $\gtrsim$ 1000 Å had been removed.

Following cleaning, the samples were mounted on a press in an evaporator. When a vacuum of about 3×10^{-6} torr was achieved, a thin layer (~ 100 Å) of Cr followed by a 1000 Å layer of Au were evaporated on the buffer, to form a durable electrical contact. 2000 Å of In was then laid down on the phonon maser, thus making electrical contact with its diffused In surface. Following evaporation, and while still under vacuum, the evaporated surfaces of the two samples were pressed together

with a pressure ≈ 200 Kg/cm^2. After allowing several hours for the bond to form, the composite cavity could be removed from the evaporator. In the region of the bond the Au layer took on a silver color, indicating that alloying had taken place with the In layer. Using this technique, CdS phonon masers were successfully bonded to buffers of Al_2O_3, fused SiO_2, BaF_2 and CdS.

REFERENCES

Abramowitz, M. and Segun, I.A., 1968. Handbook of Mathematical Functions. Dover, N.Y.

Auld, B.A., 1973. Acoustic Fields and Waves in Solids. Wiley.

Bhatia, A.B. and Noble, W.J., 1953. Proc. Roy. Soc. 220, ser. A, 356.

Booth, A.H., 1954. Can. J. Chem. 32, 214.

Born, M. and Wolf, E., 1959. Principles of Optics. Pergamon Press, N.Y.

Burbank, M.B., 1971. Phonon Maser Action in CdS. Ph.D. thesis, S.F.U.

Butcher, P.N., 1971. J. Phys. C: Solid St. Phys. 4, 36.

Butcher, P.N. and Ogg, N.R., 1968. J. Phys. D: Appl. Phys. 1, 1271.

———————————— 1969. J. Phys. D: Appl. Phys. 2, 333.

———————————— 1970. J. Phys. C: Solid St. Phys. 3, 706.

Chaban, A.A., 1972. JETP Lett. 15, 74.

———————— 1974. Sov. Phys. Solid State 15, 2405.

———————— 1975. Sov. Phys. Solid State 17, 650.

Cutler, C.C., 1955. Proc. I.R.E. 43, 140.

Davis, H.F., 1968. Fourier Series and Orthogonal Functions. Allyn and Bacon, Inc.

Demaria, A.J., Glenn, W.H., Brienza, M.J. and Mack, M.E., 1969. Proc. IEEE 57, 2.

Dember, H., 1931. Physik. Zeits. 32, 554.

Dixon, R.W., 1967. J. Appl. Phys. 38, 5149.

Extermann, R. and Wannier, G., 1936. Helv. Phys. Acta. 9, 520.

Gainon, J.A., 1964. J. Opt. Soc. Am. 54, 270.

Garlick, G.F.J. and Gibson, A.F., 1948. Proc. Roy. Soc. A60, 574.

Gay, R.K.L. and Hartnagel, H.L., 1969. J. Phys. D: Appl. Phys. 2, 1589.

———————————— 1970. J. Phys. D: Appl. Phys. 3, 736.

Goodman, J.W., 1968. Introduction to Fourier Optics. McGraw-Hill.

Grossweiner, L.J., 1953, J. Appl. Phys. 24, 1306.

Gulayev, Y.V., 1970. IEEE Trans. Sonics Ultrason. SU17, 111.

———————— 1970. Sov. Phys. Solid St. 12, 328.

Gurevich, V.L., 1969. Sov. Phys. Semicond. 2, 1299.

Haering, R.R., 1959. Can. J. Phys. 37, 1374.

Haydl, W.H. and Quate, C.F., 1966. Phys. Lett. 20, 463.

Hudson, A.R. and White, D.L., 1962. J. Appl. Phys. 33, 40.

Hughes, R.C., 1974. Mode Structure in Acoustic Cavities. Ph.D. thesis, S.F.U.

Hughes, R.C. and Haering, R.R., 1976. J. Acoust. Soc. Am. 59, 452.

Kaminow, I.P., 1968. IEEE J. Quan. Elec. QE4, 23.

Klein, W.R., Cook, W.D. and Mayer, W.G., 1965. Acustica 15, 57.

Klein, W.R. and Cook, W.D., 1967. IEEE Trans. Sonics Ultrason. SU14, 123.

Maerfeld, C. and Tournois, P., 1975. Appl. Phys. Lett. 26, 661.

Maines, J.D., 1966. Appl. Phys. Lett. 8, 67.

Maines, J.D. and Paige, E.G.S., 1969. J. Phys. C 2, 175.

———————————— 1970. Solid State Commun. 8, 421.

Maloney, W.T. and Carleton, H.R., 1967. IEEE Trans. Sonics Ultrason. SU14, 135.

Melcher, R.L. and Shiren, N.S., 1975. Phys. Rev. Lett. 34, 731.

McFee, J.H., 1966. Physical Acoustics. Ed. by W.P. Mason. Academic Press N.Y. Vol. IV, part A.

Neuberger, M., 1969. II-VI Semiconducting Compounds Data Tables, Electronic Properties Information Center, Hughes Aircraft Co. U.S.A.

Nye, J.F., 1964. Physical Properties of Crystals. Oxford: Clavendon.

Pankove, J.I., 1971. Optical Processes in Semiconductors. Prentice-Hall, chap. 14.

Raman, C.V. and Nath, N.S.N., 1935a. Proc. Ind. Acad. Sci. A2, 406.

———————————— 1935b. Proc. Ind. Acad. Sci. A2, 413.

———————————— 1936a. Proc. Ind. Acad. Sci. A3, 75.

———————————— 1936b. Proc. Ind. Acad. Sci. A3, 119.

Sharma, A.K. and Wilson, M.G.F., 1970. Proc. IEEE 117, 2216.

Shiren, N.S., 1975. IEEE Trans. Sonics Ultrason. SU22, 229.

Shiren, N.S., Melcher, R.L., Garrod, D.K. and Kazyaka, T.G., 1973. Phys. Rev. Lett. 31, 819.

Sittig, E.K. and Cook, H.D., 1968. Proc. IEEE L56, 1375.

Smeaton, M.D., Hughes, R.C., Vrba, J. and Haering, R.R., 1976. Solid State Commun, 18, 465.

Smeaton, M.D. and Haering, R.R., 1976a. Solid State Commun. (in press).

———————————— 1976b. Solid State Commun. (in press).

Smith, R.W., 1963. Phys. Rev. Lett. 9, 87.

Tien, P.K., 1968. Phys. Rev. 171, 970.

Vrba, J. and Haering, R.R., 1973. J. Appl. Phys. 44, 5213.

———————————— 1973. Can. J. Phys. 51, 1341.

———————————— 1974. Can. J. Phys. 52, 1233.

White, D.L., 1962. J. Appl. Phys. 33, 2547.

Willard, G.W., 1949. J. Acoust. Soc. Am. 21, 101.

Williams, R., 1962. J. Phys. Chem. Solids 23, 1057.

Wonneberger, W., 1970. Phys. Stat. Solidi 40, 129.

Yushin, N.K., Lemanov, V.V., and Agishev, B.A., 1975. Sov. Phys. Solid State 16, 1812.

BIBLIOGRAPHY - DIFFRACTION OF LIGHT BY ULTRASONIC WAVES

General Theory:

Bhatia, A.B. and Noble, W.J., 1953. Proc. Roy. Soc. 220, ser. A, 356.

Klein, W.R., Cook, W.D. and Mayer, W.G., 1965. Acustica 15, 57.

Quate, C.F., Wilkinson, C.D.W. and Winslow, D.K., 1965. Proc. IEEE 53, 1604.

Raman - Nath Diffraction:

Nath, N.S.N. and Mueller, H., 1938. Nature 141, 37.

Raman, C.V. and Nath, N.S.N., 1935. Proc. Ind. Acad. Sci. A2, 406

———————— 1935. Proc. Ind. Acad. Sci. A2, 413.

———————— 1936. Proc. Ind. Acad. Sci. A3, 75.

———————— 1936. Proc. Ind. Acad. Sci. A3, 119.

Vrba, J. and Haering, R.R., 1973. Can. J. Phys. 51, 1341.

———————— 1973. Can. J. Phys. 51, 1359.

———————— 1974. Can. J. Phys. 52, 1233.

———————— 1974. Can. J. Phys. 52, 1239.

Modifications to Raman - Nath Theory:

Hargrove, L.E., 1967. IEEE trans. Sonics Ultrason. SU14, 33.

Klein, W.R. and Hiedemann, E.A., 1963. Physica 29, 981.

Mertens, R., 1958. Ind. Acad. Sci. A48, 88.

Miller, R.B. and Hiedemann, E.A., 1958. J. Acoust. Soc. Am. 30, 1042.

Plancke-Schuyten, G., Mertens, R. and Leroy, O., 1972. Physica 61, 299.

Comparison of Raman - Nath and Bragg Diffraction:

Klein, W.R. and Cook, B.D., 1967. Trans. Sonics Ultrason. SU14, 123.

Mayer, W.G., 1964. J. Acoust. Soc. Am. 36, 779.

Imaging Experiments:

Goruk, W.S., Vella, P.J. and Stegeman, G.I.A., 1973. Phys. Lett. 45A, 357.

Loeber, A.D. and Hiedemann, E.A., 1955. J. Acoust. Soc. Am. 28, 27.

Ristic, W.M., Zuliani, M.J.J., Stegeman, G.I.A. and Vella, P.J., 1972. Appl. Phys. Lett. 21, 85.

Vella, P.J. and Stegeman, G.I.A., 1973. Appl. Phys. Lett. 23, 296.

Zuliani, M.J.J., Ristic, V.M., Vella, P.J. and Stegeman, G.I.A., 1973. J. Appl. Phys. 44, 2964.